

AN INVESTIGATION OF MICRODENSITOMETRY

by

Wendell Paul Goring

A Thesis Submitted to the Faculty of the
COMMITTEE ON OPTICAL SCIENCES (GRADUATE)
In Partial Fulfillment of the Requirements
For the Degree of
MASTER OF SCIENCE
In the Graduate Collège
THE UNIVERSITY OF ARIZONA

1 9 8 0

STATEMENT BY AUTHOR

This thesis has been submitted in partial fulfillment of requirements for an advanced degree at The University of Arizona and is deposited in the University Library to be made available to borrowers under rules of the Library.

Brief quotations from this thesis are allowable without special permission, provided that accurate acknowledgment of source is made. Requests for permission for extended quotation from or reproduction of this manuscript in whole or in part may be granted by the head of the major department or the Dean of the Graduate College when in his judgment the proposed use of the material is in the interests of scholarship. In all other instances, however, permission must be obtained from the author.

SIGNED: _____

William Paul Garrison

APPROVAL BY THESIS DIRECTOR

This thesis has been approved on the date shown below:

R. R. Shannon

R. R. SHANNON

Professor of Optical Sciences

18 April 60

Date

ACKNOWLEDGMENTS

An author may claim credit for his words and should accept responsibility for his mistakes, but credit for his thought process is not solely his. It belongs in part to his mentors and family.

While I cannot acknowledge them all on this page I would like at a minimum to mention two of my technical mentors. The first is my uncle, Albert Miller, who peaked the "scientific curiosity" of a four-year-old with a homemade telegraph key and wires, bulbs, batteries and a speaker. The most recent is Professor Robert Shannon, who with patience and well chosen questions helped to mature an inquisitive mind. For this I thank them both.

I thank my parents, Henry and Ann Goring, and my aunt and uncle, Gertrude and Earl Spann, for their continuous support and encouragement.

Finally, I thank Norma Emptage for her friendship and for typing and retyping much of this paper, and Martha Stockton for bringing English to what was said.

TABLE OF CONTENTS

	Page
LIST OF ILLUSTRATIONS	v
ABSTRACT	ix
1. INTRODUCTION	1
2. SYSTEM OVERVIEW.	3
Light Source Subsystem	6
Optical Subsystem.	7
Light Detecting, Digitizing and Recording Subsystem. . .	7
Scanning Stage and Stage Control Subsystem	8
3. OPTICAL SYSTEM	10
4. RESULTS.	26
5. CONCLUSIONS.	78
Experimental Overhead.	78
Hardware and Software Documentation.	79
Human Factors.	79
Legacy	80
APPENDIX A: MICRODENSITOMETER PHYSICAL CONSTRUCTION	82
APPENDIX B: SYSTEM CIRCUITRY.	88
APPENDIX C: ANALOG TO DIGITAL CONVERTER LINEARITY	99
REFERENCES	101

LIST OF ILLUSTRATIONS

Figure		Page
2.1.	System diagram of microdensitometer with automatic data collection.	5
3.1.	General microdensitometer optical system with associated nomenclature	10
3.2.	Mathematically idealized optical model of a microdensitometer, the "effective system"	12
4.1.	Microscope objective specifications	26
4.2.	Results of scanning a razor blade across the Gaussian spot produced by the 20X microscope objective.	28
4.3.	Results of scanning a razor blade across the Gaussian spot produced by the 10X microscope objective.	30
4.4.	Results of scanning a razor blade across the Gaussian spot produced by the 5X microscope objective	32
4.5.	Computer generated curve of the area under an ideal Gaussian surface versus razor blade position superimposed on Figure 4.2a	36
4.6.	Computer generated curve of the area under an ideal Gaussian surface versus razor blade position superimposed on Figure 4.3a	37
4.7.	Computer generated curve of the area under an ideal Gaussian surface versus razor blade position superimposed on Figure 4.4a.	
4.8.	Results of scanning a film edge across the Gaussian spot produced by the 20X microscope objective. Efflux objective is the 5X microscope objective	39
4.9.	Results of scanning a film edge across the Gaussian spot produced by the 20X microscope objective. Efflux objective is the 10X microscope objective.	40
4.10.	Results of an independent scan of the film edge under the same conditions as Figure 4.9.	41

LIST OF ILLUSTRATIONS--Continued

Figure		Page
4.11.	Results of scanning a Ronchi ruling containing 100 lines/inch across the Gaussian spot produced by the 20X microscope objective.	43
4.12.	Results of scanning a Ronchi ruling containing 300 lines/inch across the Gaussian spot produced by the 20X microscope objective.	45
4.13.	Power spectrum of the transmission data of the 100 line/inch Ronchi ruling shown in Figure 4.11.	48
4.14.	Power spectrum of the transmission data of the 300 line/inch Ronchi ruling shown in Figure 4.12.	50
4.15.	Rectangular scan pattern.	53
4.16.	Results of scanning a sample of Dupont Cronex x-ray film in the +x direction of the scan pattern shown in Figure 4.15	54
4.17.	Results of an independent scan of the same area on the Dupont Cronex sample in the +x direction as shown in Figure 4.15. No adjustment was made to the apparatus between the scans which acquired the data presented here and in Figure 4.16.	55
4.18.	Results of scanning a sample of Dupont Cronex x-ray film in the -x direction of the scan pattern shown in Figure 4.15. This data is from the same data set as that presented in Figure 4.16	56
4.19.	Results of an independent scan of the same area on the Dupont Cronex sample in the -x direction as shown in Figure 4.15. No adjustment was made to the apparatus between the scans which acquired the data presented here and in Figure 4.18	57
4.20.	Results of the first scan of a sample of Dupont Cronex film in the +x scan direction. The scan pattern consisted of 5 scans in the +x and -x directions each of 512 points with no scan motion in the y direction	59

LIST OF ILLUSTRATIONS--Continued

Figure	Page
4.21. Results of the second scan of the sample of Dupont Cronex film in the +x direction. This data is from an independent scan in the same data set as that plotted in Figure 4.20.	60
4.22. Results of averaging the 5 scans in the +x direction from the data set created by the scan pattern that consisted of 5 scans in the +x and -x directions each of 512 points with no scan motion in the y direction. . .	61
4.23. Results of averaging the 5 scans in the -x direction from the data set created by the scan pattern that consisted of 5 scans in the +x and -x directions each of 512 points with no scan motion in the y direction	63
4.24. Elevated cosine window applied to the data.	64
4.25. Wiener spectrum of the data shown in Figure 4.22.	65
4.26. Wiener spectrum of the data shown in Figure 4.23.	66
4.27. Wiener spectrum of data obtained from the same sample of x-ray film as those shown in Figure 4.22 and 4.23 but independent of those data	67
4.28. Wiener spectrum of another independent set of data obtained from the same sample of x-ray film as those shown in Figures 4.22 and 4.23.	68
4.29. Average of the Wiener spectra from six independent data sets all taken from the same sample of Dupont Cronex x-ray film.	70
4.30. Average of two of the six independent Wiener spectra that were averaged to give Figure 4.29.	71
4.31. Average of a different two of the six independent Wiener spectra that were averaged to give Figure 4.29. .	72
4.32. Physical setup used to make a film density wedge.	73
4.33. Results of scanning the film density wedge on Kodak 5063 film with the spot produced by the 10X microscope objective. The efflux objective was the 20X microscope objective	74

LIST OF ILLUSTRATIONS--Continued

Figure	Page
4.34. A plot of $D = -\ln(k\phi)$ versus position on the film for the data shown in Figure 4.33. The maximum transmission end of the data was scaled to give a $D_{\min} = 0.40$ in agreement with the value measured using the Macbeth densitometer. The remainder of the data was scaled by the same factor.	76

ABSTRACT

A microdensitometer with a He-Ne laser light source was constructed using commercially available optical components and scanning stage. Electronic control and data recording circuitry was custom made for this project. Scanning spots of 1.5 μm to 3.8 μm diameter were achieved. Several objects were scanned including a razor blade edge, an edge on Kodak 649F film, two Ronchi rulings and several samples of uniformly exposed x-ray film. The operation of the apparatus is described. A simplified theory is presented. Representative results of processing the collected data are shown.

CHAPTER 1

INTRODUCTION

The concept of a microdensitometer is not new. In fact, the first article to describe such a device appeared in 1912. In Annalen der Physik, P. P. Koch proposed "a recording microphotometer" for use in measuring spectrographic plates. Thus, even though the basic idea is more than half a century old, better understanding of the various aspects of microdensitometer operation is still unfolding. The initial understanding of the optical processes involved was based on paraxial (geometric) optics. This remains the logical point to begin an understanding, but we quickly find situations and cases where geometric approximations fail us or, worse yet, lead us astray. To improve our understanding we must add to geometrical optics the considerations of physical optics. Physical optics among other things allows us to set more meaningful limits on achievable sampling aperture sizes. Next, it is useful to bring the techniques of linear systems to bear on the problem. We get a feel for the overall system behavior by cascading an optical field through each optical element to the next from source to detector.

The comparatively recent understanding of partial coherence is also an applicable topic, from which we draw the quasi-monochromatic approximation for the case of a coherent light source as well as the

idea of effective incoherence for the noncoherent case. A related area in which there is clearly room for more understanding is in our attempt to characterize the sample mathematically. A typical mathematical model often postulated is a thin, nonscattering pure absorber. Actual photographic film has thickness, does scatter light and introduces phase changes. Treating any of these actual properties makes the problem very complicated analytically and leaves us with numerical solution as the only real option. The amount of calculation necessary for this option is very large and even then yields solutions only for the given case.

This investigation has confirmed some of the theoretically proposed properties of microdensitometers, verified some of the knowns and considered some of the as yet unknown properties.

CHAPTER 2

SYSTEM OVERVIEW

A microdensitometer extracts information important to the optician from transparent photographic layers. The first characteristic of the data so obtained is suggested by the name of the instrument; that is, density is measured over a very small sampling area. (The statement may seem inconsistent since density is defined as a macroscopic quantity.) The second characteristic of the microdensitometer data is that the location of each sampled area is precisely known with respect to the other sampled areas.

The data so obtained has been influenced by the optical properties of the microdensitometer used to make the measurement. To obtain the information that was actually contained in the photographic sample we must be able to remove from the measured result the bias and contributions introduced by the microdensitometer itself. This is possible only if the relationship between the actual sample and the measurement result is a linear one.

When constructing a microdensitometer from scratch, we are able to fix some of the optical properties of the system by selecting the optical components and by specifying the physical layout of the apparatus. The choices that we make are guided by the above desire for linearity, and by the physical limitations placed on us by the weight, size, shape, etc. of the actual components (see Appendix A).

Once the densitometer is constructed and aligned the data collection and analysis process has several basic steps common to most analyses:

1. The sample is suitably mounted.
2. The choices of sampling aperture, sample interval and number of sample points are made depending on the characteristics of the sample and the information desired as final result.
3. The apparatus is focused, the sample is scanned and the data is recorded.
4. The transmission distribution of the sample itself is obtained by deconvolving the apparatus characteristics from the measured data.
5. The transmission distribution of the sample is then processed further to obtain information about the optical system that produced the image recorded on film--or perhaps to obtain information about the photographic process itself, when characteristics of the original image-producing optical system are known.

The step from theory to practice requires that we construct a system that encompasses more than just the optical system. In Fig. 2.1 we show the actual automated system in its entirety.

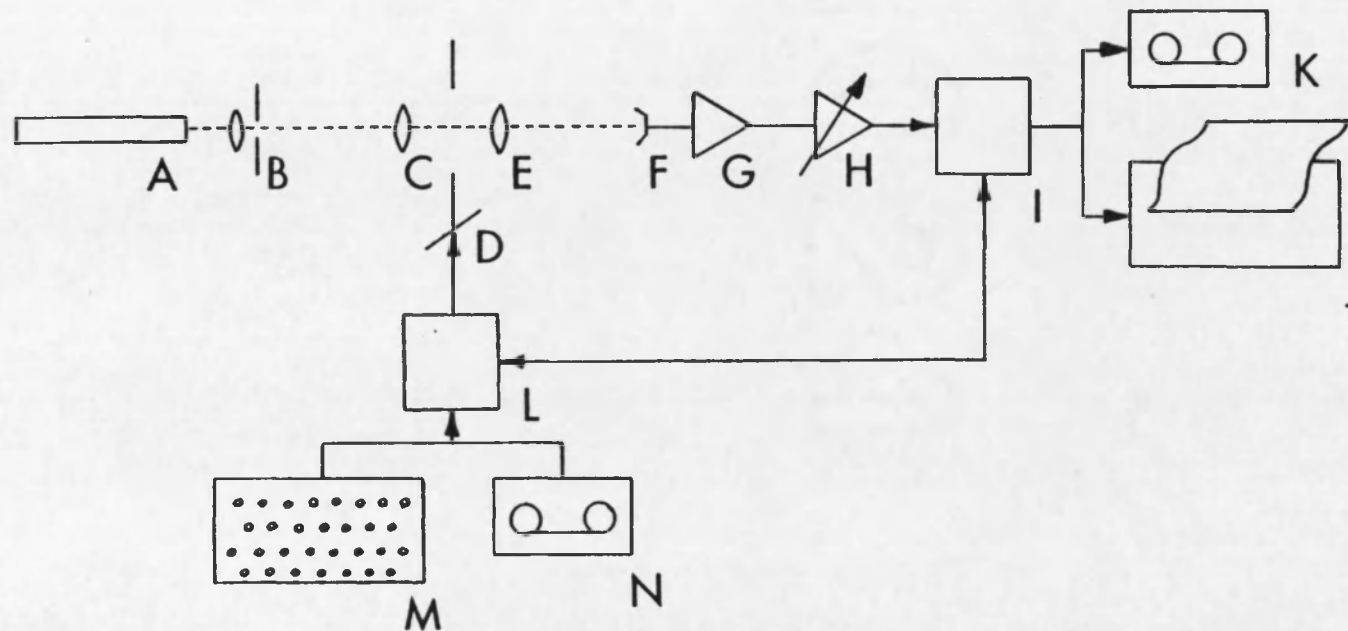


Figure 2.1. System diagram of microdensitometer with automatic data collection.

- | | | |
|--|---|--|
| A. Light source, He-Ne laser | F. Photodiode, SGD-100A | K. Digital tape recorder, TI-733, recorded data |
| B. Spatial filter | G. Amplifier, buffer | L. Scanning stage digital control circuitry |
| C. Influx objective | H. Amplifier, variable gain | M. Keyboard, TI-733, to input new scan control commands. |
| D. Scanning stage, Carl Zeiss, 0.5 $\mu\text{m}/\text{step}$ | I. Analog-to-digital converter and digital output circuitry | N. Digital tape playback, TI-733, new scan commands |
| E. Efflux objective | J. Printer, TI-733 | |

For purposes of description the system has four subsystems: the light source, the optical subsystem, the light detecting, digitizing and recording subsystem, and the scanning stage and stage control subsystem.

Light Source Subsystem

The light source is a Spectra Physics Model 236 He-Ne laser, which is filtered by a Gaertner spatial filter with a 10X objective and a 25- μ m pinhole. After 3 hours warmup, the laser's light power output was found to be sufficiently stable that no stabilizing apparatus needed to be added to the laser.

It was found that no compensating circuit was needed to sample the laser output power and correct the gathered data for changes in laser output. However, in the course of this study two such circuits were evaluated and discarded. Both circuits sampled the output power of the laser with an SGD-100A photodiode. The resulting analog signal suitably scaled was used as the reference for 100% transmission. The analog signal corresponding to the actual light passing through the system and sample was then compared to the reference signal. The first circuit used an analog subtraction of the logarithms of both reference and signal. The system required constant adjustment. The analog modules were made by Optical Electronics, Inc. The second circuit that was constructed used a Burr Brown Research analog divider module. The reference signal was fed to the denominator input while the signal input was fed to the numerator input. It was noted that very slight changes in the reference (denominator) caused misleadingly large changes in the final result. This characteristic behavior seems to commonly be

"hidden" in the specification of divider circuits. The thoroughly warmed up uncompensated laser produced a light source stable enough for this investigation. Other workers in the field (Hoeschen and Miranda, 1977) have reported similar findings.

Optical Subsystem

The optical system is discussed thoroughly in Chapter 3. As an overview, the influx portion of the optical system focuses the source illumination at a reduction on the sample being scanned. Some of the focused light is transmitted by the sample under investigation. The efflux portion of the optics images the irradiated portion of the sample on the detector or collects the transmitted light and sends it to the detector (nonimaging).

Light Detecting, Digitizing and Recording Subsystem

The light that has been transmitted is the sample radiance distribution. It is this quantity that we are interested in as a means of determining what the transmission of the sample was. The quantity we are able to detect is power incident on the SGD-100A photodiode. An analog current is generated when light falls on the diode. We buffer and scale the analog signal appropriately using an SSS-725C instrumentation amplifier and a 72741P operational amplifier. Though we could record the result in analog form, we are ultimately interested in processing the result digitally on an available computer. Therefore, we choose to digitize the analog signal at this point and record it in a

digital format, on one of the tape drives of the Texas Instrument TI-733 terminal. To process the data we later go on line to a digital computer and send the data to the computer in digital format, without the need for further signal processing.

Digital circuitry, built by the author, triggers the A/D conversion and gates the result out in serial digital format to printer and/or digital tape recorder on the TI-733. That circuitry is discussed in detail in Appendix B. In the course of constructing the electronics, the digitizing characteristics of the analog-to-digital (A/D) converter made by Varadyne Systems were investigated. The results of that investigation are discussed in Appendix C.

Scanning Stage and Stage Control Subsystem

The scanning stage is a Carl Zeiss Model 47 34 81 microscope scanning stage. It is capable of motion in both x and y directions with step size of 0.5 μm and maximum stepping rate of 200 steps/minute. The stage, servo motors and driver electronics are all supplied by Zeiss as a unit. The unit was delivered wired for 220 VAC. Changing power transformer jumpers allows the stage to be used with 120 VAC. The stage driver circuitry moves the stage one step in the +x, -x, +y or -y direction for every TTL-compatible square wave pulse applied to one of four separate digital inputs on the driver electronics chassis. The stage motion is open loop; that is, a pulse is applied to the appropriate input and the stage moves one step. There is no feedback mechanism (shaft encoders, etc.) other than watching gross stage movement to verify that the motion has occurred.

Digital circuitry built by the author pulses the scanning stage driver circuit, keeps track of the current position of the stage and accepts new inputs of direction, step size and current scan line limit from the TI-733 keyboard or prerecorded tape played on the TI-733 "play-back" cassette tape drive. The circuitry is discussed in Appendix B.

CHAPTER 3

OPTICAL SYSTEM

Microdensitometers exist in various configurations, sizes and shapes. Figure 3.1 shows the most general configuration and the associated nomenclature proposed to the ANSI Working Group on Microdensitometry by C. S. McCamy (1966).

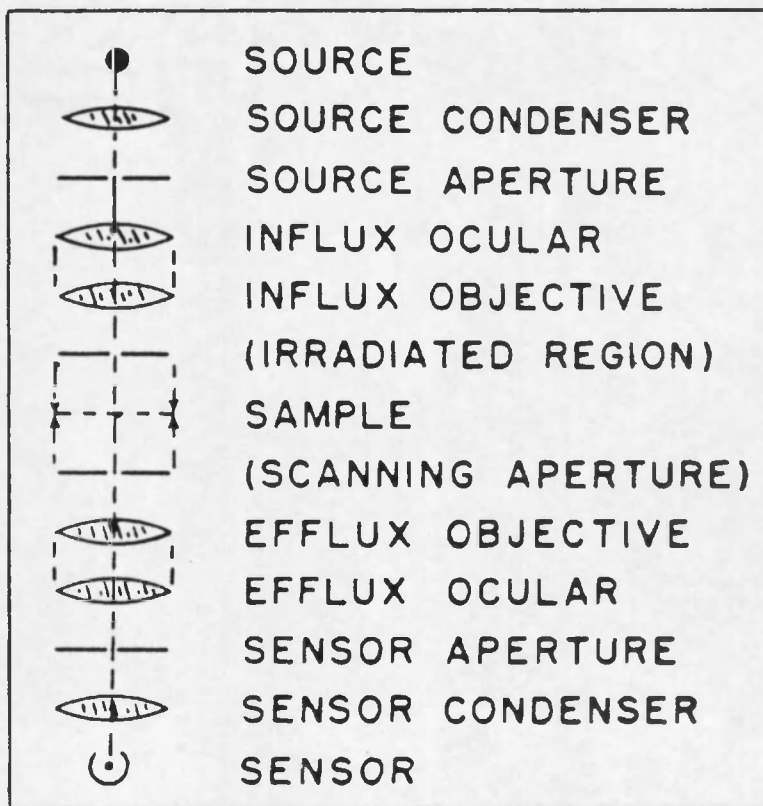


Figure 3.1. General microdensitometer optical system with associated nomenclature.

(Swing, 1973, Fig. 1, p. 187)

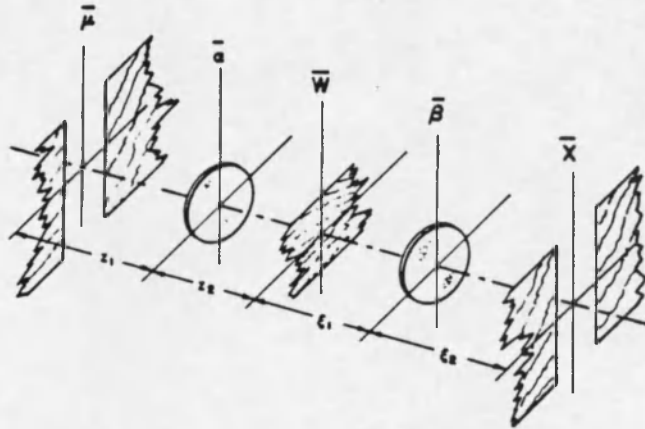
It is not necessary that each microdensitometer contain all of these components. However, in comparing one device to another it is convenient to use the standardized name in referring to the components that are contained.

The microdensitometer that we will analyze using the above framework has as its light source a Spectra Physics Model 236 He-Ne laser. Weingärtner (1971), in an article in Optik, suggests the laser as a microdensitometer light source. A major advantage that he points out explicitly is that a high flux density is available in the light probe when a laser source is used. Another advantage of a laser source is that the beam's radiance profile is Gaussian. Citing Kogelnik and Li (1966), Hoeschen and Mirandé (1977, p. 460) stressed that "even with defocusing, the radiance distribution retains its Gaussian profile." As we will also see in the following analysis, the rotationally symmetric character of the Gauss function allows us to separate some integrals that would otherwise be particularly difficult to handle.

The approach and notation for the following mathematical discussion derives from Swing's definitive paper "Microdensitometer Optical Performance: Scalar Theory and Experiment" (1976a), as well as an unpublished supplement to this paper (Swing, 1976b); Berán and Parrent's book Theory of Partial Coherence (1964); and Parrent and Thompson's book Physical Optics Notebook (1969).

It is common practice when analyzing the system to replace the schematic of actual optical components, Fig. 3.1, with a mathematically

idealized optical model, shown in Fig. 3.2. Swing (1976a) has dubbed this model the "effective system."



$\bar{\mu}$ - source aperture; $\bar{\alpha}$ - influx optics; \bar{w} - sample plane;
 $\bar{\beta}$ - efflux optics; $\bar{\xi}$ - image plane and sensor aperture.

Figure 3.2. Mathematically idealized optical model of a microdensitometer, the "effective system".

(Swing, 1976a, Fig. 1, p. 560)

The microdensitometer described in this chapter uses standard microscope objectives available from Rolyn Optics Company in Arcadia, California. The objectives are used on axis with the aperture centered about a line that is normal to the Zeiss scanning stage (see Figure A.1, p. 83).

In this configuration it is reasonable to make the following assumptions:

1. The optical system is stationary.
2. Gaussian (paraxial) approximations are adequate.
3. The thin lens equations can be used:

$$\frac{1}{z_1} + \frac{1}{z_2} = \frac{1}{f_1}$$

(1)

$$\frac{1}{\xi_2} + \frac{1}{\xi_2} = \frac{1}{f_2}$$

4. The objectives are essentially diffraction-limited with circular pupils.
5. The sagittal approximation (which follows from the paraxial approximation) applies.

The light source is an He-Ne laser, so it is reasonable in our use of the theory of partial coherence to use the quasi-monochromatic approximation.

An additional approximation must be made to make the mathematical model tractable in closed form. That approximation considers the photographic material to be a grain-free, nonscattering, thin, continuous distribution of transmittance. With this approximation we have departed from what we know to be the physical case. However, this is the most reasonable approach since it allows a mathematical solution, the results of which can be qualified later to include the effects of the grain and other actual characteristics of the photographic material.

The fundamental basis for what follows is ultimately the Fresnel-Kirchoff diffraction theory developed as it applied to partially coherent propagation in Theory of Partial Coherence (Beran and Parrent, 1964) and Optical Sciences courses 206 and 322. The notation followed here is Swing's (1976a,b).

Having accepted the paraxial and sagittal approximations, we can propagate the mutual coherence in our effective system from one plane to another by multiplying by the complex exponentials:

$$\exp\{ik(p_1 - q_1)^2/2d\} \exp\{-ik(p_2 - q_2)^2/2d\} \quad (2)$$

where p is an image point, q a source point, and d the distance between source and image planes. We then propagate the mutual coherence through a lens by multiplying by the pupil function of the lens and by phase factors that account for the converging effect of the lens on the incident wavefront:

$$F(p_1)F^*(p_2) \exp(-ikp_1^2/2f) \exp(ikp_2^2/2f) \quad (3)$$

The propagation of the mutual coherence from the source (where it is denoted by $\Gamma_o(\mu_1, \mu_2)$) to the sensor (where it is denoted by $\Gamma(x_1, x_2, \theta)$) is described by the following integrals:

$$\Gamma(x_1, x_2, \theta) = \int \Gamma_o(\mu_1, \mu_2) \cdot t(\mu_1) \cdot t^*(\mu_2)$$

Mutual coherence function Γ incident on the source aperture t in the μ plane.

$$\cdot \exp\{ik(\alpha_1 - \mu_1)^2/2z_1\} \exp\{-ik(\alpha_2 - \mu_2)^2/2z_1\}$$

Propagating the mutual coherence from the source plane μ to the first lens in the α plane.

$$\cdot F_1(\alpha_1) F_1^*(\alpha_2) \exp(-ik\alpha_1^2/2f_1) \exp(ik\alpha_2^2/2f_1)$$

Pupil function of the lens F and phase factors to account for the converging wavefront due to the lens in the α plane.

$$\cdot \exp\{ik(w_1 - \alpha_1)^2/2z_2\} \exp\{-ik(w_2 - \alpha_2)^2/2z_2\}$$

Propagating mutual coherence from the lens in the α plane to the sample in the w plane.

$$\cdot \phi(w_1 - \theta) \phi^*(w_2 - \theta)$$

Radiance characteristic $\phi\phi^*$ of the sample being examined where θ is the distance that the sample has been shifted from a chosen origin to account for the scanning motion of the microdensitometer.

$$\cdot \exp\{ik(\beta_1 - w_1)^2/2\xi_1\} \exp\{-ik(\beta_2 - w_2)^2/2\xi_1\}$$

Propagating the mutual coherence from the sample plane w to the lens in the β plane.

$$\cdot F_2(\beta_1) F_2^*(\beta_2) \exp(-ik\beta_1^2/2f_2) \exp(ik\beta_2^2/2f_2)$$

Pupil function F of the second lens and phase factors to account for the converging wavefront due to the lens in the β plane.

$$\cdot \exp\{ik(x_1 - \beta_1)^2/2\xi_2\} \exp\{-ik(x_2 - \beta_2)^2/2\xi_2\}$$

Propagating the mutual coherence from the lens in the β plane to the sensor in the x plane.

$$\cdot m(x_1) m^*(x_2) d\mu_1 d\mu_2 d\alpha_1 d\alpha_2 dw_1 dw_2 d\beta_1 d\beta_2 \quad (4)$$

Irradiance characteristic mm^* of the sensor aperture in the x plane.

The detector, an SGD-100A photodiode, is sensitive to irradiance rather than amplitude, so we form the limit

$\Gamma(x, x, \theta) = I(x, \theta)$ and integrate over the area of the detector:

$$I(\theta) = \int I(x, \theta) dx \quad (5)$$

When using the expression in equation (4) for $\Gamma(x, x, \theta)$ we obtain:

$$\begin{aligned} I(\theta) = & \int \Gamma_0(\mu_1, \mu_2) t(\mu_1) t^*(\mu_2) \exp(ik\mu_1^2/2z_1) \exp(-ik\mu_2^2/2z_1) \\ & \cdot \int F_1(\alpha_1) \exp\{ik\alpha_1^2(1/2z_1 - 1/2f_1 + 1/2z_2)\} \exp\{-ik\alpha_1(\mu_1/z_1 + w_1/z_2)\} d\alpha_1 \\ & \cdot \int F_1^*(\alpha_2) \exp\{-ik\alpha_2^2(1/2z_1 + 1/2z_2 - 1/2f_1)\} \exp\{ik\alpha_2(w_2/z_2 + \mu_2/z_1)\} d\alpha_2 \\ & \cdot \phi(w_1 - \theta) \cdot \phi^*(w_2 - \theta) \exp\{ikw_1^2(1/2z_2 + 1/2\xi_1)\} \exp\{-ikw_2^2(1/2z_2 + 1/2\xi_1)\} \\ & \cdot \int F_2(\beta_1) \exp\{ik\beta_1^2(1/2\xi_1 - 1/2f_2 + 1/2\xi_2)\} \exp\{-ik\beta_1(w_1/\xi_1 + x/\xi_2)\} d\beta_1 \\ & \cdot \int F_2^*(\beta_2) \exp\{-ik\beta_2^2(1/2\xi_1 - 1/2f_2 + 1/2\xi_2)\} \exp\{ik\beta_2(w_2/\xi_1 + x/\xi_2)\} d\beta_2 \\ & \cdot m(x) m^*(x) d\mu_1 d\mu_2 dw_1 dw_2 dx \end{aligned} \quad (6)$$

When the lenses are in focus, the equations

$$\frac{1}{z_1} + \frac{1}{z_2} = \frac{1}{f_1} \quad \text{and} \quad \frac{1}{\xi_1} + \frac{1}{\xi_2} = \frac{1}{f_2} \quad (1)$$

simplify the integrals over α_1 , α_2 , β_1 and β_2 to

$$\begin{aligned}
I(\theta) = & \int \Gamma_0(\mu_1, \mu_2) t(\mu_1) t^*(\mu_2) \exp\{ik(\mu_1^2 - \mu_2^2)/2z_1\} \\
& \cdot \int F_1(\alpha_1) \exp\{-ik\alpha_1(\mu_1/z_1 + w_1/z_2)\} d\alpha_1 \\
& \cdot \int F_1^*(\alpha_2) \exp\{ik\alpha_2(\mu_2/z_1 + w_2/z_2)\} d\alpha_2 \\
& \cdot \phi(w_1 - \theta) \phi^*(w_2 - \theta) \exp\{-ik/2 [(w_1^2 - w_2^2)/z_2 + (w_1^2 - w_2^2)/\xi_1]\} \\
& \cdot \int F_2(\beta_1) \exp\{-ik\beta_1(w_1/\xi_1 + x/\xi_2)\} d\beta_1 \\
& \cdot \int F_2^*(\beta_2) \exp\{ik\beta_2(w_2/\xi_1 + x/\xi_1)\} d\beta_2 \\
& \cdot M(x) d\mu_1 d\mu_2 dw_1 dw_2 dx
\end{aligned} \tag{7}$$

We can simplify this equation further by the following arguments of scale. The approximation

$$\exp\{ik(\mu_1^2 - \mu_2^2)/2z_1\} \approx 1 \tag{8}$$

is reasonable since the source aperture size is on the order of ten micrometers (a spatial filter pinhole) while the distance z_1 is on the order of 100 millimeters (microscope standard conjugates).

Similarly, the approximation for the quadratic

$$\exp\{ik/2 [(w_1^2 - w_2^2)/z_2 + (w_1^2 - w_2^2)/\xi_1]\} \approx 1 \tag{9}$$

is reasonable since the portion of the sample being measured is on the order of micrometers while the distances z_2 and ξ_1 are on the order of millimeters.

Thus, the irradiance in the sensor plane is

$$\begin{aligned}
 I(\theta) = & \int \Gamma_0(\mu_1, \mu_2) t(\mu_1) t^*(\mu_2) \phi(w_1 - \theta) \phi^*(w_2 - \theta) \\
 & \cdot M(x) \tilde{F}_1(w_1/\lambda z_2 + \mu_1/\lambda z_1) \tilde{F}_1^*(w_2/\lambda z_2 + \mu_2/\lambda z_1) \\
 & \cdot \tilde{F}_2(x/\lambda \xi_2 + w_1/\lambda \xi_1) \tilde{F}_2^*(x/\lambda \xi_2 + w_2/\lambda \xi_1) \\
 & \cdot d\mu_1 d\mu_2 dw_1 dw_2 dx
 \end{aligned} \tag{10}$$

as is shown by Swing (1976a).

We are interested in this quantity for those measurements where our primary concern is with resolution, as when measuring edges or periodic structures, such as Ronchi rulings.

We are also interested in the spectrum of the image that is given by the Fourier transform of $I(\theta)$:

$$\tilde{Y}(\sigma) = \int I(\theta) \exp(-2\pi i \sigma \theta) d\theta \tag{11}$$

In equation (10) the only terms containing θ , the distance that the sample has been shifted, are the two ϕ terms representing the sample radiance distribution. We group the θ terms after substituting equation (10) into equation (11) to obtain:

$$\begin{aligned}
\tilde{Y}(\sigma) = & \int \Gamma_0(\mu_1, \mu_2) t(\mu_1) t^*(\mu_2) M(x) \\
& \cdot \tilde{F}_1(w_1/\lambda z_2 + \mu_1/\lambda z_1) \tilde{F}_1^*(w_2/\lambda z_2 + \mu_2/\lambda z_1) \\
& \cdot \tilde{F}_2(x/\lambda \xi_2 + w_1/\lambda \xi_1) \tilde{F}_2^*(x/\lambda \xi_2 + w_2/\lambda \xi_1) \\
& \cdot \int \phi(w_1 - \theta) \phi^*(w_2 - \theta) \exp(-2\pi i \sigma \theta) d\theta \\
& \cdot d\mu_1 d\mu_2 dw_1 dw_2 dx
\end{aligned} \tag{12}$$

For the moment we will consider only the θ integral and refer to it as Integral 1. If we replace the two θ terms representing the sample's radiance characteristic by their Fourier transforms,

$$\begin{aligned}
\phi(w_1 - \theta) &= \int \tilde{\phi}(n') \exp\{+2\pi i (w_1 - \theta)n'\} dn' \\
\phi^*(w_2 - \theta) &= \int \tilde{\phi}^*(n) \exp\{-2\pi i (w_2 - \theta)n\} dn
\end{aligned} \tag{13}$$

the θ integral then becomes:

$$\begin{aligned}
\text{Integral 1} &= \int \int \tilde{\phi}(n') \exp\{2\pi i (w_1 - \theta)n'\} dn' \\
&\cdot \int \tilde{\phi}^*(n) \exp\{-2\pi i (w_2 - \theta)n\} dn \\
&\cdot \exp\{-2\pi i \sigma \theta\} d\theta
\end{aligned} \tag{14}$$

When we collect terms in θ we have:

$$\begin{aligned}
\text{Integral 1} &= \int \tilde{\phi}(n') \exp\{2\pi i w_1 n'\} \int \tilde{\phi}^*(n) \exp\{-2\pi i w_2 n\} \\
&\cdot \int \exp\{-2\pi i \theta (n' - n + \sigma)\} d\theta dn dn'
\end{aligned} \tag{15}$$

We recognize the integral over θ as an integral representation of a delta function of the form:

$$\delta(x-x') = \int \exp\{-2\pi i \mu(x-x')\} d\mu \quad (16)$$

(Lighthill, 1959).

The sifting property of the delta function allows us to do the integral over η' , yielding:

$$\begin{aligned} \text{Integral 1} = \int \tilde{\phi}(\eta-\sigma) \exp\{2\pi i w_1(\eta-\sigma)\} \\ \cdot \tilde{\phi}^*(\eta) \exp\{-2\pi i w_2 \eta\} d\eta \end{aligned} \quad (17)$$

Using this result for the θ integral in equation (12) gives:

$$\begin{aligned} \tilde{Y}(\sigma) = \int \Gamma_0(\mu_1, \mu_2) t(\mu_1) t^*(\mu_2) M(x) \tilde{F}_1(w_1/\lambda z_2 + \mu_1/\lambda z_1) \\ \cdot \tilde{F}_1^*(w_2/\lambda z_2 + \mu_2/\lambda z_1) \tilde{F}_2(x/\lambda \xi_2 + w_1/\lambda \xi_1) \tilde{F}_2^*(x/\lambda \xi_2 + w_2/\lambda \xi_1) \\ \cdot \int \tilde{\phi}(\eta-\sigma) \exp\{2\pi i w_1(\eta-\sigma)\} \tilde{\phi}^*(\eta) \exp\{-2\pi i w_2 \eta\} d\eta d\mu_1 d\mu_2 dw_1 dw_2 dx \end{aligned} \quad (18)$$

Grouping terms in w_1 and in w_2 yields:

$$\begin{aligned} \tilde{Y}(\sigma) = \int \Gamma_0(\mu_1, \mu_2) t(\mu_1) t^*(\mu_2) M(x) \tilde{\phi}(\eta-\sigma) \tilde{\phi}^*(\eta) \\ \cdot \int \tilde{F}_1(w_1/\lambda z_2 + \mu_1/\lambda z_1) \tilde{F}_2(x/\lambda \xi_2 + w_1/\lambda \xi_1) \exp\{2\pi i w_1(\eta-\sigma)\} dw_1 \\ \cdot \int \tilde{F}_1^*(w_2/\lambda z_2 + \mu_2/\lambda z_1) \tilde{F}_2^*(x/\lambda \xi_2 + w_2/\lambda \xi_1) \exp\{-2\pi i w_2 \eta\} dw_2 d\mu_1 d\mu_2 d\eta dx \end{aligned} \quad (19)$$

Using the same procedure as before, we consider the integral over w_1 , replace the \tilde{F}_1 and \tilde{F}_2 terms with their Fourier transforms and regroup terms in w_1 in hopes of finding a delta function camouflaged in the equation. Thus,

$$\begin{aligned}
\text{Integral 2} &= \int \int F_1(\zeta') \exp\{2\pi i(w_1/\lambda z_2 + \mu_1/\lambda z_1)\zeta'\} d\zeta' \\
&\quad \cdot \int F_2(\zeta) \exp\{2\pi i(x/\lambda \xi_2 + w_1/\lambda \xi_1)\zeta\} d\zeta \\
&\quad \cdot \exp\{2\pi i(\eta - \sigma)w_1\} dw_1 \\
&= \int F_1(\zeta') \exp\{2\pi i\mu_1\zeta'/\lambda z_1\} \\
&\quad \cdot \int F_2(\zeta) \exp\{2\pi i x \zeta/\lambda \xi_2\} \\
&\quad \cdot \int \exp\{2\pi i(\zeta'/\lambda z_2 + \zeta/\lambda \xi_1 + \eta - \sigma)w_1\} dw_1 d\zeta d\zeta' \quad (20)
\end{aligned}$$

The sifting property of the delta function again allows the evaluation of one integral, in this case the integral over ζ' :

$$\begin{aligned}
\text{Integral 2} &= \int F_1[-\zeta z_2/\xi_1 - \lambda z_2(\eta - \sigma)] F_2(\zeta) \\
&\quad \cdot \exp\{(2\pi i\mu_1/\lambda z_1)[- \zeta z_2/\xi_1 - \zeta z_2(\eta - \sigma)]\} \exp\{2\pi i x \zeta/\lambda \xi_2\} d\zeta \quad (21)
\end{aligned}$$

Similarly, for the integral over w_2 in equation (19),

$$\begin{aligned}
\text{Integral 3} &= \int \int F_1^*(\zeta') \exp\{-2\pi i(w_2/\lambda z_2 + \mu_2/\lambda z_1)\zeta'\} d\zeta' \\
&\quad \cdot \int F_2^*(\zeta) \exp\{-2\pi i(x/\lambda \xi_2 + w_2/\lambda \xi_1)\zeta\} d\zeta \\
&\quad \cdot \exp\{-2\pi i w_2 \eta\} dw_2 \\
&= \int F_1^*(\zeta') \exp\{-2\pi i\mu_2\zeta'/\lambda z_1\} \\
&\quad \cdot \int F_2^*(\zeta) \exp\{-2\pi i x \zeta/\lambda \xi_2\} \\
&\quad \cdot \int \exp\{-2\pi i(\zeta'/\lambda z_2 + \zeta/\lambda \xi_1 + \eta)w_2\} dw_2 d\zeta d\zeta' \quad (22)
\end{aligned}$$

Again, the sifting property of the delta function yields:

$$\begin{aligned} \text{Integral 3} &= \int F_1^*[-\zeta z_2/\xi_1 - \eta \lambda z_2] F_2^*(\zeta) \\ &\cdot \exp\{(-2\pi i \mu_2/\lambda z_1)(-\zeta z_2/\xi_1 - \eta \lambda z_2)\} \exp\{-2\pi i x \zeta/\lambda \xi_2\} d\zeta \end{aligned} \quad (23)$$

So as not to confuse the variable of integration in Integral 2 with that of Integral 3, let $\zeta = \zeta'$:

$$\begin{aligned} \text{Integral 3} &= \int F_1^*(-\zeta' z_2/\xi_1 - \eta \lambda z_2) F_2^*(\zeta') \\ &\cdot \exp\{(-2\pi i \mu_2/\lambda z_1)(-\zeta' z_2/\xi_1 - \eta \lambda z_2)\} \exp\{-2\pi i x \zeta'/\lambda \xi_2\} d\zeta' \end{aligned} \quad (24)$$

Substituting Integral 2 and Integral 3 into equation (19) yields

$$\begin{aligned} \Upsilon(\sigma) &= \int \Gamma_0(\mu_1, \mu_2) t(\mu_1) t^*(\mu_2) M(x) \tilde{\phi}(\eta - \sigma) \tilde{\phi}^*(\eta) \\ &\cdot \int F_1\{-\zeta z_2/\xi_1 - \lambda z_2(\eta - \sigma)\} F_2\{\zeta\} \\ &\cdot \exp\{(2\pi i \mu_1/\lambda z_1)[-\zeta z_2/\xi_1 - \lambda z_2(\eta - \sigma)]\} \\ &\cdot \exp\{2\pi i \zeta x/\lambda \xi_2\} d\zeta \\ &\cdot \int F_1^*(-\zeta' z_2/\xi_1 - \eta \lambda z_2) F_2^*(\zeta') \\ &\cdot \exp\{(-2\pi i \mu_2/\lambda z_1)(-\zeta' z_2/\xi_1 - \eta \lambda z_2)\} \\ &\cdot \exp\{-2\pi i x \zeta'/\lambda \xi_2\} d\zeta' d\mu_1 d\mu_2 d\eta dx \end{aligned} \quad (25)$$

Now grouping terms in x , μ_1 and μ_2 , we have,

$$\begin{aligned}
\Upsilon(\sigma) = & \int F_1[-\zeta z_2/\xi_1 - \lambda z_2(\eta - \sigma)] F_1^*[\zeta' z_2/\xi_1 - \eta \lambda z_2] \\
& \cdot F_2[\zeta] F_2^*[\zeta'] \tilde{\phi}(\eta - \sigma) \tilde{\phi}^*(\eta) \\
& \cdot \int M(x) \exp\{2\pi i x/\lambda \xi_2(\zeta - \zeta')\} dx \\
& \cdot \int \Gamma_0(\mu_1, \mu_2) t(\mu_1) t^*(\mu_2) \\
& \cdot \exp\{(2\pi i \mu_1/\lambda z_1)[-\zeta z_2/\xi_1 - \lambda z_2(\eta - \sigma)]\} \\
& \cdot \exp\{(-2\pi i \mu_2/\lambda z_1)(-\zeta' z_2/\xi_1 - \eta \lambda z_2)\} d\mu_1 d\mu_2 d\eta d\zeta d\zeta' \quad (26)
\end{aligned}$$

The sampling aperture is created in one of two ways. The most common technique, called "image scanning" considers the sampling aperture to be the reduced image of the sensor aperture in the sample plane. In this case the sample is illuminated by the influx optics over an area larger than the sampling aperture.

When we "sample scan" we create the sampling aperture by projecting the source aperture onto the sample itself. This is the method used in this project. Swing (1976a, p.562) notes that "very few microdensitometers employ this mode of operation." The lower limit to the size of the sampling aperture is the impulse response of the influx optics since the effective aperture is the sampling aperture itself: that is, the actual reduced spot in the image plane of the influx objective. The detail on the sample (usually the photographic image on the negative) is convolved with the sampling aperture directly. The efflux optics collects the flux passing through the sample being scanned and relays that flux to the sensor.

In this case we can make a simplification if we assume that the sensor aperture is wide enough to collect all the flux of interest. It then contributes a constant attenuation to the flux,

$$M(x) = \text{constant}$$

and its spectrum is a delta function,

$$\tilde{M}[(\zeta' - \zeta)/\lambda\xi_2] = \delta(\zeta' - \zeta)$$

Thus the term in equation (26) becomes

$$\int M(x) \exp\{-2\pi i x / \lambda\xi_2 (\zeta' - \zeta)\} dx = \tilde{M}[(\zeta' - \zeta)/\lambda\xi_2] = \delta(\zeta' - \zeta) \quad (27)$$

while equation (26) itself becomes

$$\begin{aligned} \tilde{Y}(\sigma) = & \int F_1[-\zeta z_2 / \xi_1 - \lambda z_2 (\eta - \sigma)] F_1^*[\zeta z_2 / \xi_1 - \eta \lambda z_2] \\ & \cdot F_2[\zeta] F_2^*[\zeta] \tilde{\phi}(\eta - \sigma) \tilde{\phi}^*(\eta) \\ & \cdot \int \Gamma_0(\mu_1, \mu_2) t(\mu_1) t^*(\mu_2) \\ & \cdot \exp\{(2\pi i \mu_1 / \lambda z_1) [-\zeta z_2 / \xi_1 - \lambda z_2 (\eta - \sigma)]\} \\ & \cdot \exp\{(-2\pi i \mu_1 / \lambda z_1) (-\zeta z_2 / \xi_1 - \eta \lambda z_2)\} d\mu_1 d\mu_2 d\eta d\zeta \quad (28) \end{aligned}$$

In the case of the spatially filtered laser source used in this project we can argue that the Gaussian profile of the laser beam has an amplitude so close to zero before the source aperture is reached that the term representing the source aperture radiance distribution can be taken to be 1 for all points of interest. The size of the source is then contained in the Γ term of the equation

$$\Gamma_0(\mu_1, \mu_2) = A_z^{\frac{1}{2}} \exp(-\mu_1^2/\omega_z^2) A_z^{\frac{1}{2}} \exp(-\mu_2^2/\omega_z^2) \quad (29)$$

When this term is substituted for Γ in equation (28) the integrals over μ_1 and μ_2 separate, yielding

$$\begin{aligned} \text{Integral 4} = & \int A_z^{\frac{1}{2}} \exp(-\mu_1^2/\omega_z^2) \\ & \cdot \exp\{(2\pi i \mu_1/\lambda z_1) [-\zeta z_2/\xi_1 - \lambda z_2(\eta - \sigma)]\} d\mu_1 \\ & \cdot \int A_z^{\frac{1}{2}} \exp(-\mu_2^2/\omega_z^2) \\ & \cdot \exp\{(-2\pi i \mu_2/\lambda z_1) (-\zeta z_2/\xi_1 - \eta \lambda z_2)\} d\mu_2 \quad (30) \end{aligned}$$

We recognize these integrals as the Fourier transforms of a Gaussian and its complex conjugate. Thus, equation (28) becomes

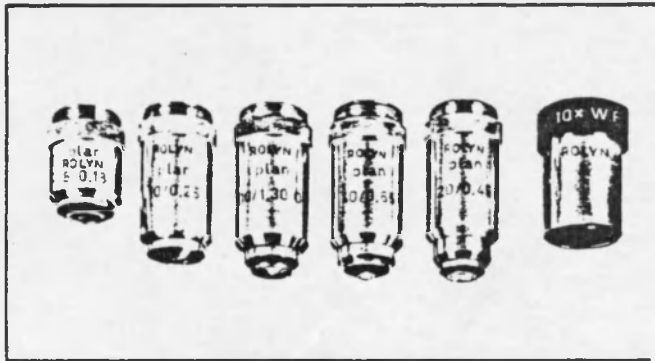
$$\begin{aligned} \tilde{Y}(\sigma) = & \int F_1[-\zeta z_2/\xi_1 - \lambda z_2(\eta - \sigma)] F_1^*[\zeta z_2/\xi_1 - \eta \lambda z_2] \\ & \cdot F_2[\zeta] F_2^*[\zeta] \tilde{\phi}(\eta - \sigma) \tilde{\phi}^*(\eta) A_z \\ & \cdot \exp\{-[-\zeta z_2/\lambda z_1 \xi_1 - z_2(\eta - \sigma)/z_1]^2/\omega_z^2\} \\ & \cdot \exp\{-[-\zeta z_2/\lambda z_1 \xi_1 - \eta z_2/z_1]^2/\omega_z^2\} d\eta d\zeta \quad (31) \end{aligned}$$

Equation (31) relates the spatial frequency spectrum at the sensor to the spatial frequency spectrum of the sample. Application of this equation to specific cases is done using numerical integration.

CHAPTER 4

RESULTS

Four microscope objectives of better than average quality were used in this investigation. They were: one 20X objective (NA 0.45), two 10X objectives (NA 0.25), and one 5X objective (NA 0.18). They are all specified as "plan" or flat field. They were obtained from Rolyon Optics Co., Arcadia, California 91006. Figure 4.1 reproduces the objectives' specifications from the Rolyon catalog.



STOCK #	X	E.F.L.	W.D.	N.A.
80.3515	5:1	32.0	19.0	0.18
80.3520	10:1	16.0	4.6	0.25
80.3525	20:1	9.0	0.7	—
80.3550	40:1	—	0.3	—

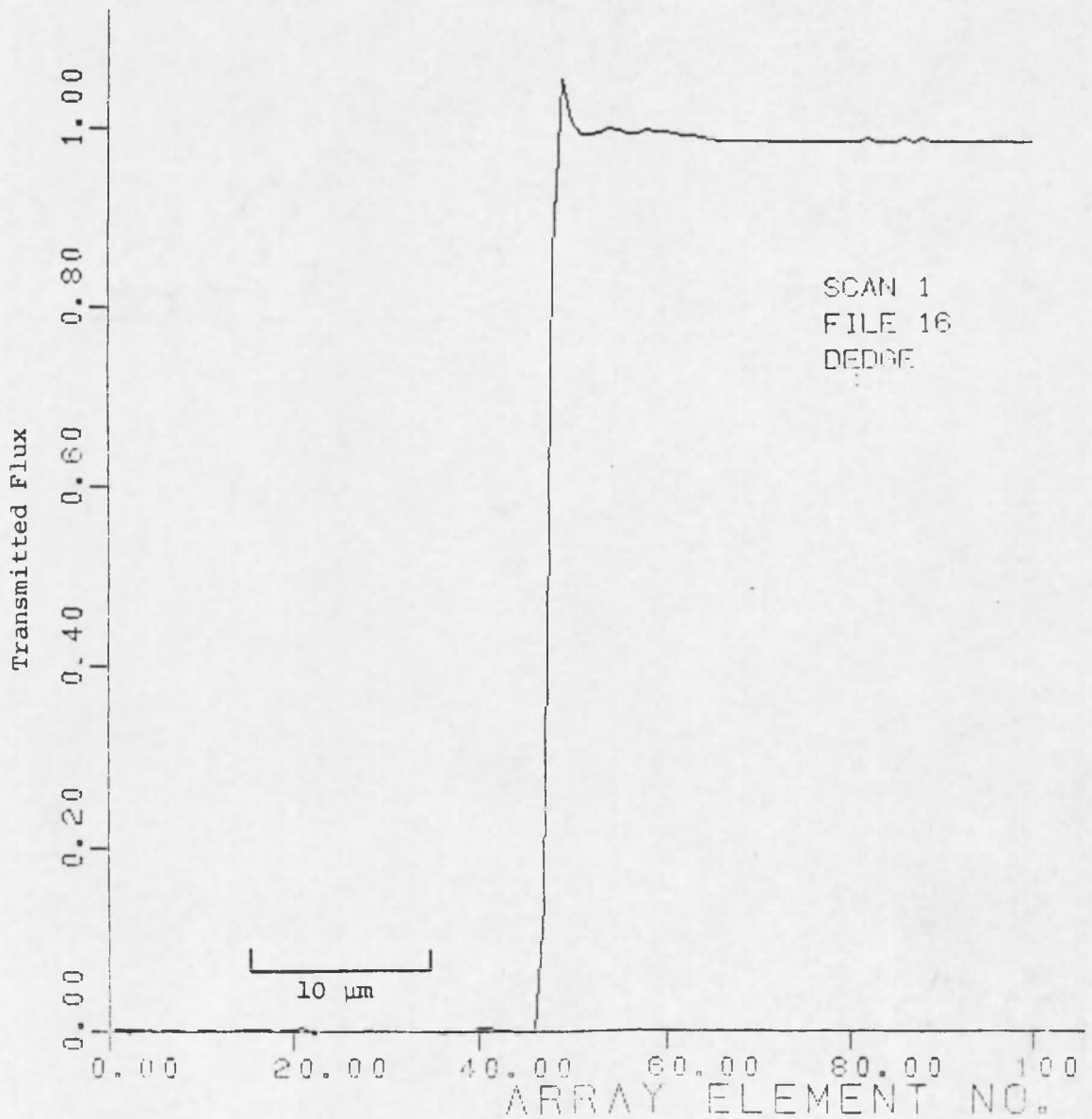
Figure 4.1. Microscope objective specifications.

(Optics for Industry, Catalog 77,
1977, p. 56)

The smallest obtainable Gaussian light probe produced by each of the objectives was investigated as follows. One of the 10X objectives was chosen as the collecting optic and mounted in the upper microscope carrier. A Gillette "super stainless" razor blade was mounted on the Zeiss scanning stage in the location normally occupied by the photographic negative or slide. The razor blade was scanned across the focused spot produced when each of the remaining objectives was mounted in the lower microscope carrier as the influx optics. The razor blade was moved in 0.5 μm steps.

Figure 4.2 shows the measured results as the razor blade was scanned in 0.5 μm increments toward and away from the focused spot produced by the 20X objective. Figures 4.3 and 4.4 show the measured results for the 10X and 5X objectives respectively. The plots have been normalized to a value of 1.0 for an unobstructed light path. The spot widths which can be estimated from the plotted values justify the assumption that the optics are diffraction limited. Table 4.1 compares the measured spot sizes to the theoretically expected values.

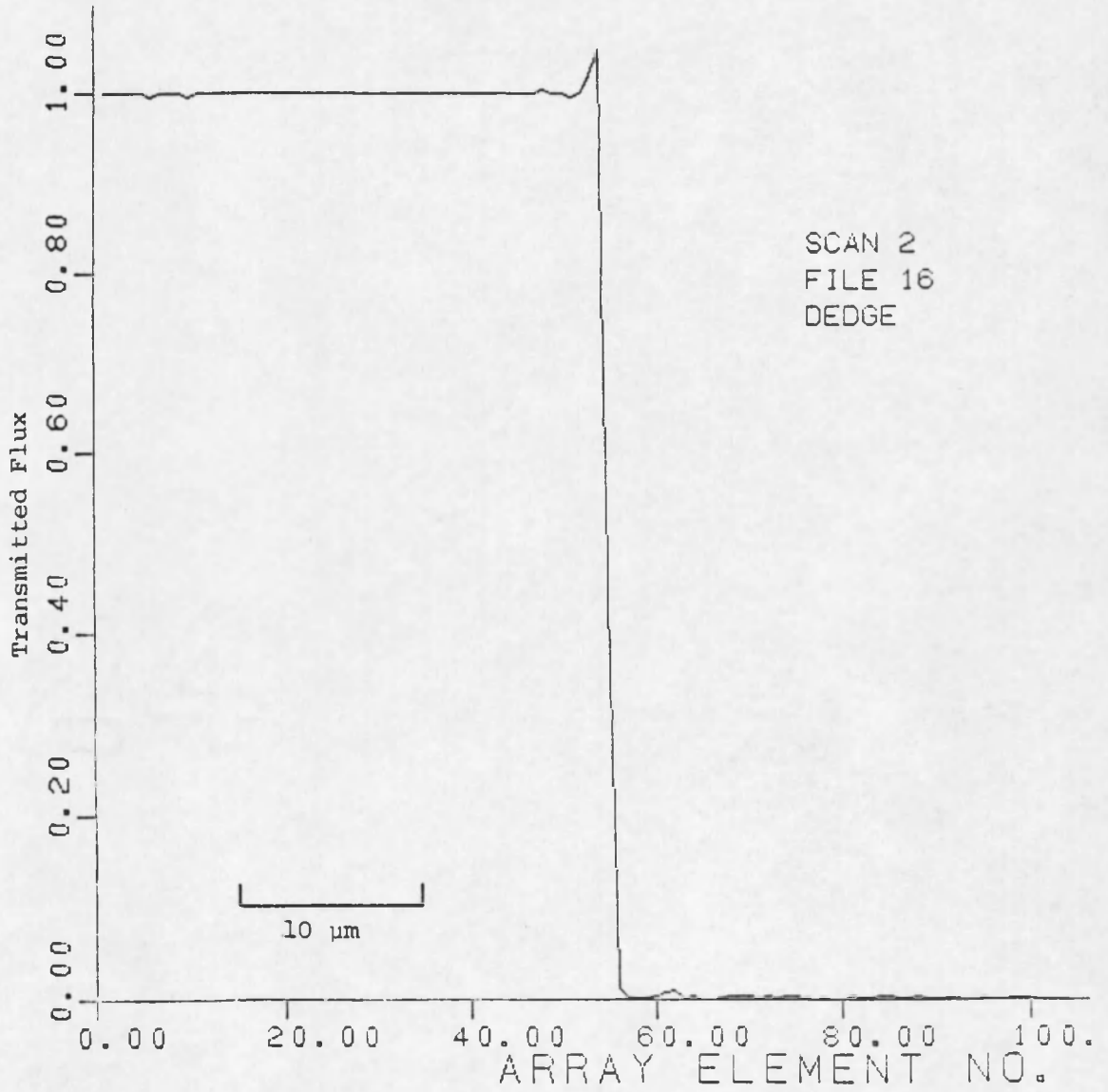
A computer program was written to calculate the area under an ideal Gaussian surface of revolution. The ideal surface is cut by a plane perpendicular to the x axis and the area under the surface to the left of the plane is plotted as the plane is moved from -x to +x values. The best fitting computer-generated profile is superimposed on each of the measured curves. The computer-generated profiles were chosen to have a good fit along the portion of the measured



a. Scanned in the +x direction.

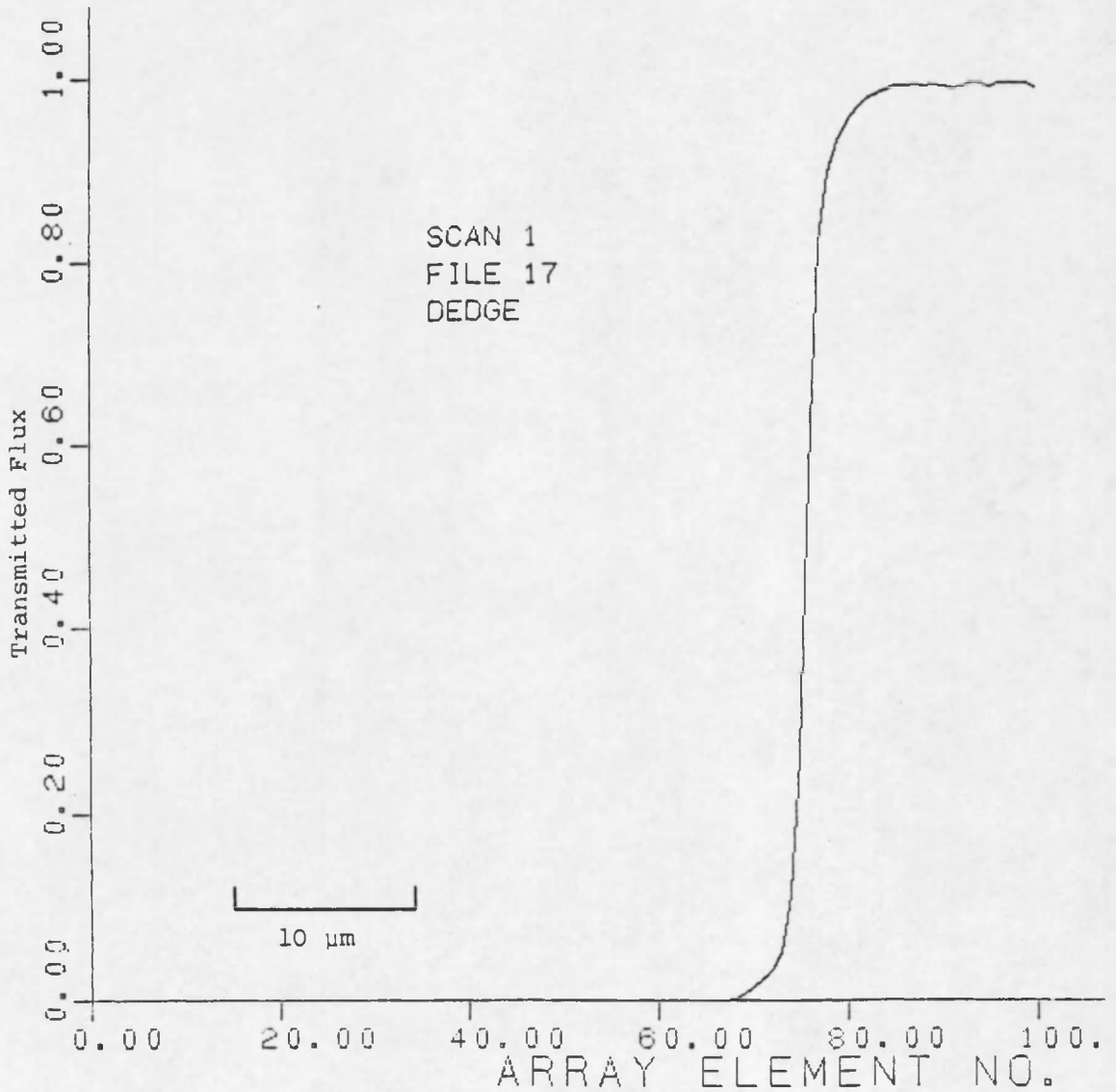
Figure 4.2. Results of scanning a razor blade across the Gaussian spot produced by the 20X microscope objective.

Scan object: Gillette super stainless razor blade
 Influx objective: 20X (NA 0.45)
 Efflux objective: 10X (NA 0.25)
 Number of data points: 512
 Distance between data points: 0.5 μm .



b. Scanned in the -x direction.

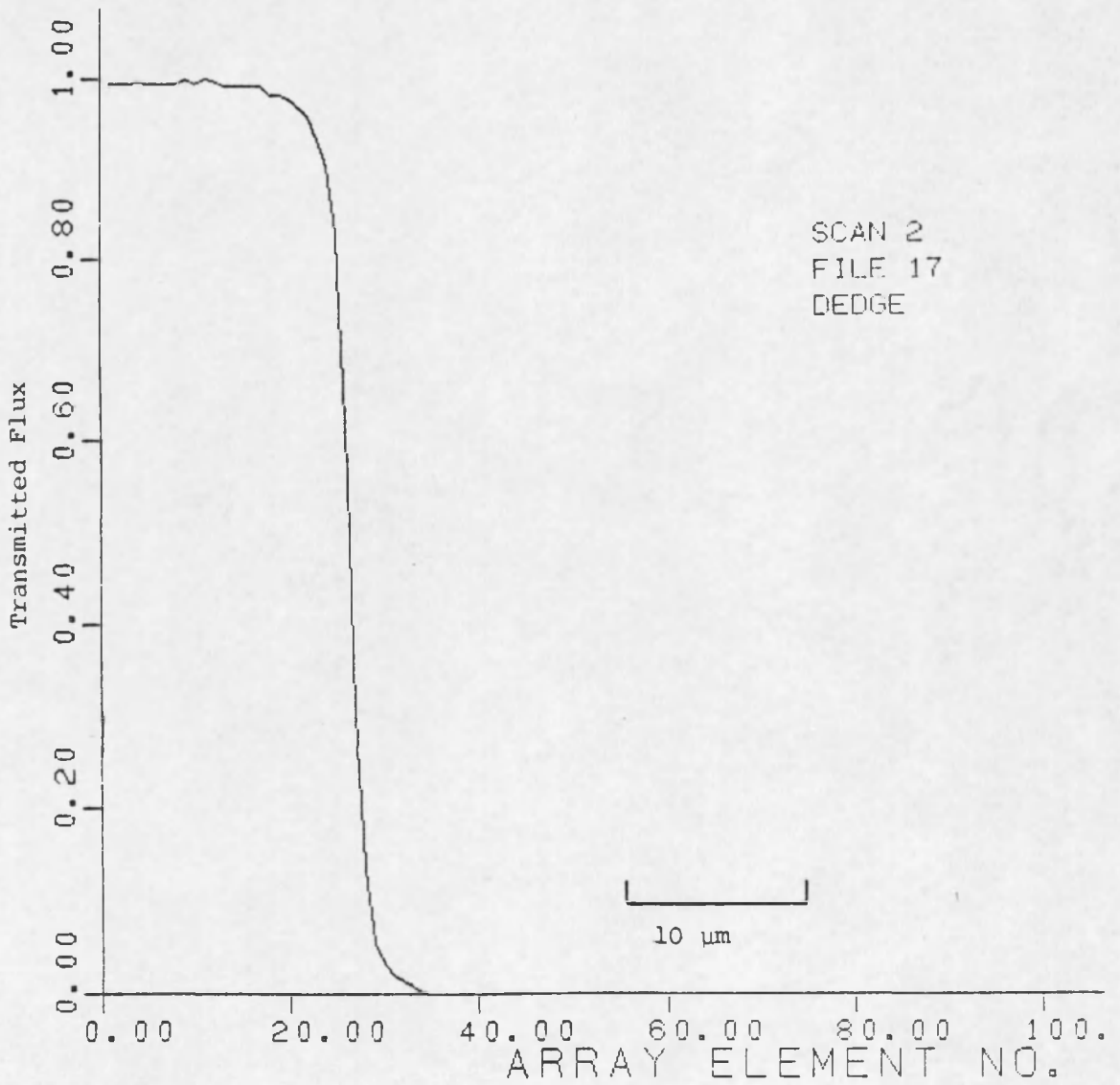
Figure 4.2, Continued.



a. Scanned in the +x direction.

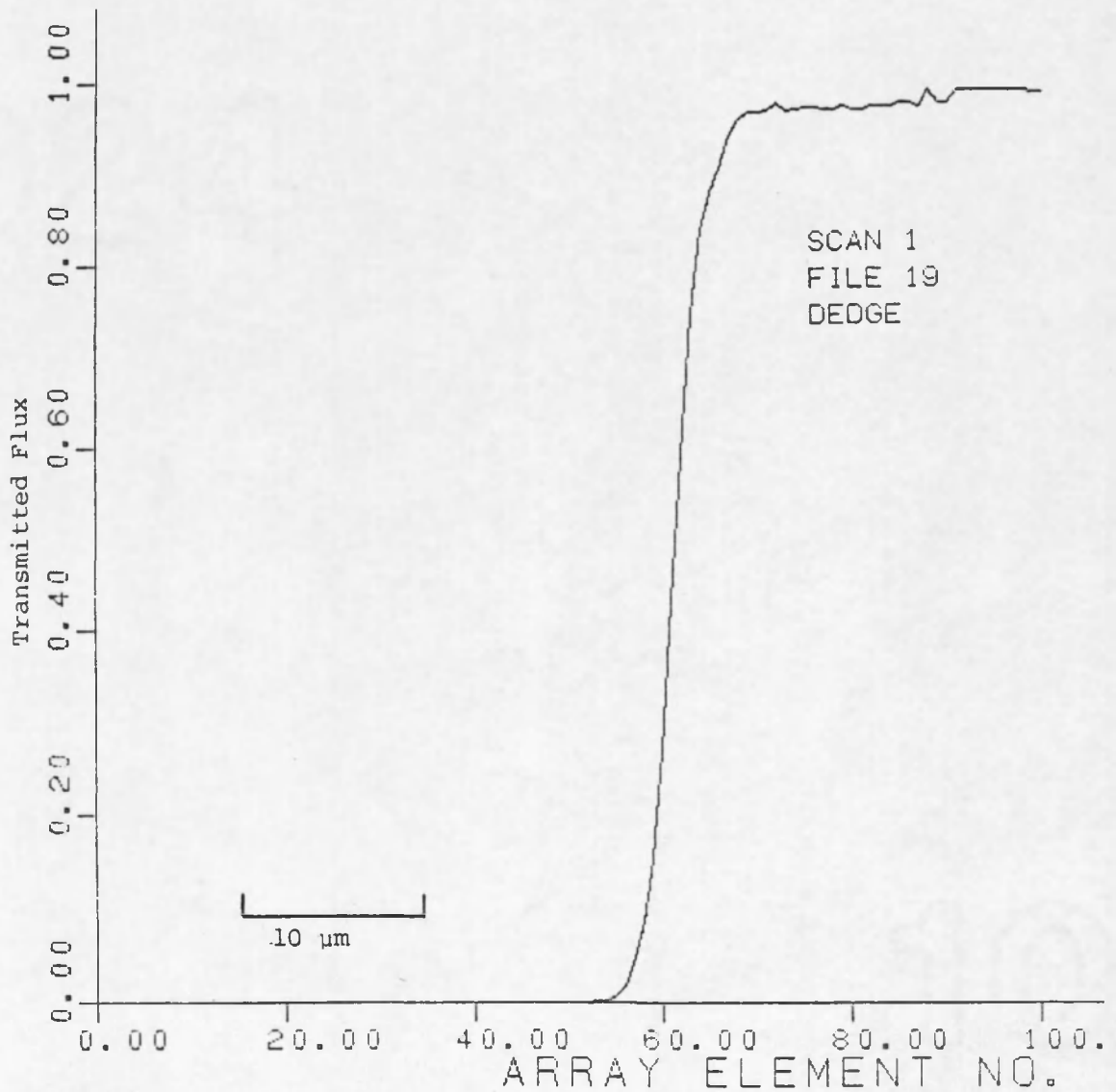
Figure 4.3. Results of scanning a razor blade across the Gaussian spot produced by the 10X microscope objective.

Scan object: Gillette super stainless razor blade
 Influx objective: 10X (NA 0.25)
 Efflux objective: 10X (NA 0.25)
 Number of data points: 512
 Distance between data points: 0.5 μ m.



b. Scanned in the -x direction.

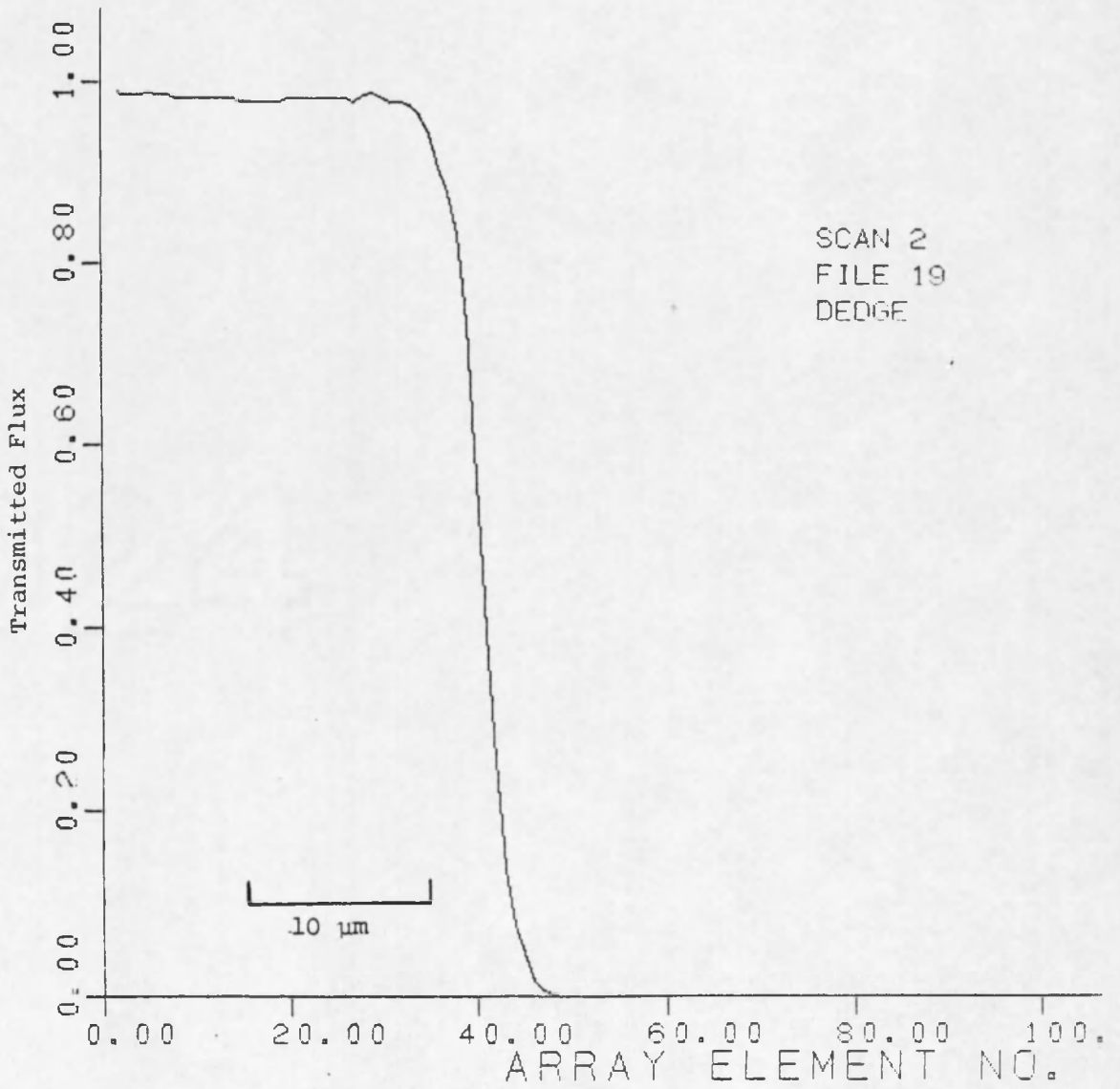
Figure 4.3, Continued.



a. Scanned in the +x direction.

Figure 4.4. Results of scanning a razor blade across the Gaussian spot produced by the 5X microscope objective.

Scan object: Gillette super stainless razor blade
Influx objective: 5X (NA 0.18)
Efflux objective: 10X (NA 0.25)
Number of data points: 512
Distance between data points: 0.5 μ m.



b. Scanned in the -x direction.

Figure 4.4, Continued.

Table 4.1. Diffraction limit vs actual spot size.

Influx NA	$R = \frac{\lambda}{2 \text{ NA}}$	$D = 2R$	Measured Diameter
0.18	1.76 μm	3.52 μm	3.8 μm
0.25	1.27 μm	2.53 μm	2.9 μm
0.45	0.70 μm	1.41 μm	1.5 μm

curve showing a fraction of a transmitted flux between 0.1 and 0.9. The departure of the measured curve at top or bottom is an indication of the amount of nonlinearity introduced by the microdensitometer system due to scattered light, diffraction effects, vignetting, flare, etc. Figures 4.5, 4.6 and 4.7 show the computer profiles superimposed on Figures 4.2a, 4.3a and 4.4a, respectively.

Because of the reasonable fit of the measured result to the computer-generated ideal curve for the cases of the 5X and 20X objective, we might have expected the 10X objective to produce better agreement near the endpoints. Swing (1976a, p. 564) reports otherwise. The curves presented here support Swing's contention that "matched numerical apertures do not lead to linear system response except when the sample has no frequency content (i.e., the sample is a uniform distribution of optical density.)"

The razor blade was replaced as scan object by an edge on film provided by Professor P. N. Slater. The edge is a contact print of a razor blade made on 35 mm Kodak 649F holographic negative film. Three curves of measured data obtained from the film edge are shown in Figures 4.8, 4.9 and 4.10. The 20X objective was chosen as the influx objective in order to obtain the smallest light probe. Figure 4.8 shows the results of scanning the film edge using the 5X objective as the efflux objective. The apparent width of the film edge is 3.3 μm . The fluctuations in the plot at the high transmission portion of the graph are probably due to grains that cause fog in the unexposed portion

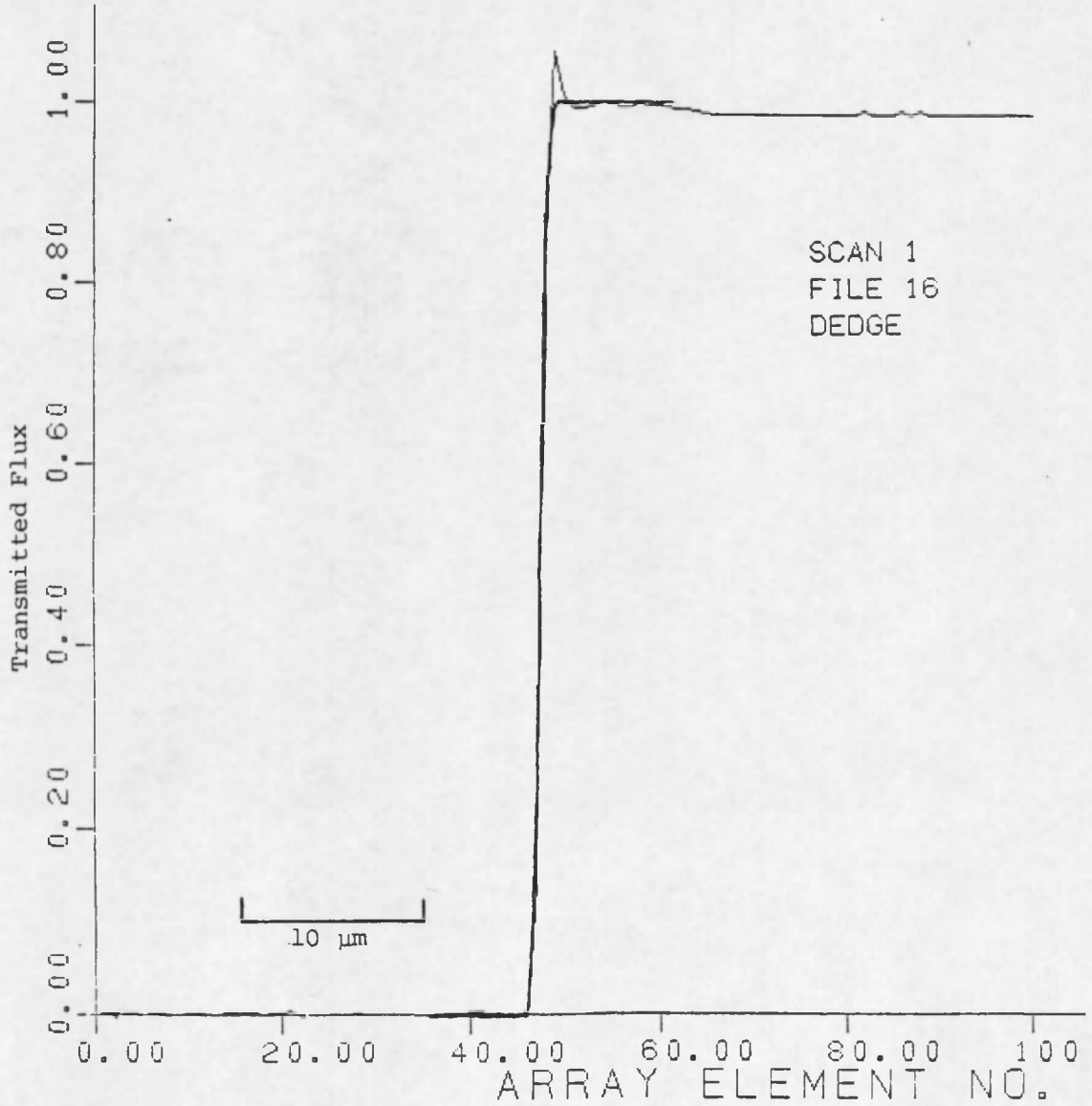


Figure 4.5. Computer generated curve of the area under an ideal Gaussian surface versus razor blade position superimposed on Figure 4.2a.

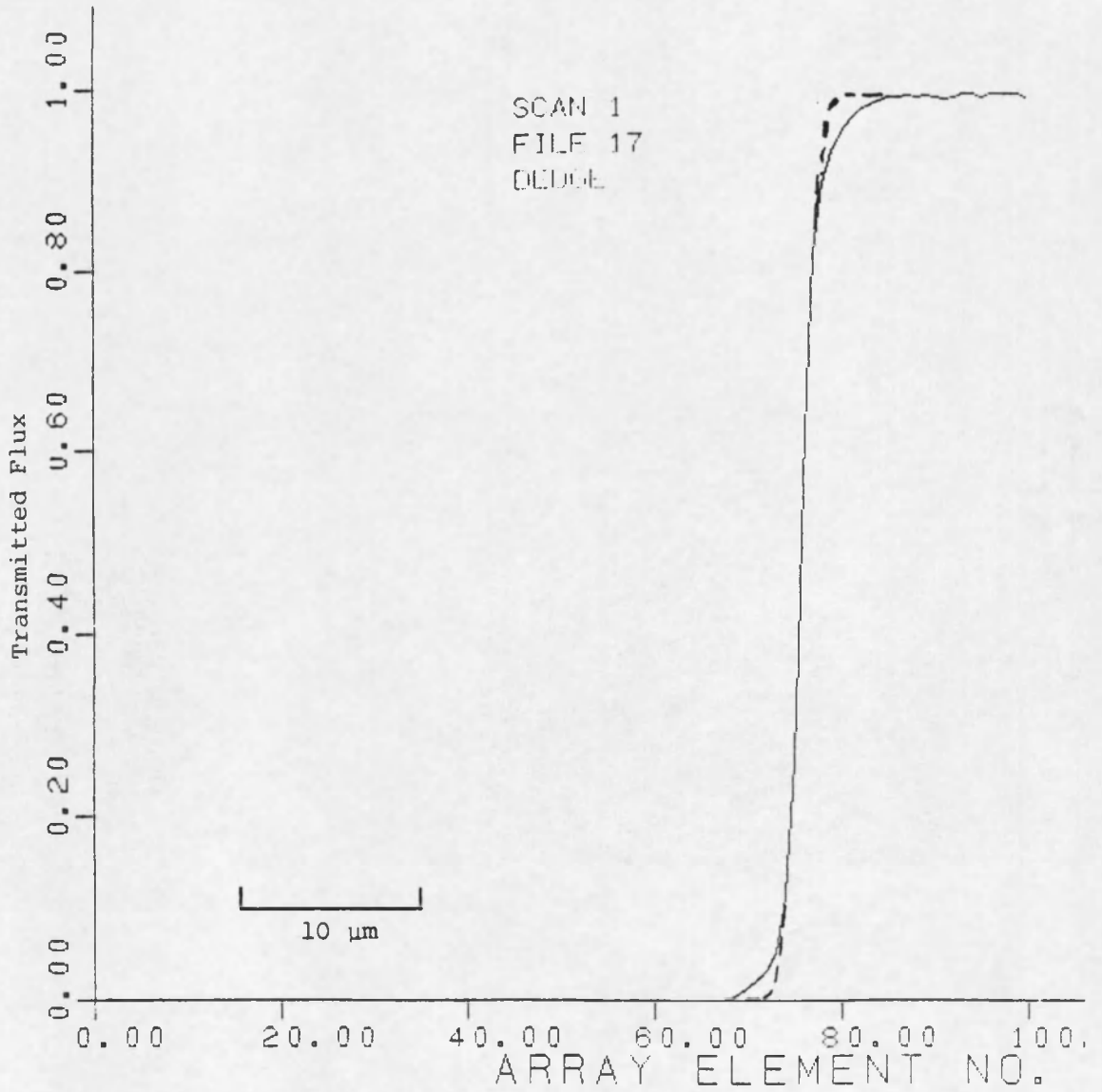


Figure 4.6. Computer generated curve of the area under an ideal Gaussian surface versus razor blade position superimposed on Figure 4.3a.

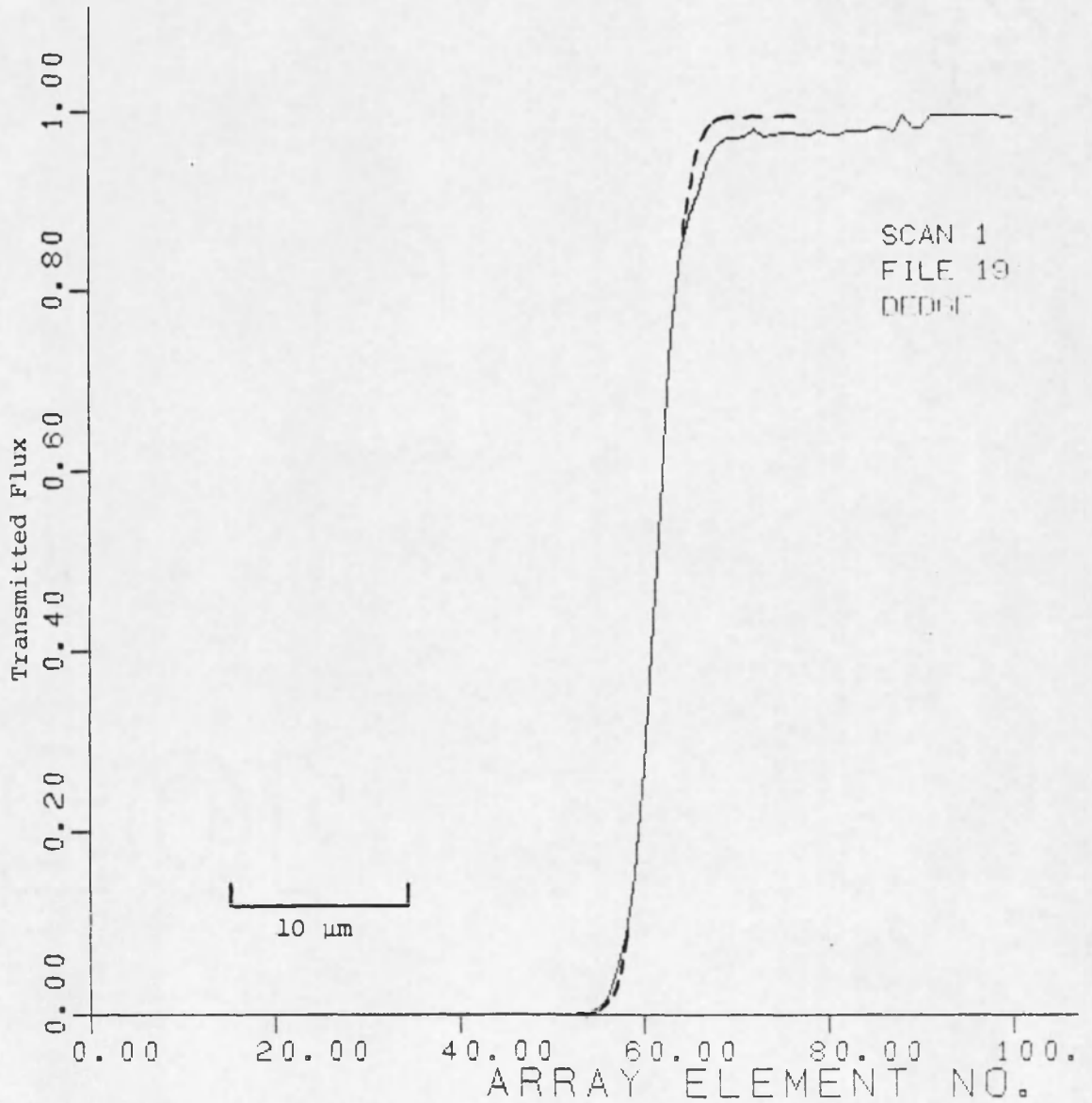


Figure 4.7. Computer generated curve of the area under an ideal Gaussian surface versus razor blade position superimposed on Figure 4.4a.

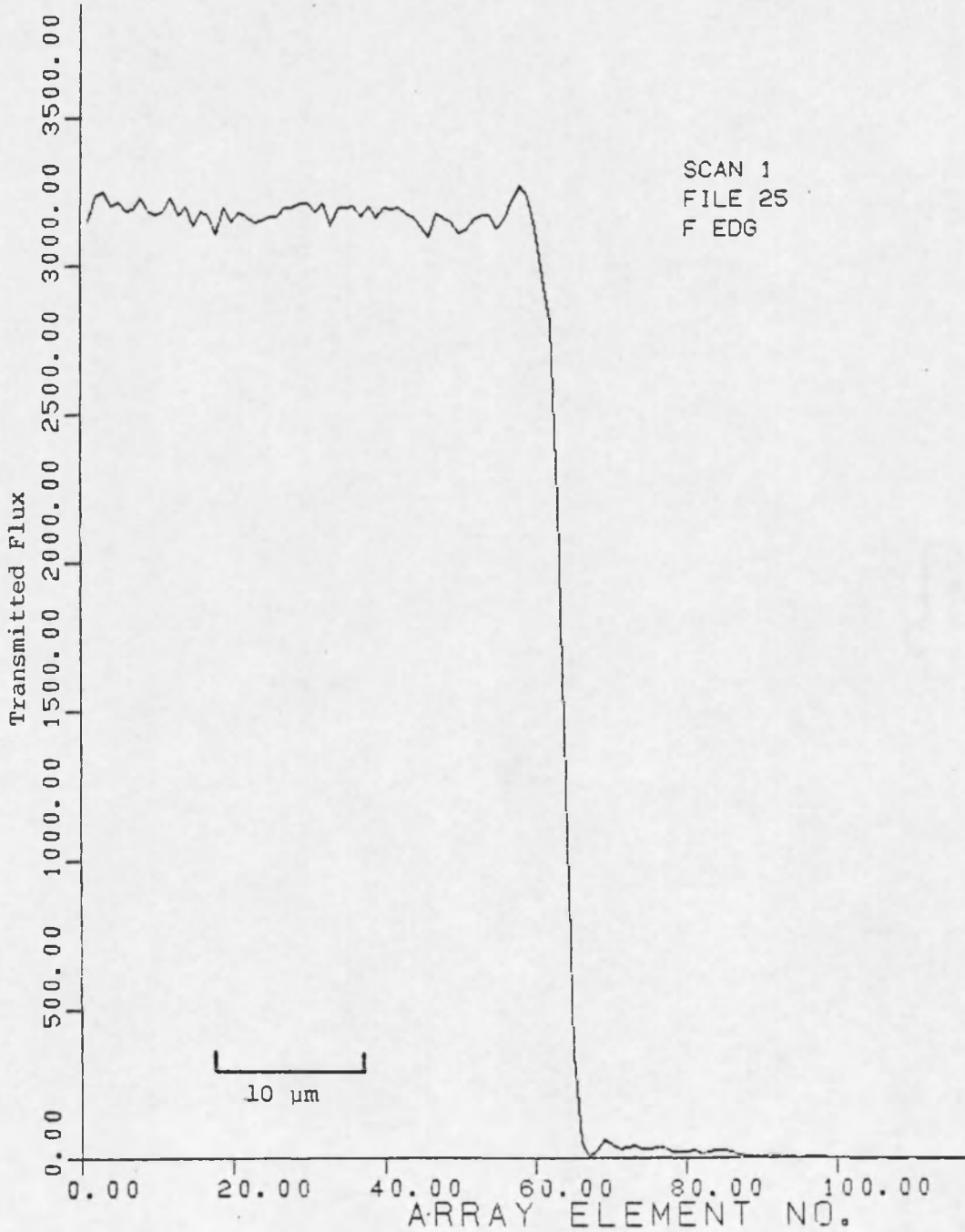


Figure 4.8. Results of scanning a film edge across the Gaussian spot produced by the 20X microscope objective. Efflux objective is the 5X microscope objective.

Scan object: Edge on Kodak 649F holographic film
Influx objective: 20X (NA 0.45)
Efflux objective: 5X (NA 0.18)
Number of data points: 512
Distance between data points: 0.5 μm .

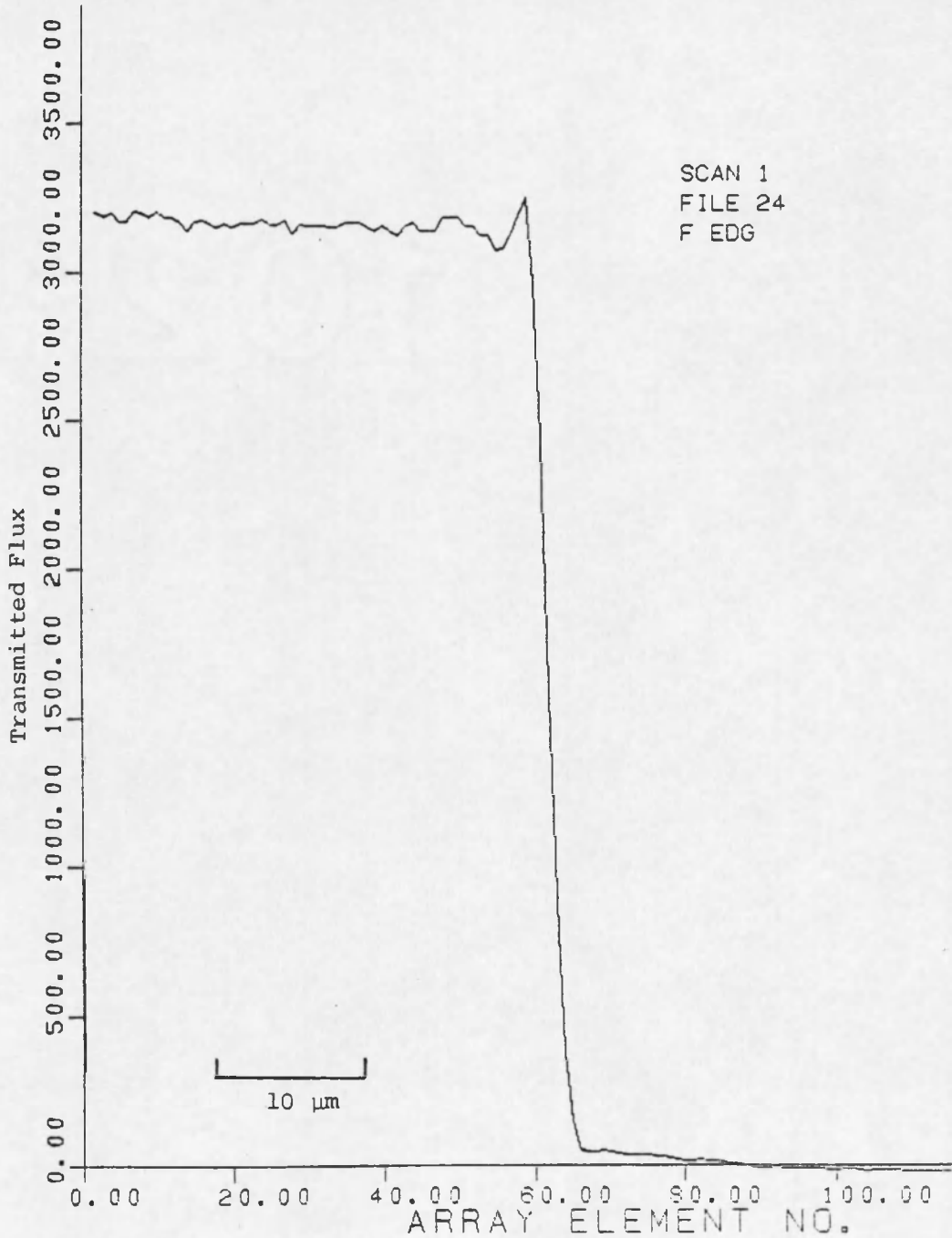


Figure 4.9. Results of scanning a film edge across the Gaussian spot produced by the 20X microscope objective. Efflux objective is the 10X microscope objective.

Scan object: Edge on Kodak 649F holographic film
Influx objective: 20X (NA 0.45)
Efflux objective: 10X (NA 0.25)
Number of data points: 512
Distance between data points: 0.5 μm .

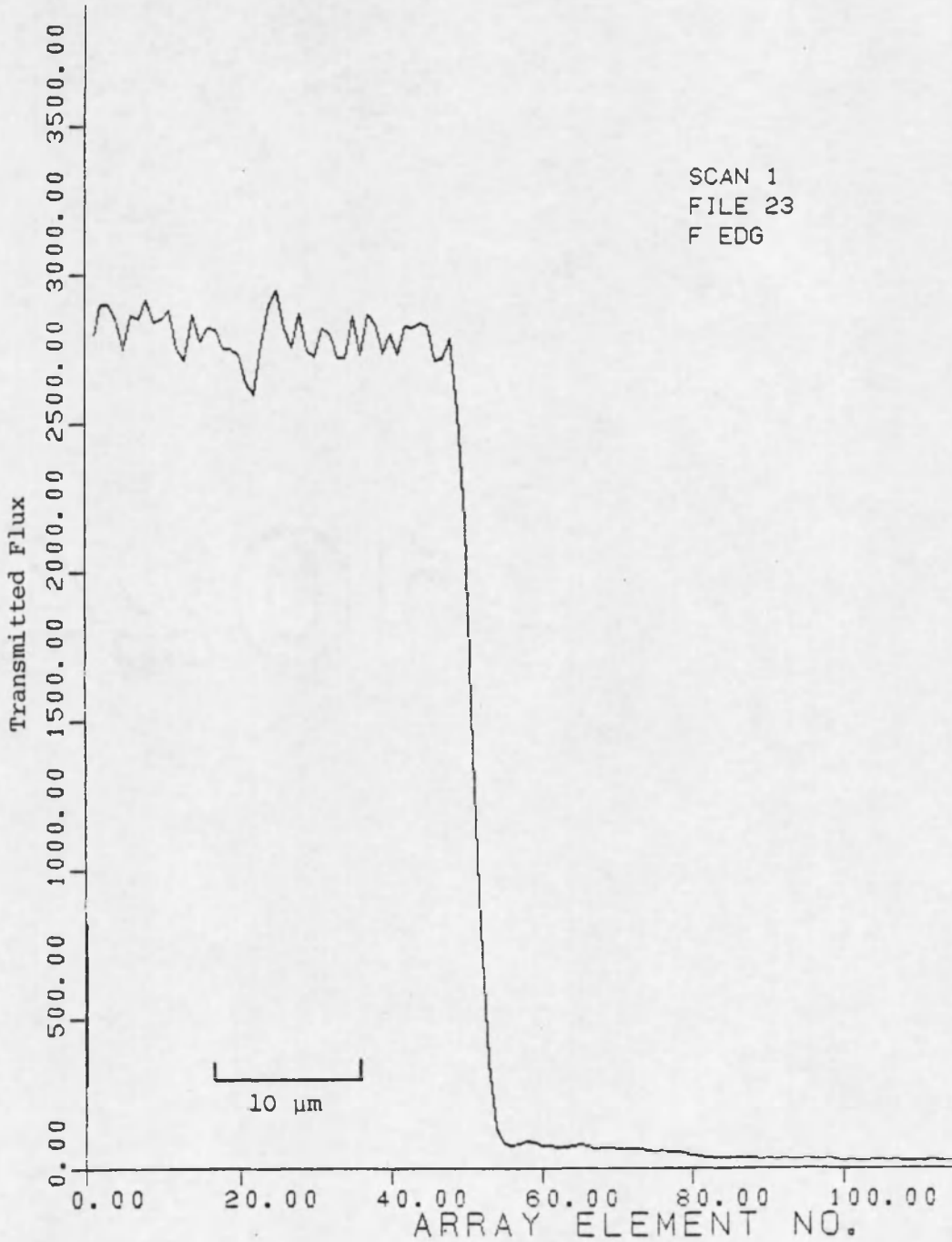


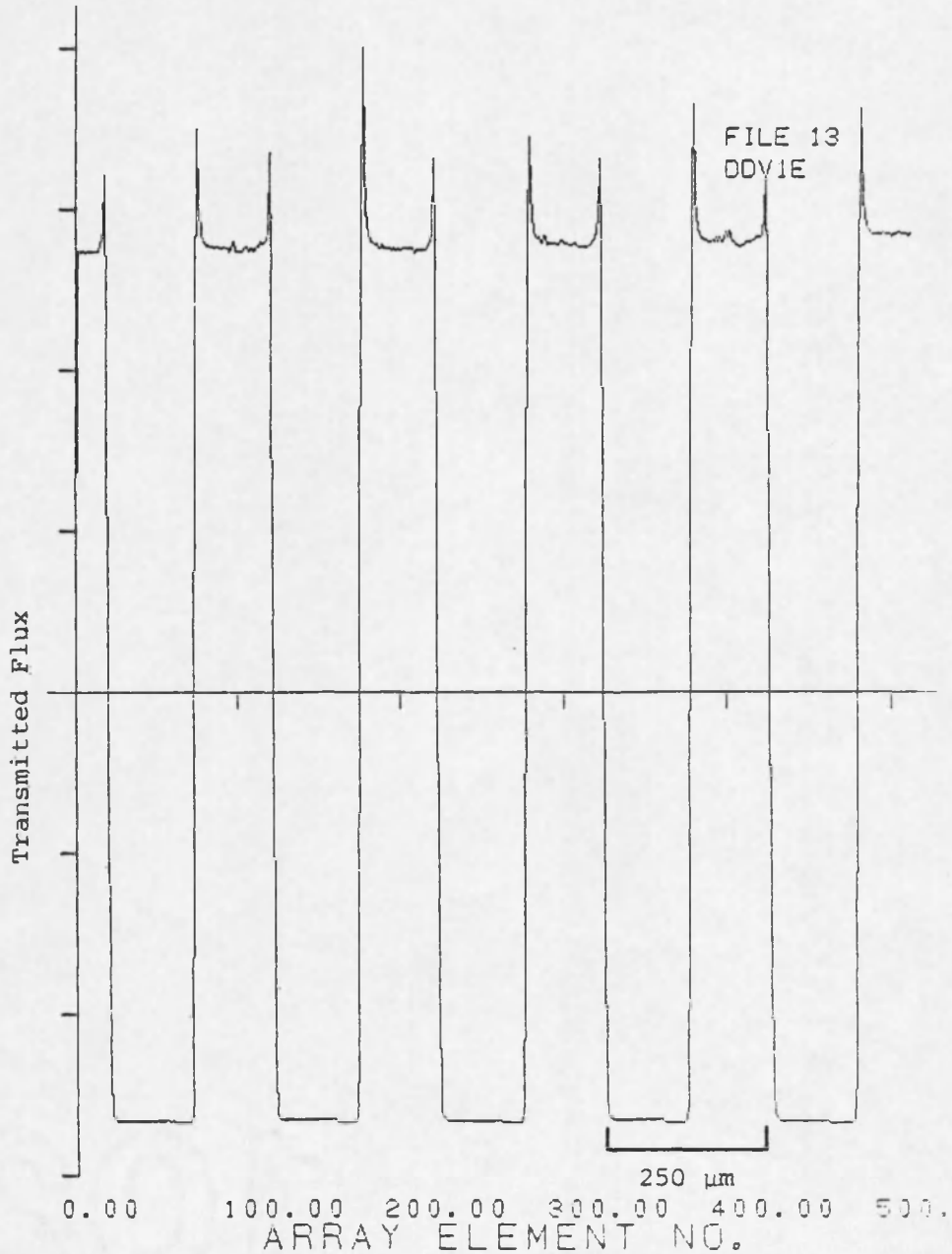
Figure 4.10. Results of an independent scan of the film edge under the same conditions as Figure 4.9.

Scan object: Edge on Kodak 649F holographic film
Influx objective: 20X (NA 0.45)
Efflux objective: 10X (NA 0.25)
Number of data points: 512
Distance between data points: 0.5 μm .

of the negative. Figures 4.9 and 4.10 are the results of scanning the same edge using the 10X objective as the collecting optic. The film edge again has an apparent width of $3.3 \mu\text{m}$.

The peak evident at the high transmission end of the edge was evident in the razor blade scans with the microdensitometer similarly configured (influx objective = 20X, efflux objective = 10X). However, such a pronounced local minimum adjacent to the peak did not appear in the razor blade case.

To verify the gross characteristics of the microdensitometer, two Ronchi rulings provided by Mr. Richard Sumner of the Optical Sciences Center were scanned. The scan pattern consisted essentially of two scans normal to the rulings. Each scan contains 512 data points. The first scan is in the +x direction with $2.5 \mu\text{m}$ between data points. The second scan is in the -x direction but displaced from the first by $25 \mu\text{m}$ in the y direction. No direction-dependent differences were expected and none were observed. Figure 4.11 shows the results of scanning a Ronchi ruling that has 100 lines/inch or 1 line per 0.254 mm. With a data point every $2.5 \mu\text{m}$ we would expect to see one period of the ruling completed in 101.6 data points or 5 periods completed in 508 data points. Figure 4.12 shows the results of scanning a Ronchi ruling having 300 lines/inch or 1 line per 0.0847 mm. We would expect to see a ruling period every 33.87 data points or 15.1 periods across the 512 data points sampled. The figures present the data in zero mean format with the highest transmission peak normalized to 1.0. Note that the abscissa does not divide the figures at the midpoint between maximum and minimum



a. Scanned in the +x direction.

Figure 4.11. Results of scanning a Ronchi ruling containing 100 lines/inch across the Gaussian spot produced by the 20X microscope objective.

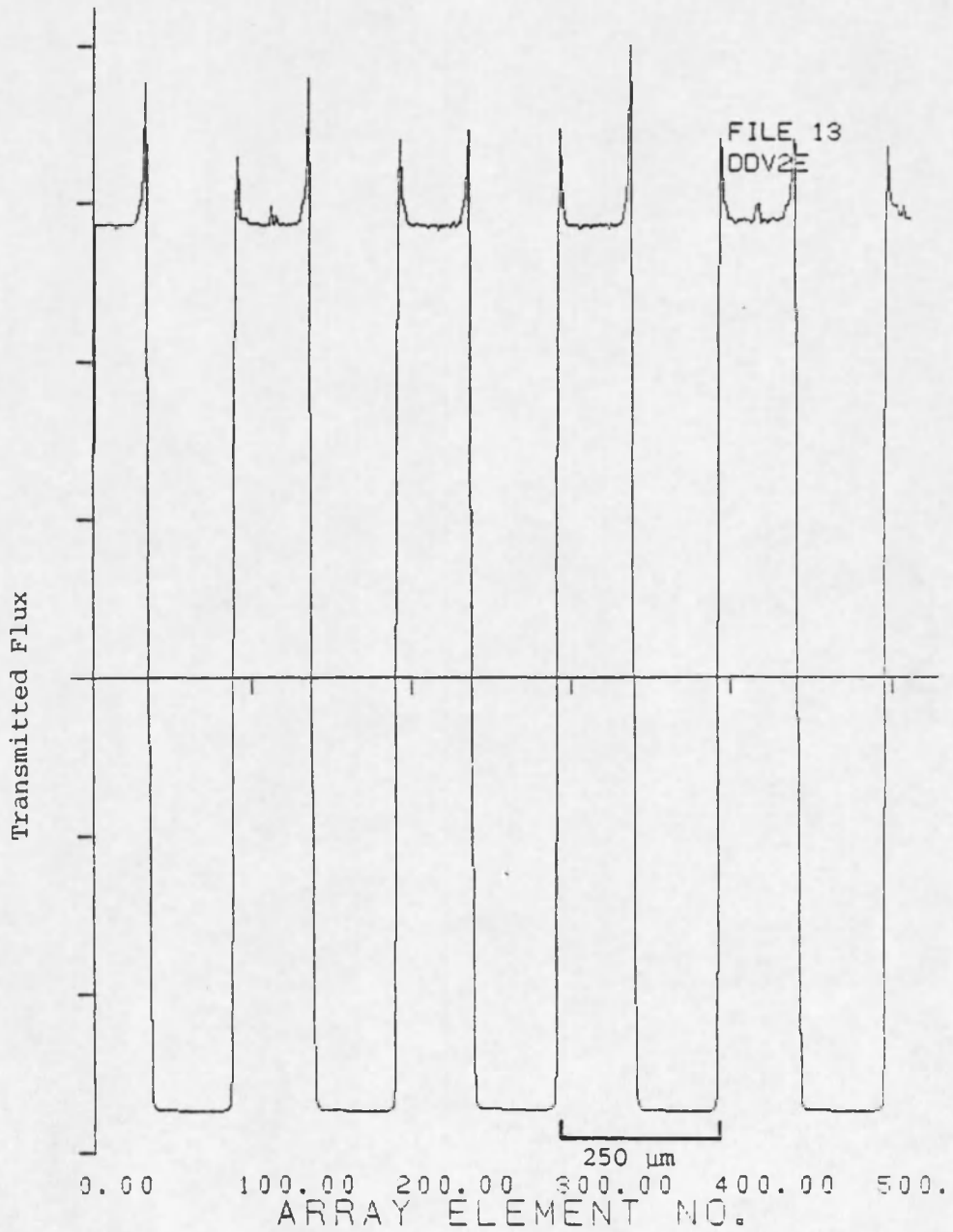
Scan object: Ronchi ruling, 100 lines/inch
Edmund Scientific #30518

Influx objective: 20X (NA 0.45)

Efflux objective: 10X (NA 0.25)

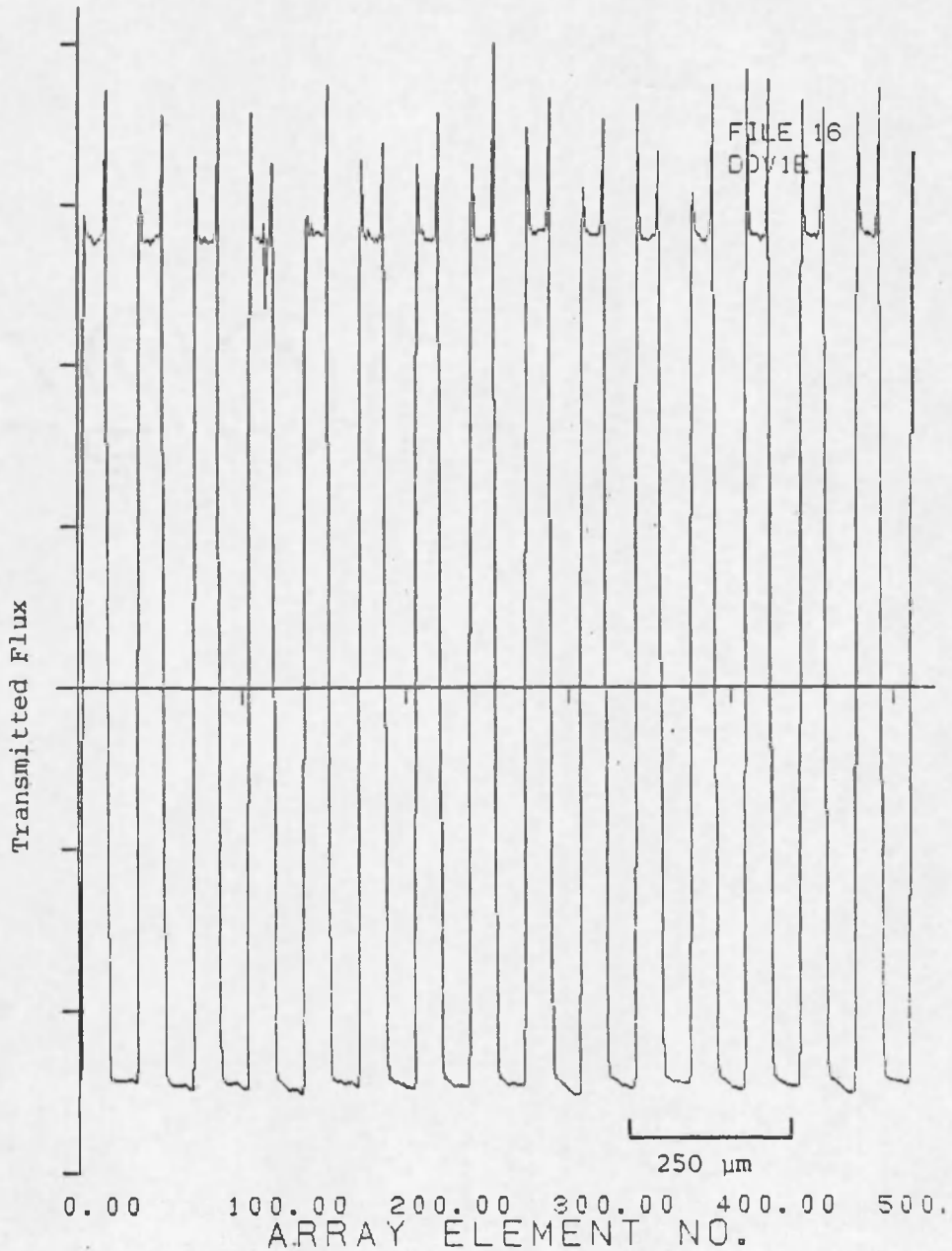
Number of data points: 512

Distance between data points: 2.5 μm .



b. Scanned in the -x direction.

Figure 4.11, Continued.



a. Scanned in the +x direction.

Figure 4.12. Results of scanning a Ronchi ruling containing 300 lines/inch across the Gaussian spot produced by the 20X microscope objective.

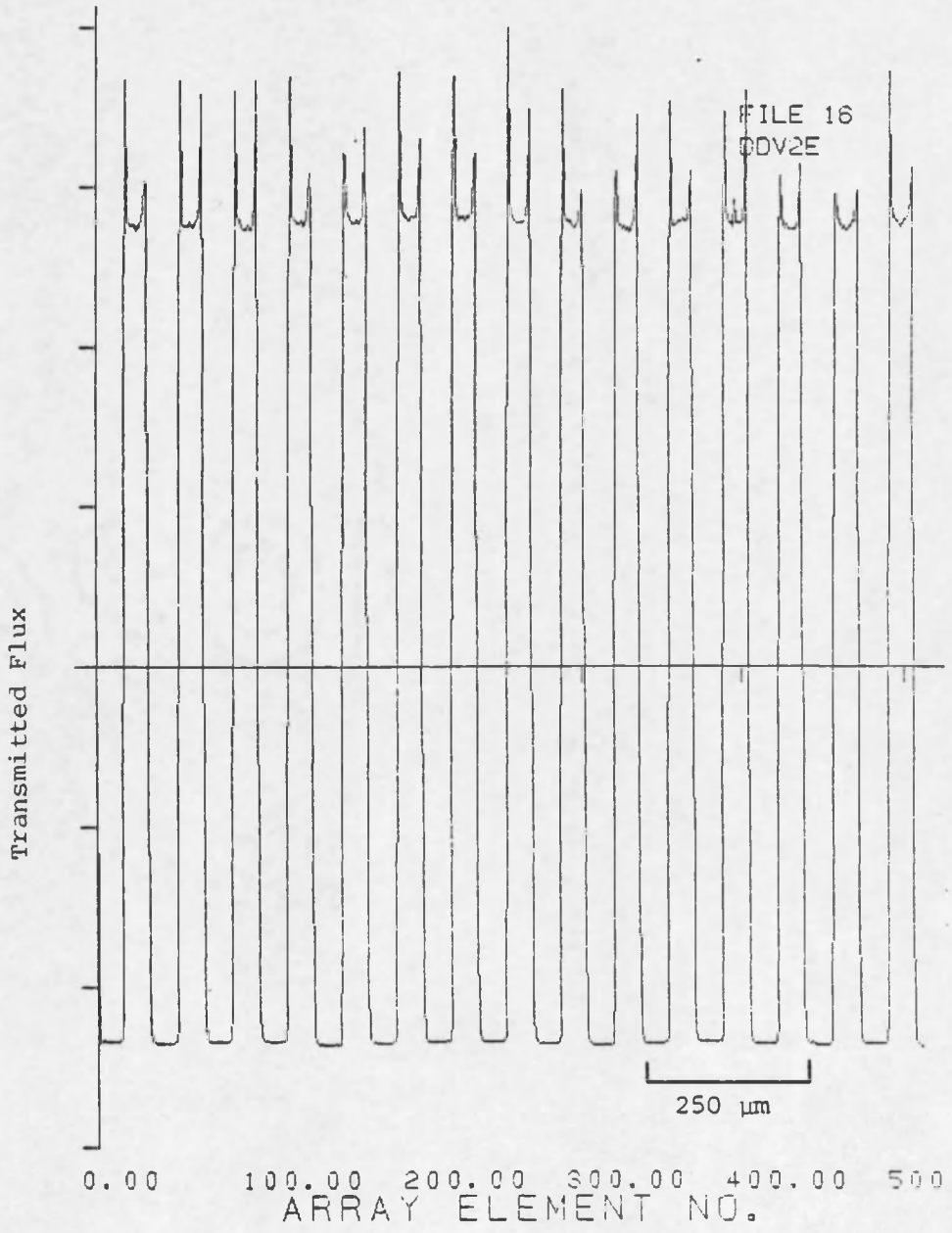
Scan object: Ronchi ruling, 300 lines/inch
Edmund Scientific #30513

Influx objective: 20X (NA 0.45)

Efflux objective: 10X (NA 0.25)

Number of data points: 512

Distance between data points: 2.5 μm .



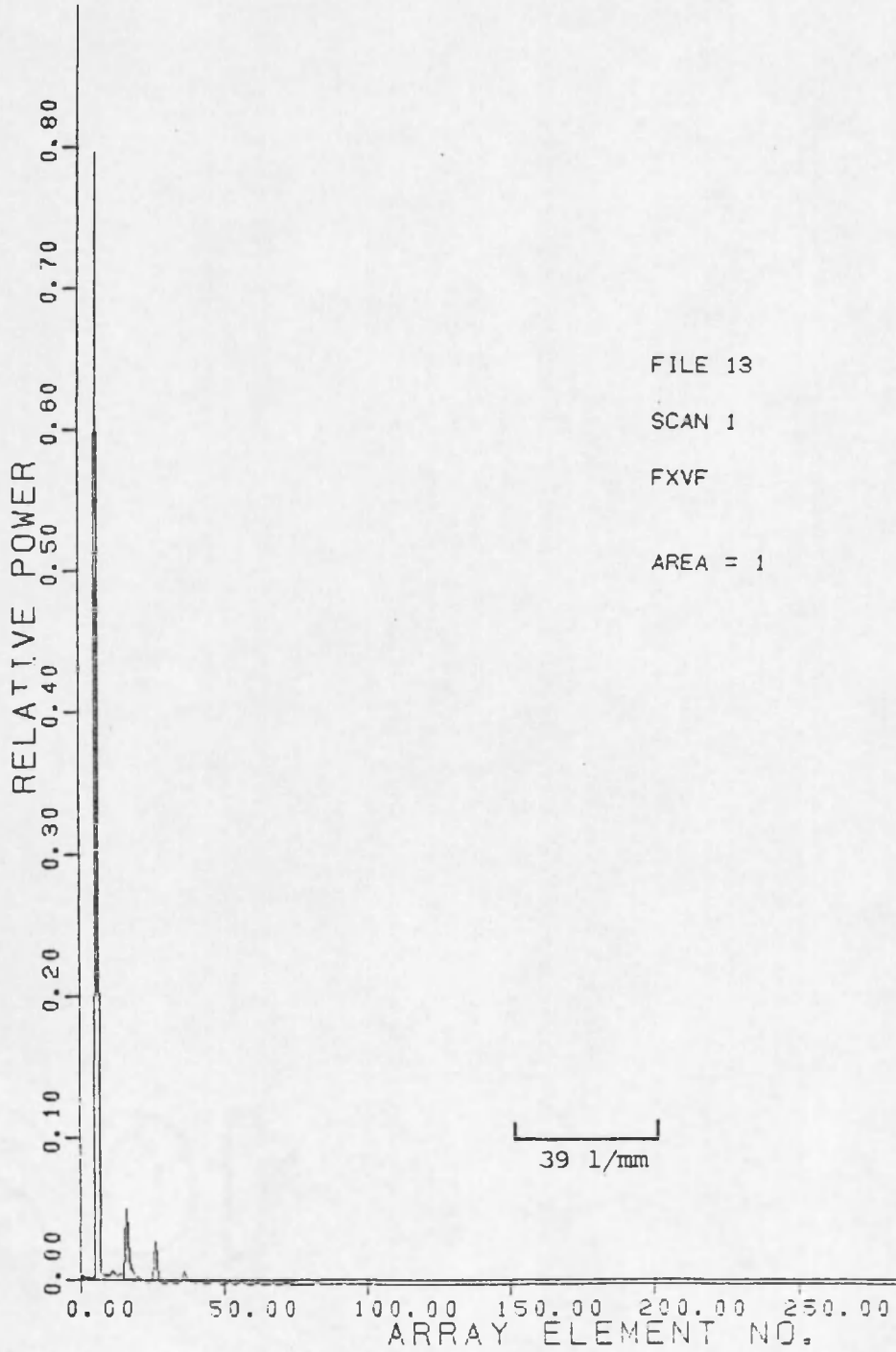
b. Scanned in the -x direction.

Figure 4.12, Continued.

values. Closer inspection reveals that this is largely because the duty cycle of the ruling is not 50%, and partly because of the presence of the peaks at the edges of the transmission maxima. These peaks can be manifestations of the diffraction effect at the opaque edge but can also be caused in part by physical changes in the glass at the transmission boundary.

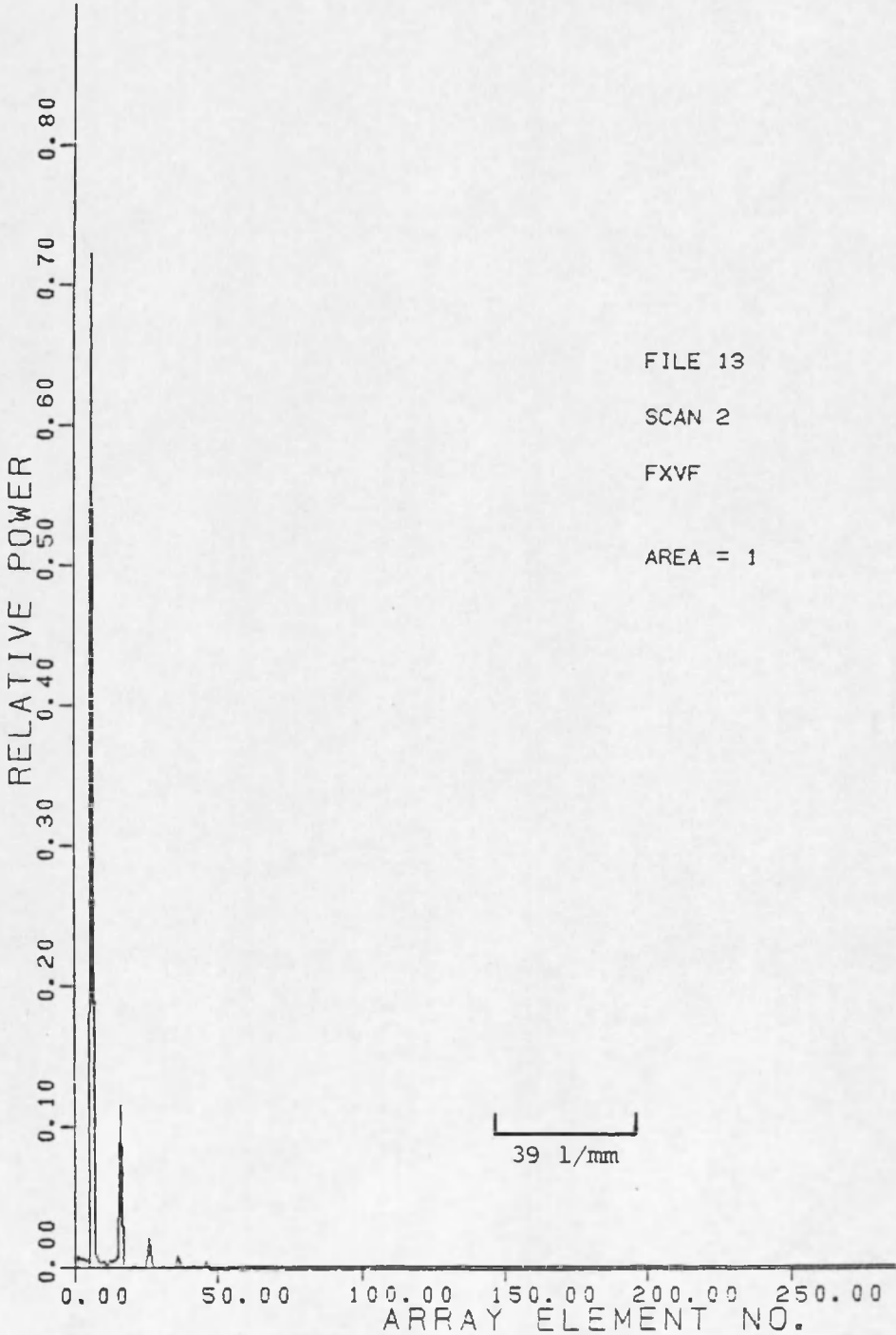
To establish confidence in the Fourier transform routine, the data obtained by scanning the Ronchi rulings was analyzed by a program that windowed the data within 10% of first and last data point with an elevated cosine function, calculated the FFT of the resulting input array and plotted the results. The transform of the windowed data in Figure 4.11 is shown in Figure 4.13. Similarly, the transform of the data shown in Figure 4.12 appropriately windowed is given in Figure 4.14. We expect the transform to resemble the transform of a square wave to the extent that the finite sample of the Ronchi ruling approximates a square wave. The actual transform agrees well with the expected result. The correct fundamental frequency and its third, fifth and seventh harmonics are observed. The relative amplitude of each component is within reasonable agreement with the expected value. A small amount of each even harmonic is present; this is because the duty cycle of the Ronchi ruling is not exactly 50%. The frequency components have some width rather than being delta functions at the appropriate frequencies; this is as we would expect owing to the finiteness of the data sample.

A sample of Dupont Cronex x-ray film was provided by Dr. Hans Roehrig of the Optical Sciences Center. The film had been exposed



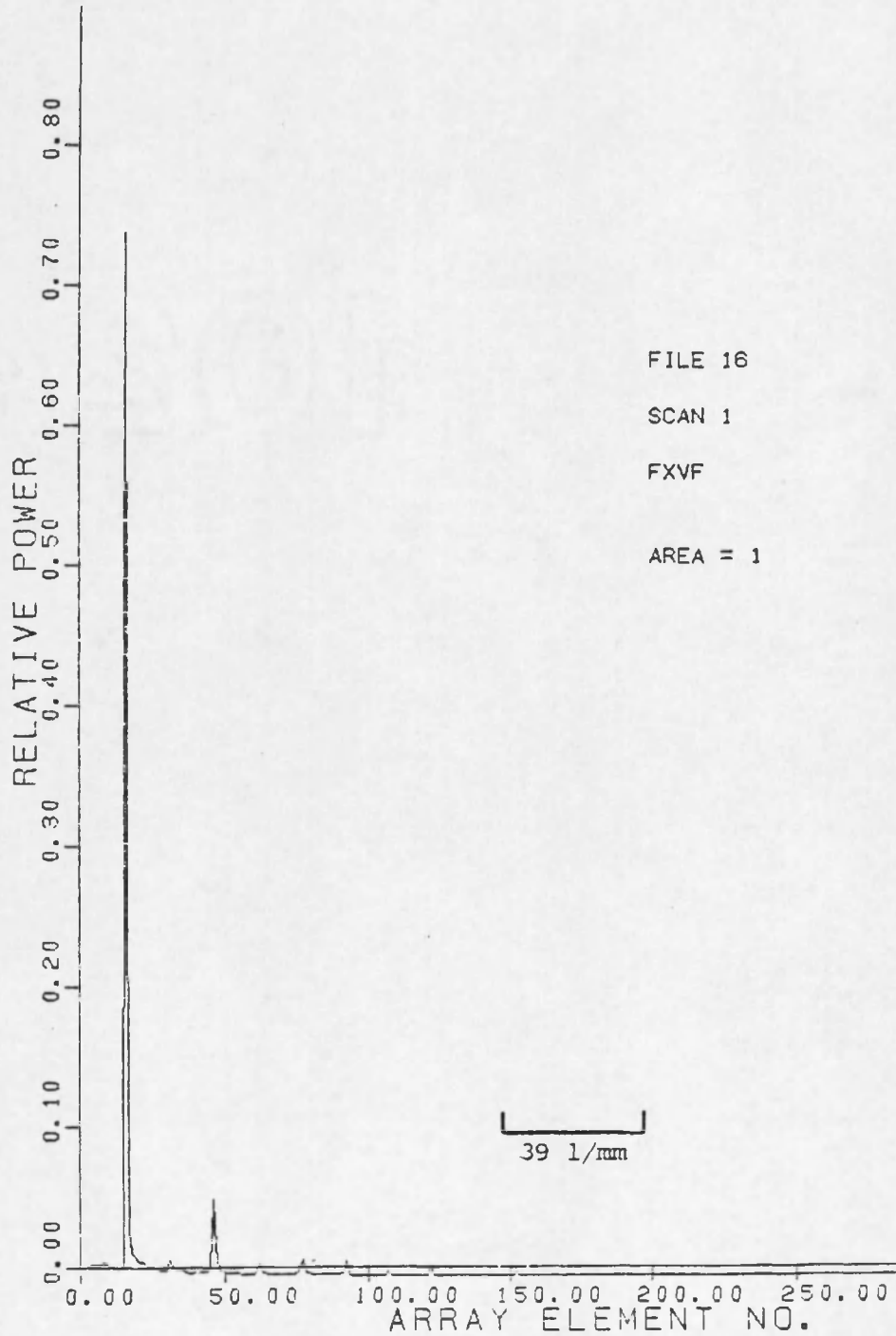
a. From transmission in (a) of Figure 4.11.

Figure 4.13. Power spectrum of the transmission data of the 100 line/inch Ronchi ruling shown in Figure 4.11.



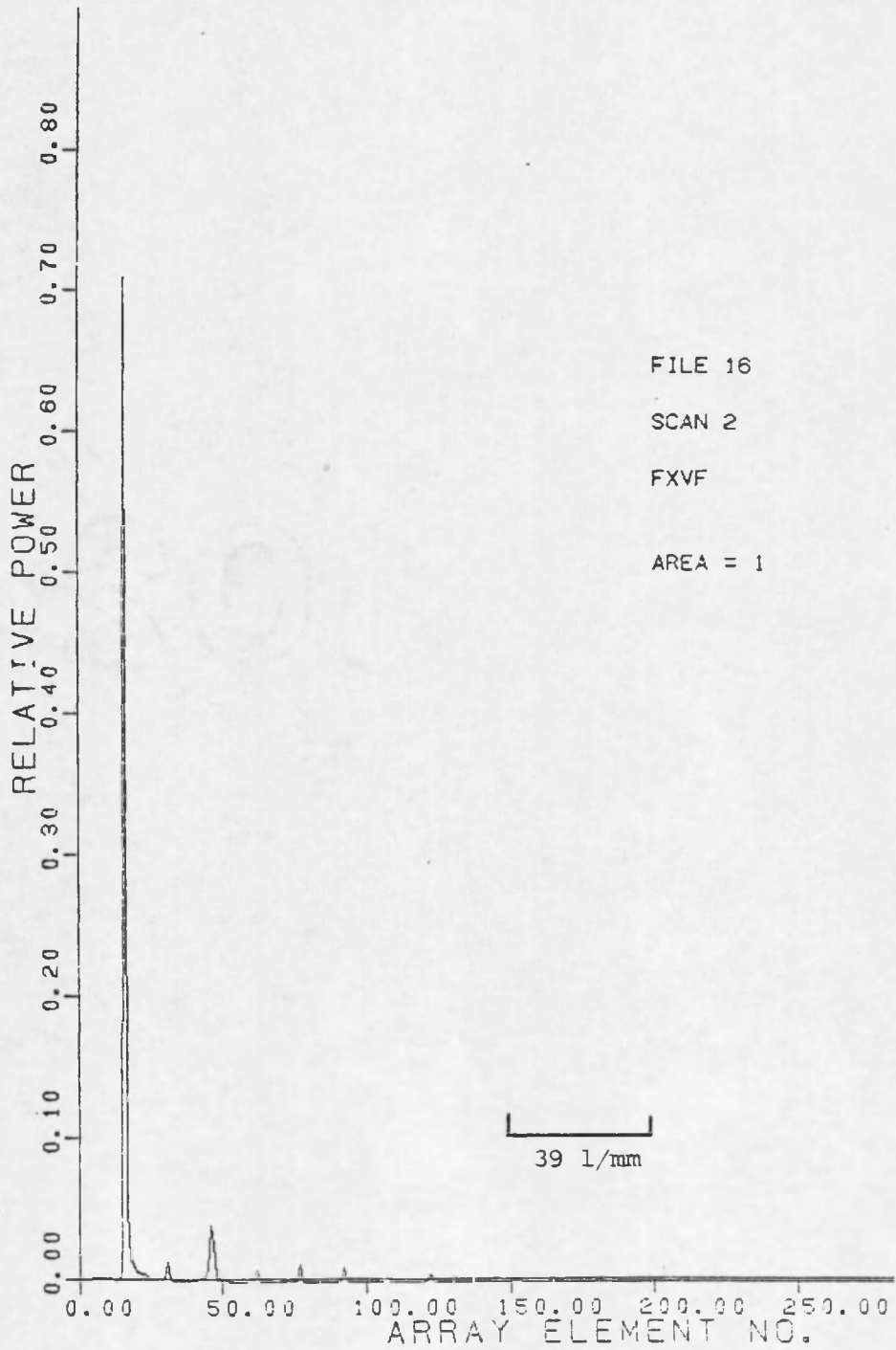
b. From transmission in (b) of Figure 4.11.

Figure 4.13, Continued.



a. From transmission in (a) of Figure 4.12.

Figure 4.14. Power spectrum of the transmission data of the 300 line/inch Ronchi ruling shown in Figure 4.12.



b. From transmission in (b) of Figure 4.12.

Figure 4.14, Continued.

using the "Lo Dose" film screen system under the following conditions: 80 kVp, 0.25 mAs, 107 inch, 1.3 mm focal spot. The resulting negative had a uniform density of approximately 1.18. Several scans were made of different locations on the sample. On initial scans of the sample, clipping occurred at 10 or more points in a 512 data-point run, indicating that the photodiode-instrumentation amplifier combination or the A/D converter had become saturated. The laser source was polarized and a sheet of polaroid material was used to reduce the amount of light available to the system to a value that would guarantee that the photodiode-instrumentation amplifier combination would not saturate. The sample was scanned without recording data, and the A/D converter input voltage was monitored on a voltmeter. The gain of the operational amplifier was adjusted so that the maximum value that occurred in this preliminary scan caused an input of approximately 8.0 V at the A/D input. By this adjustment, a voltage 75% in excess of the expected minimum value could occur without saturating the detection and digitizing circuits and thereby invalidating the data. The mean of the data was subtracted from each data point in a data set, and the data was normalized so that the maximum value was 1.0.

To investigate the repeatability of measurements we recorded a scan sequence which produced the rectangular scan pattern diagrammed in Figure 4.15 on a cassette. This scan sequence collected 10 data points 2.5 μm apart in the +y direction, then 512 data points 2.5 μm apart in the -x direction and finally 20 data points 2.5 μm apart in the -y direction returning the stage to the origin.



Figure 4.15. Rectangular scan pattern.

Two independent rectangular scans were made of the same section of film without any adjustment made to the equipment. The 512 data points in the $+x$ direction from each of the two scans are plotted in Figures 4.16 and 4.17. The 512 data points in the $-x$ direction from each of the two scans are plotted in Figures 4.18 and 4.19. Major peaks occur in the same spatial positions. Corresponding peaks in Figures 4.16 and 4.17 are numbered to aid in comparing the figures, as are corresponding peaks in Figures 4.18 and 4.19. The amplitudes do not match exactly, but the difference in amplitude can be accounted for by

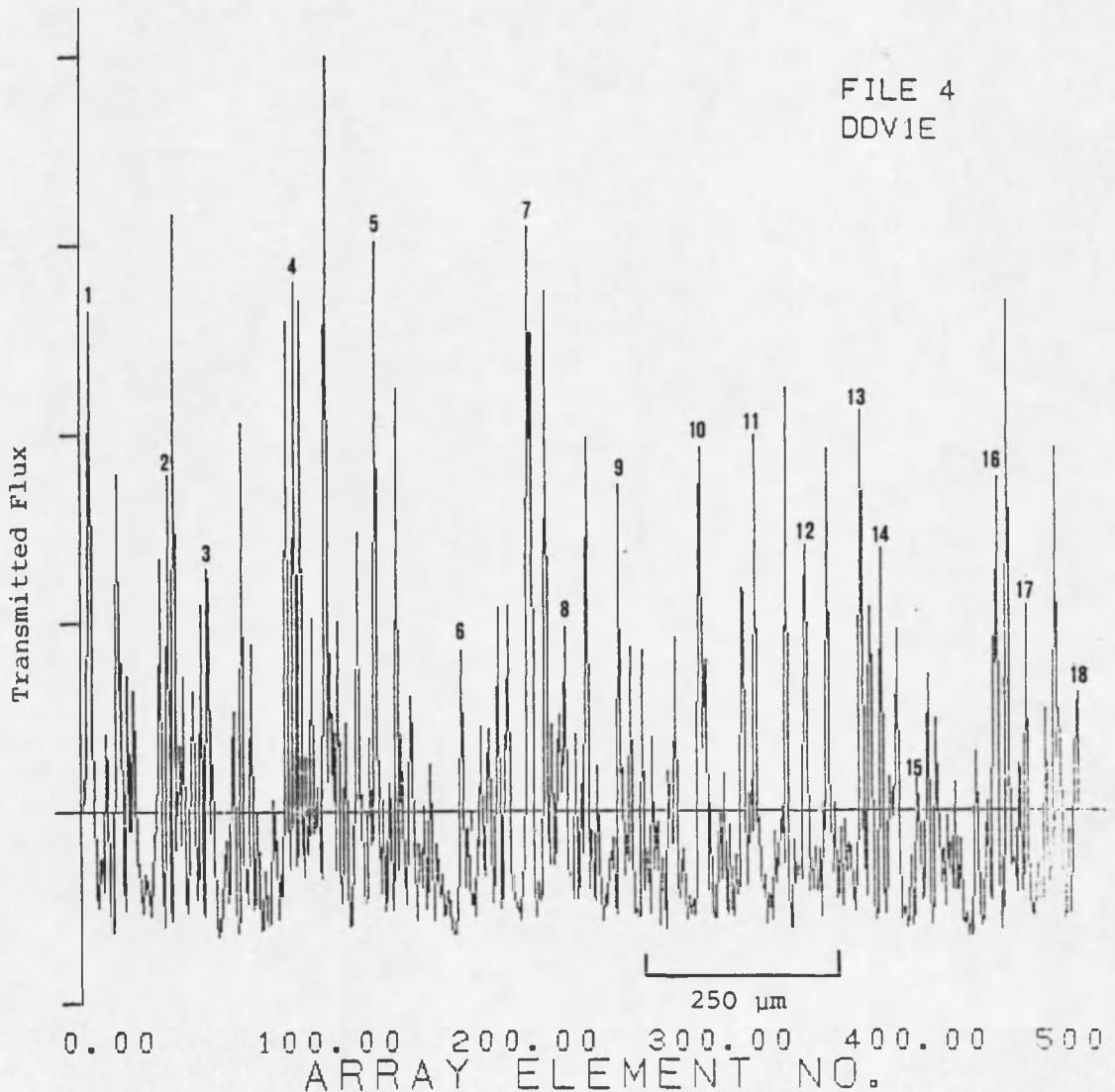


Figure 4.16. Results of scanning a sample of Dupont Cronex x-ray film in the +x direction of the scan pattern shown in Figure 4.15.

Scan object: Dupont Cronex x-ray film
 Uniform exposure using "lo dose" system
 80 kVp, .25 mAs, 107", 1.3 mm focal spot
 Influx objective: 20X (NA 0.45)
 Efflux objective: 10X (NA 0.25)
 Number of data points: 512
 Distance between data points: 2.5 μm .

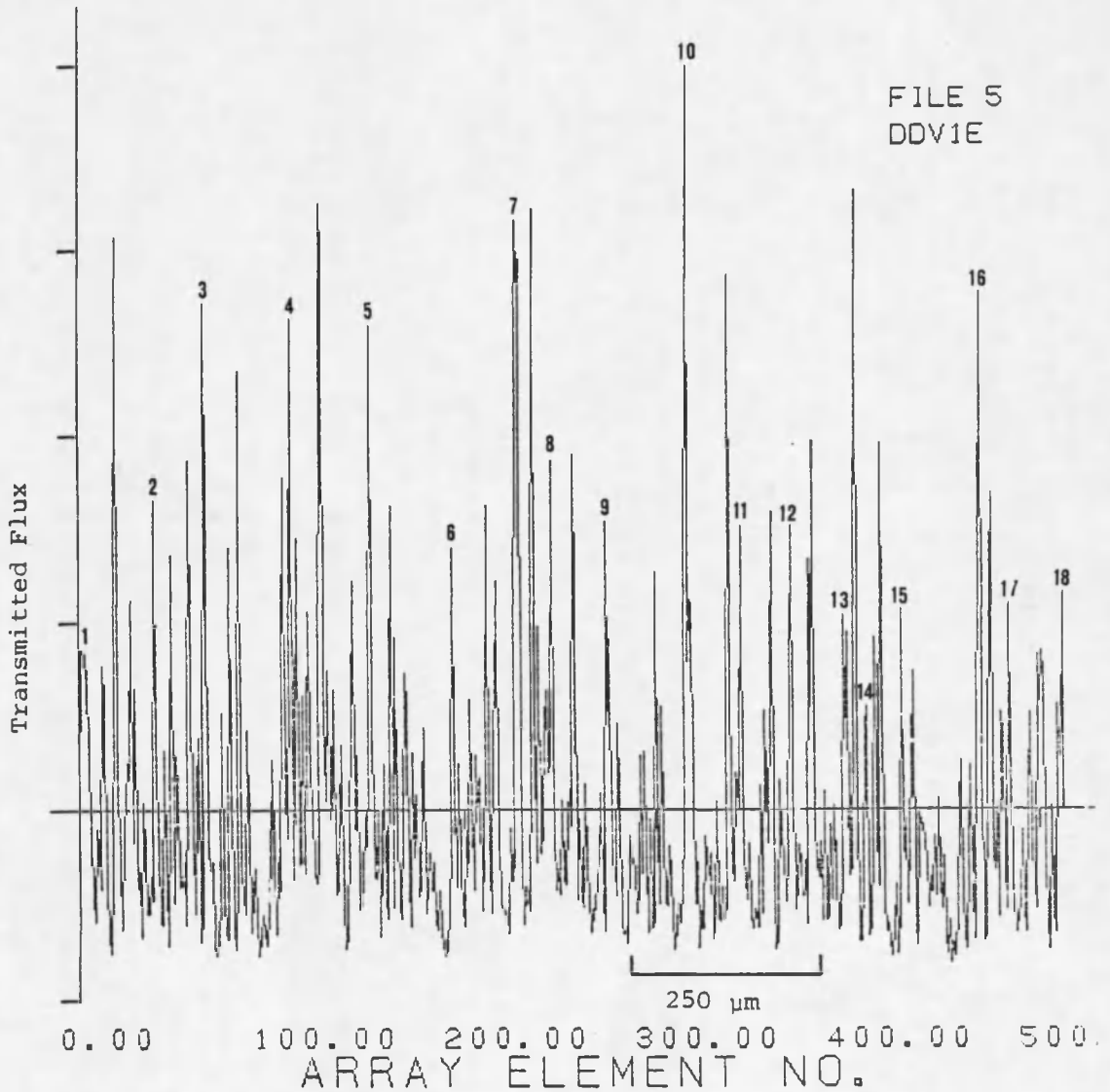


Figure 4.17. Results of an independent scan of the same area on the Dupont Cronex sample in the +x direction as shown in Figure 4.15. No adjustment was made to the apparatus between the scans which acquired the data presented here and in Figure 4.16.

Scan object: Dupont Cronex x-ray film
 Uniform exposure using "lo dose" system
 80 kVp, .25 mAs, 107", 1.3 mm focal spot
 Influx objective: 20X (NA 0.45)
 Efflux objective: 10X (NA 0.25)
 Number of data points: 512
 Distance between data points: 2.5 μm .

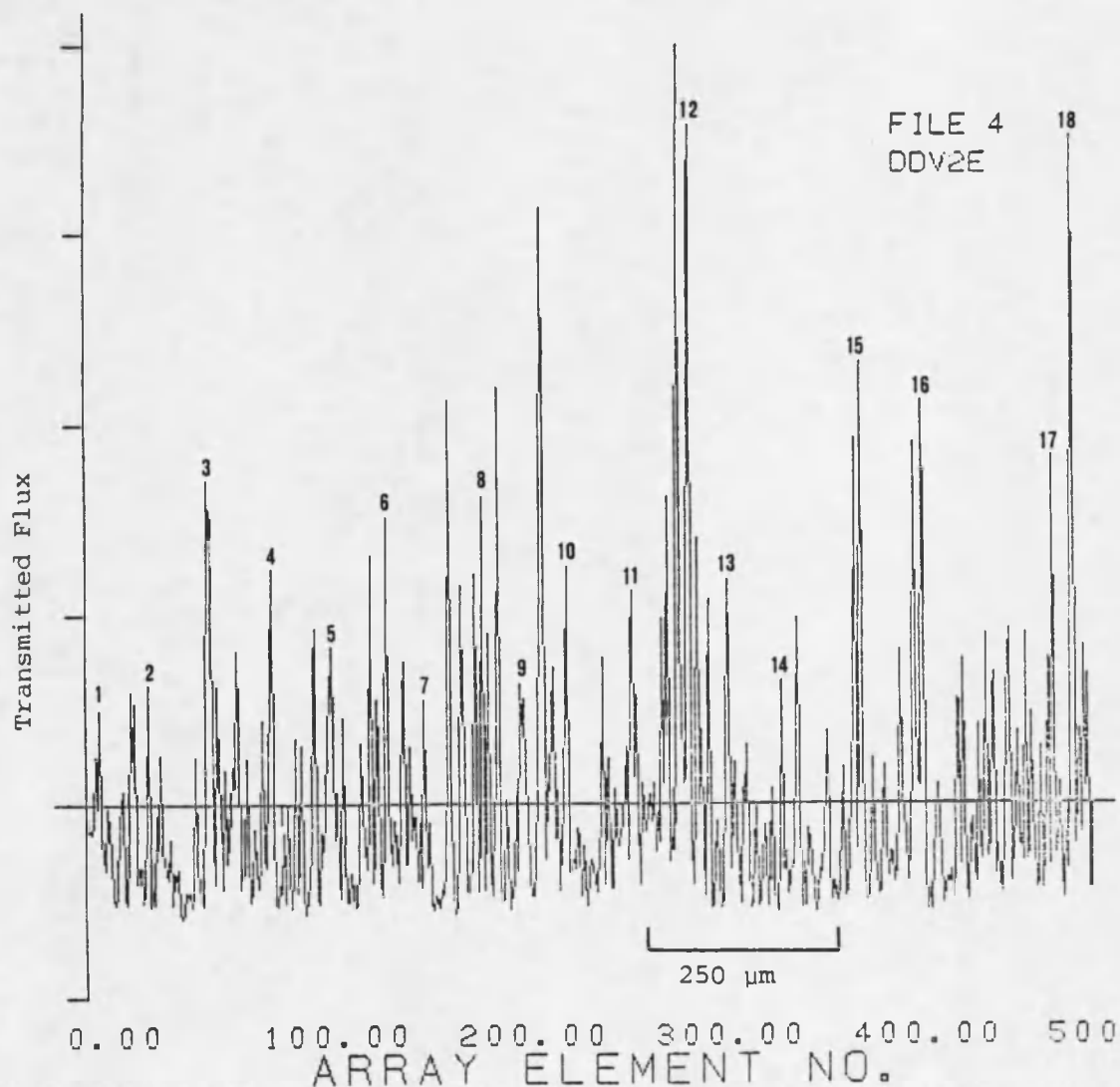


Figure 4.18. Results of scanning a sample of Dupont Cronex x-ray film in the -x direction of the scan pattern shown in Figure 4.15. This data is from the same data set as that presented in Figure 4.16.

Scan object: Dupont Cronex x-ray film
 Uniform exposure using "lo dose" system
 80 kVp, .25 mAs, 107", 1.3 mm focal spot
 Influx objective: 20X (NA 0.45)
 Efflux objective: 10X (NA 0.25)
 Number of data points: 512
 Distance between data points: 2.5 μ m.

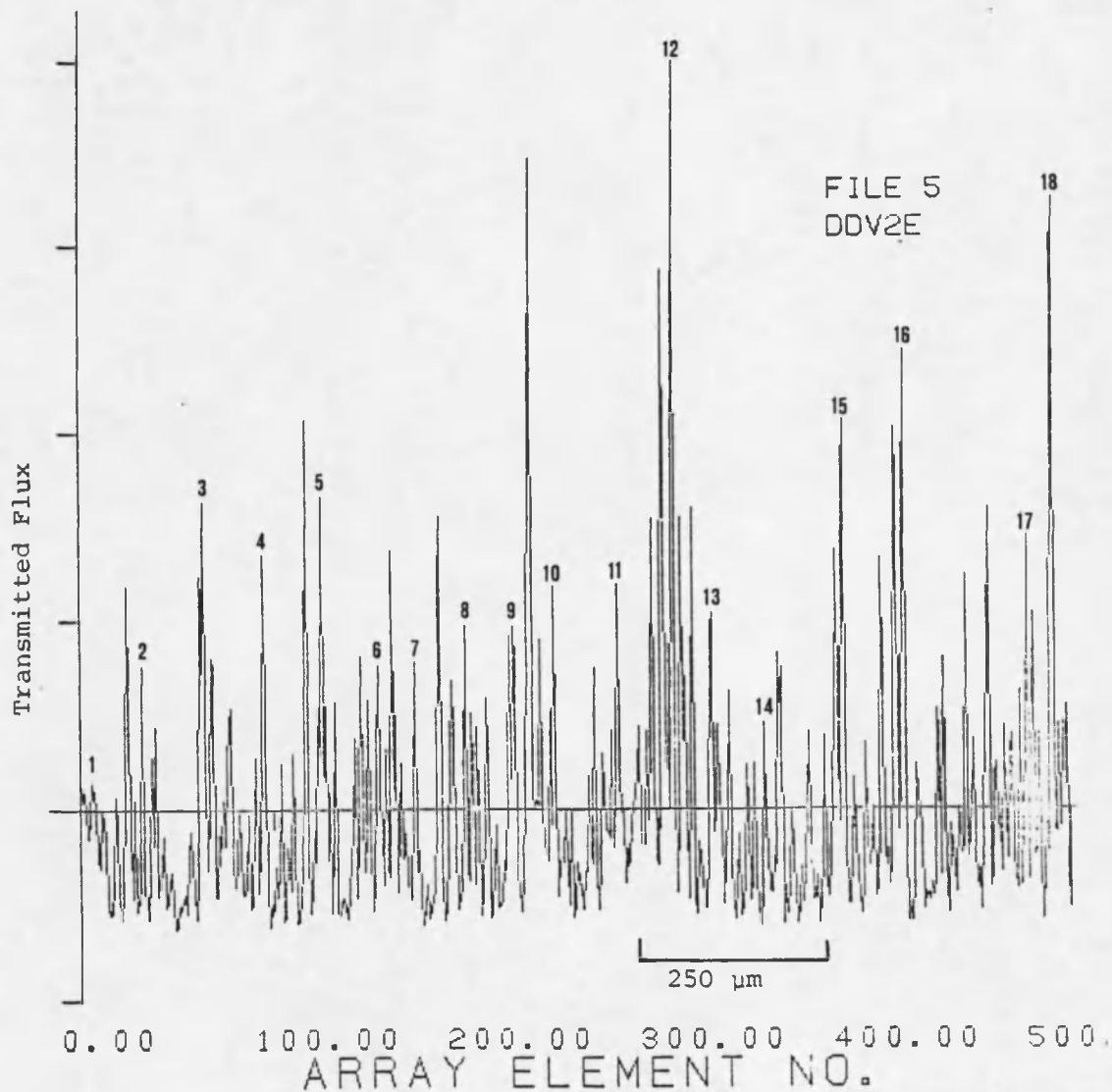


Figure 4.19. Results of an independent scan of the same area on the Dupont Cronex sample in the -x direction as shown in Figure 4.15. No adjustment was made to the apparatus between the scans which acquired the data presented here and in Figure 4.18.

Scan object: Dupont Cronex x-ray film
 Uniform exposure using "lo dose" system
 80 kVp, .25 mAs, 107", 1.3 mm focal spot
 Influx objective: 20X (NA 0.45)
 Efflux objective: 10X (NA 0.25)
 Number of data points: 512
 Distance between data points: 2.5 μm .

the slightest difference in the y position as the x scan is being made. The grain pattern is random; thus a slight y displacement means that on a scan in the x direction the edge of some grain might be encountered that had not been encountered by the light probe at the corresponding position in the previous scan, yielding a lower peak. Similarly, a grain on the other side of the scan path might not be encountered or less of it may block the area of the light probe, yielding a higher peak. In any event, for the system to be useful, some measure of repeatability is necessary. Figures 4.16 and 4.17 together with Figures 4.18 and 4.19 demonstrate that the overall character of the data remains the same and corresponding peaks are identifiable if not identical.

To determine whether the difference could be attributed indisputably to some "play" or imprecision in the stage drive mechanism in the direction opposite to the direction of the long scan, a scan tape was made which recorded 512 data points in the +x direction and 512 data points in the -x direction five times each. Figures 4.20 and 4.21 show two of the scans in the -x direction in principle over the same 512 data points. Much closer amplitude agreement was achieved in this case where there was no scan motion in the y direction. The result does suggest that the scanning stage precision is on the order of some fraction of the grain clumping size and thus that we can use this system to obtain meaningful results in scanning negatives of this type.

The results of the five scans in the +x direction were averaged and the average was plotted in Figure 4.22. Similarly, the five scans in the -x direction were averaged and the average was plotted in

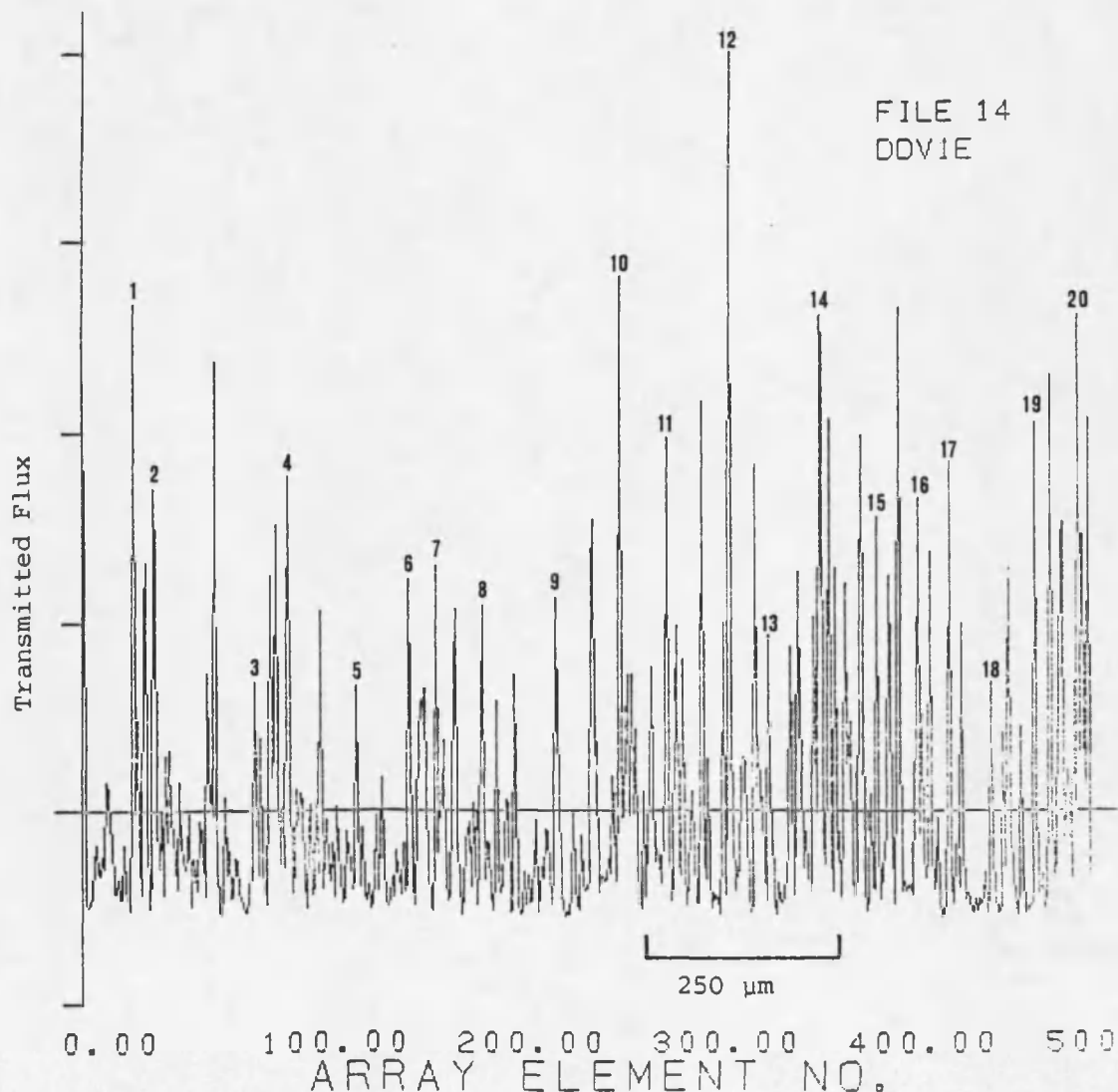


Figure 4.20. Results of the first scan of a sample of Dupont Cronex film in the +x scan direction. The scan pattern consisted of 5 scans in the +x and -x directions each of 512 points with no scan motion in the y direction.

Scan object: Dupont Cronex x-ray film
 Uniform exposure using "lo dose" system
 80 kVp, .25 mAs, 107", 1.3 mm focal spot

Influx objective: 20X (NA 0.45)

Efflux objective: 10X (NA 0.25)

Number of data points: 512

Distance between data points: 2.5 μ m.

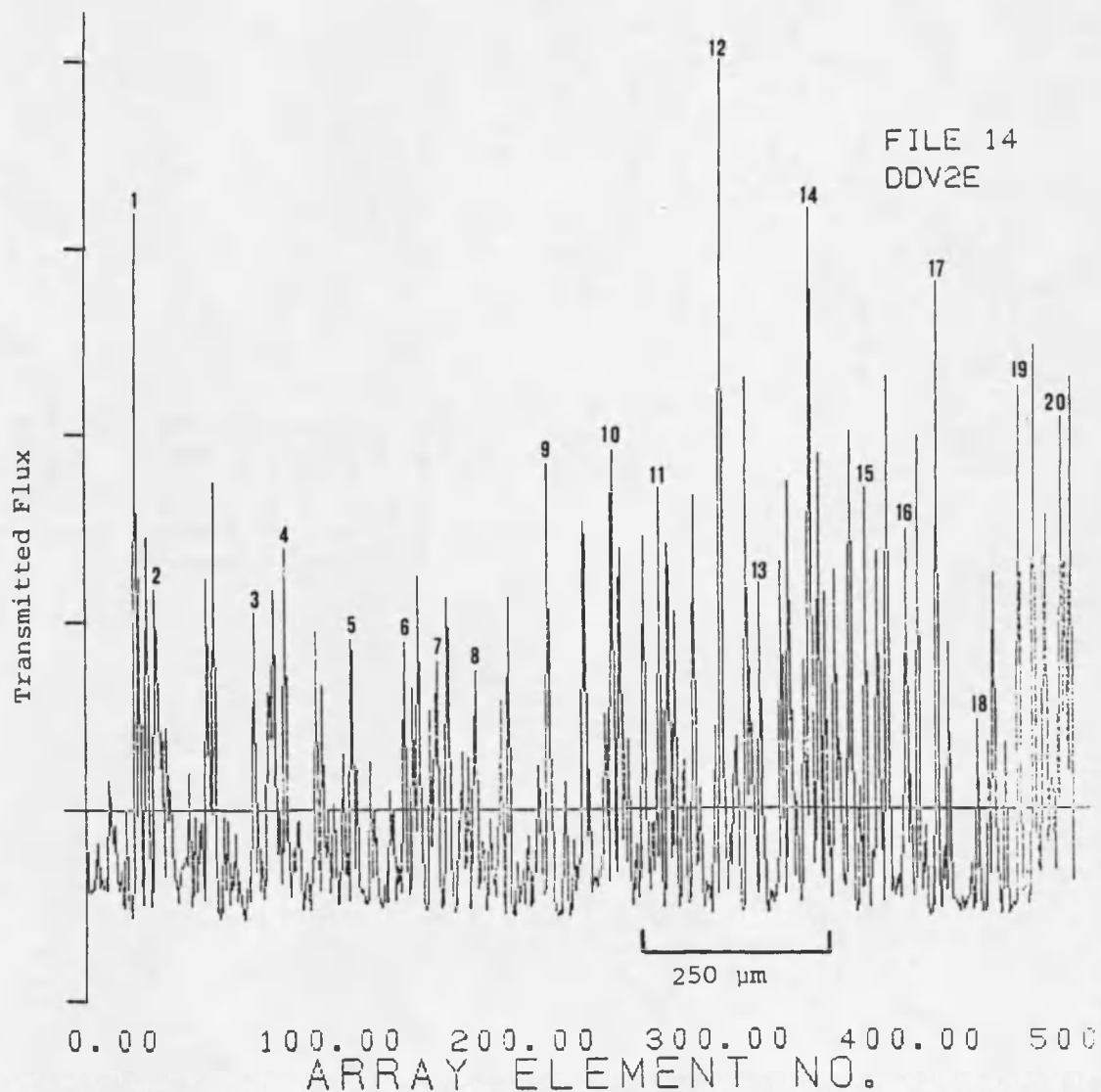


Figure 4.21. Results of the second scan of the sample of Dupont Cronex film in the +x direction. This data is from an independent scan in the same data set as that plotted in Figure 4.20.

Scan object: Dupont Cronex x-ray film
 Uniform exposure using "lo dose" system
 80 kVp, .25 mAs, 107", 1.3 mm focal spot
 Influx objective: 20X (NA 0.45)
 Efflux objective: 10X (NA 0.25)
 Number of data points: 512
 Distance between data points: 2.5 μm .

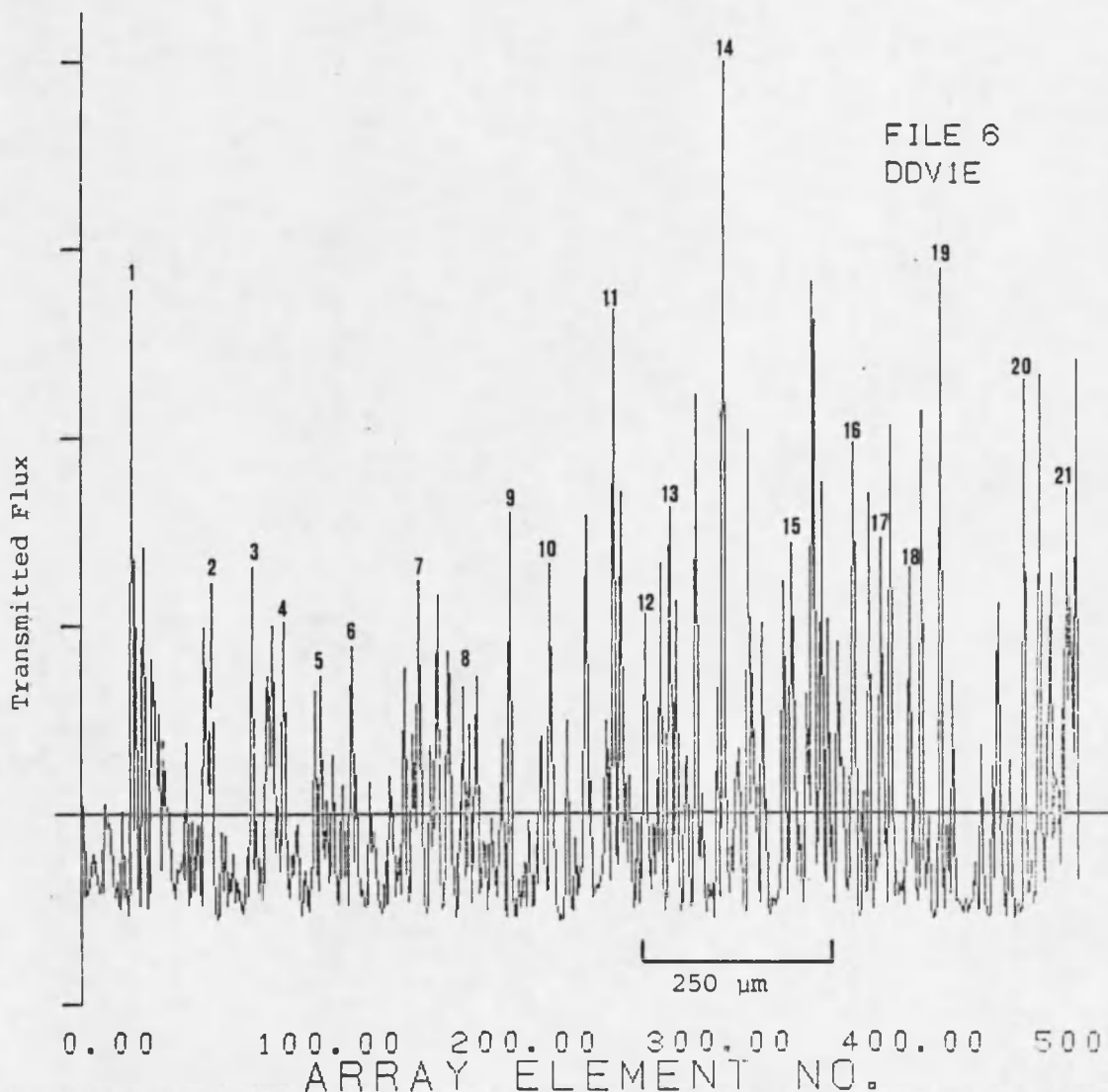


Figure 4.22. Results of averaging the 5 scans in the +x direction from the data set created by the scan pattern that consisted of 5 scans in the +x and -x directions each of 512 points with no scan motion in the y direction.

Scan object: Dupont Cronex x-ray film
 Uniform exposure using "lo dose" system
 80 kVp, .25 mAs, 107", 1.3 mm focal spot

Influx objective: 20X (NA 0.45)

Efflux objective: 10X (NA 0.25)

Number of data points: 512

Distance between data points: 2.5 μm .

Figure 4.23. We expect these figures to be symmetric reflections of one another. Corresponding peaks are numbered to aid in comparing the two figures.

The measured transmission data in Figures 4.22 and 4.23 was used as input to a program that calculates the power spectrum of the random grain distribution (Wiener spectrum). The measured data is windowed by the elevated cosine window of Figure 4.24 to remove the discontinuities at the beginning and end of the data sample.

The cosine window is applied to the data points within 10% of the endpoints. To reduce aliasing, the data is smoothed by averaging adjacent data points together. The power at each spatial frequency component is obtained by squaring the real and imaginary components of the array returned by the fast Fourier transform subroutine. The power curve is normalized so that the area under it is 1.0 in order to aid in comparison of one curve to another. The resulting power curve is then "Hanned" using weights 0.25, 0.50, 0.25 to obtain the results plotted in Figures 4.25 and 4.26. Although similar, the two curves are not identical. The differences in the two curves reflect the amount of imprecision in the measurement process and the roundoff error in the calculations. Figures 4.27 and 4.28 show plots of the same Wiener spectrum calculation sequence applied to a similar but completely independent set of data from the same x-ray film sample. The plots have similar characteristics but clearly will not overlay one another identically. The qualities that we observe in these plots is what we would expect. Similar characteristics among plots leads us to conclude

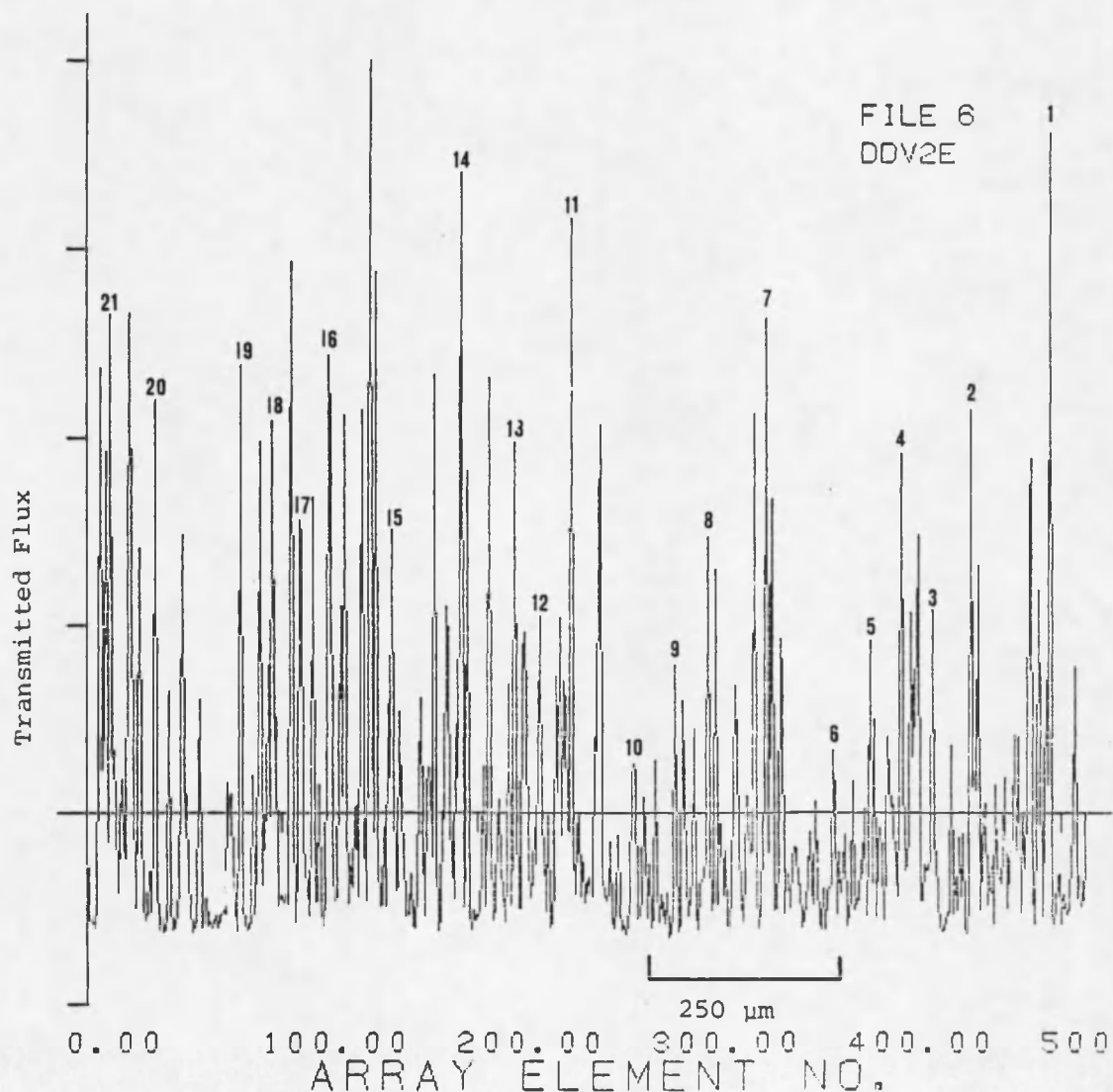


Figure 4.23. Results of averaging the 5 scans in the $-x$ direction from the data set created by the scan pattern that consisted of 5 scans in the $+x$ and $-x$ directions each of 512 points with no scan motion in the y direction.

Scan object: Dupont Cronex x-ray film
 Uniform exposure using "lo dose" system
 80 kVp, .25 mAs, 107", 1.3 mm focal spot
 Influx objective: 20X (NA 0.45)
 Efflux objective: 10X (NA 0.25)
 Number of data points: 512
 Distance between data points: 2.5 μm .

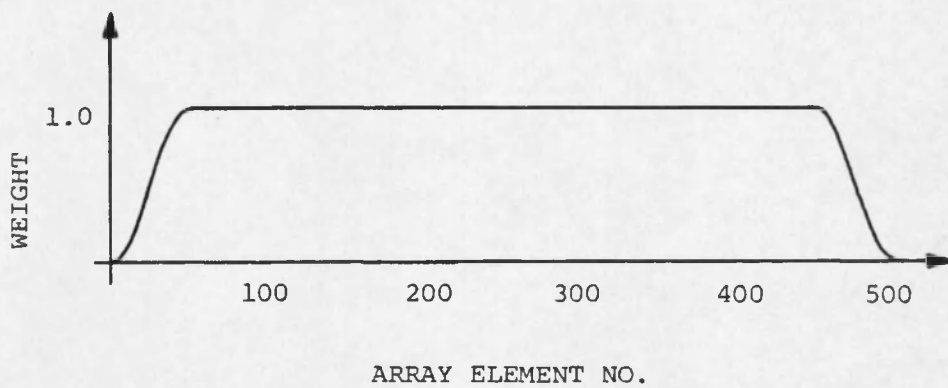


Figure 4.24. Elevated cosine window applied to the data.

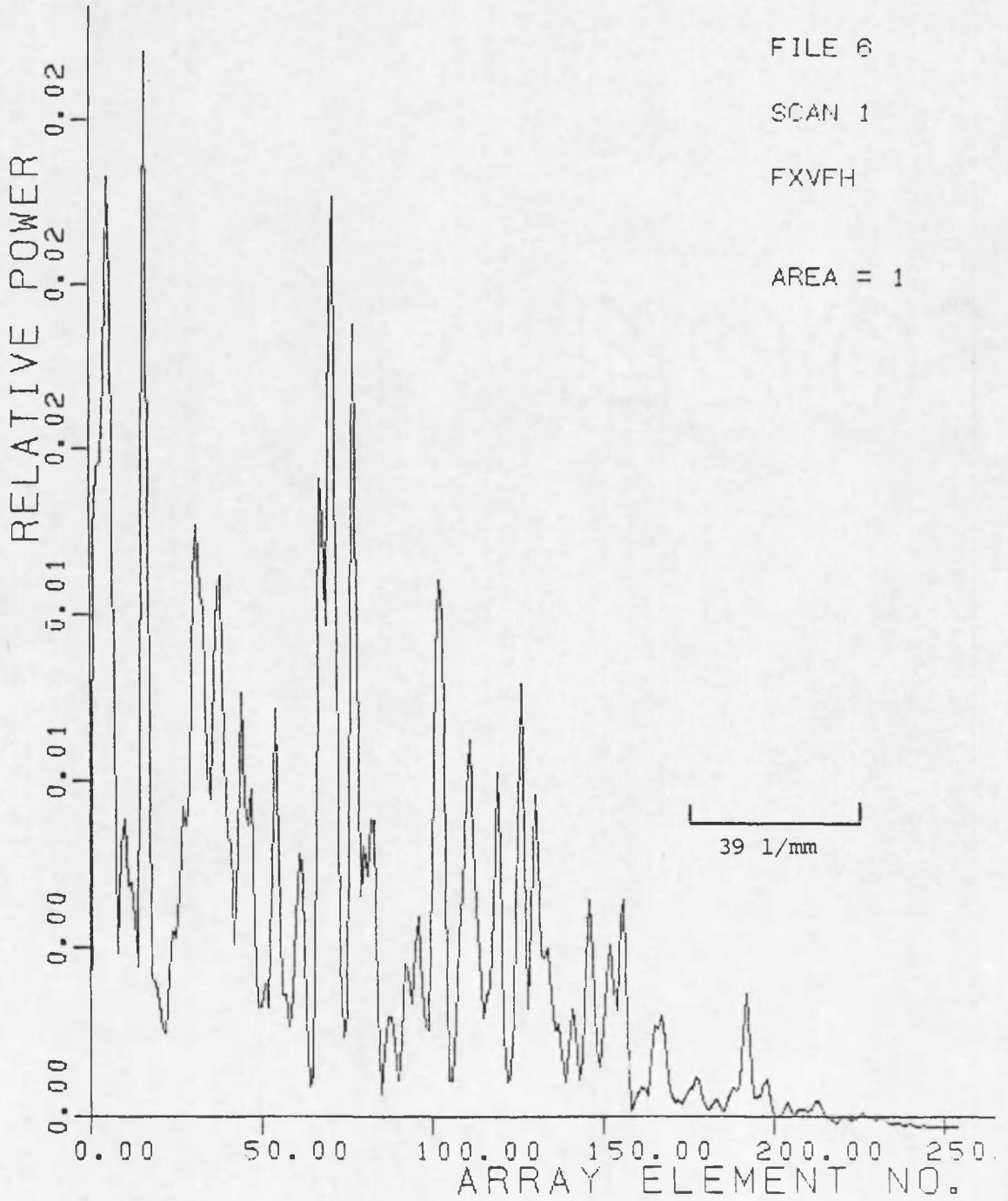


Figure 4.25. Wiener spectrum of the data shown in Figure 4.22.

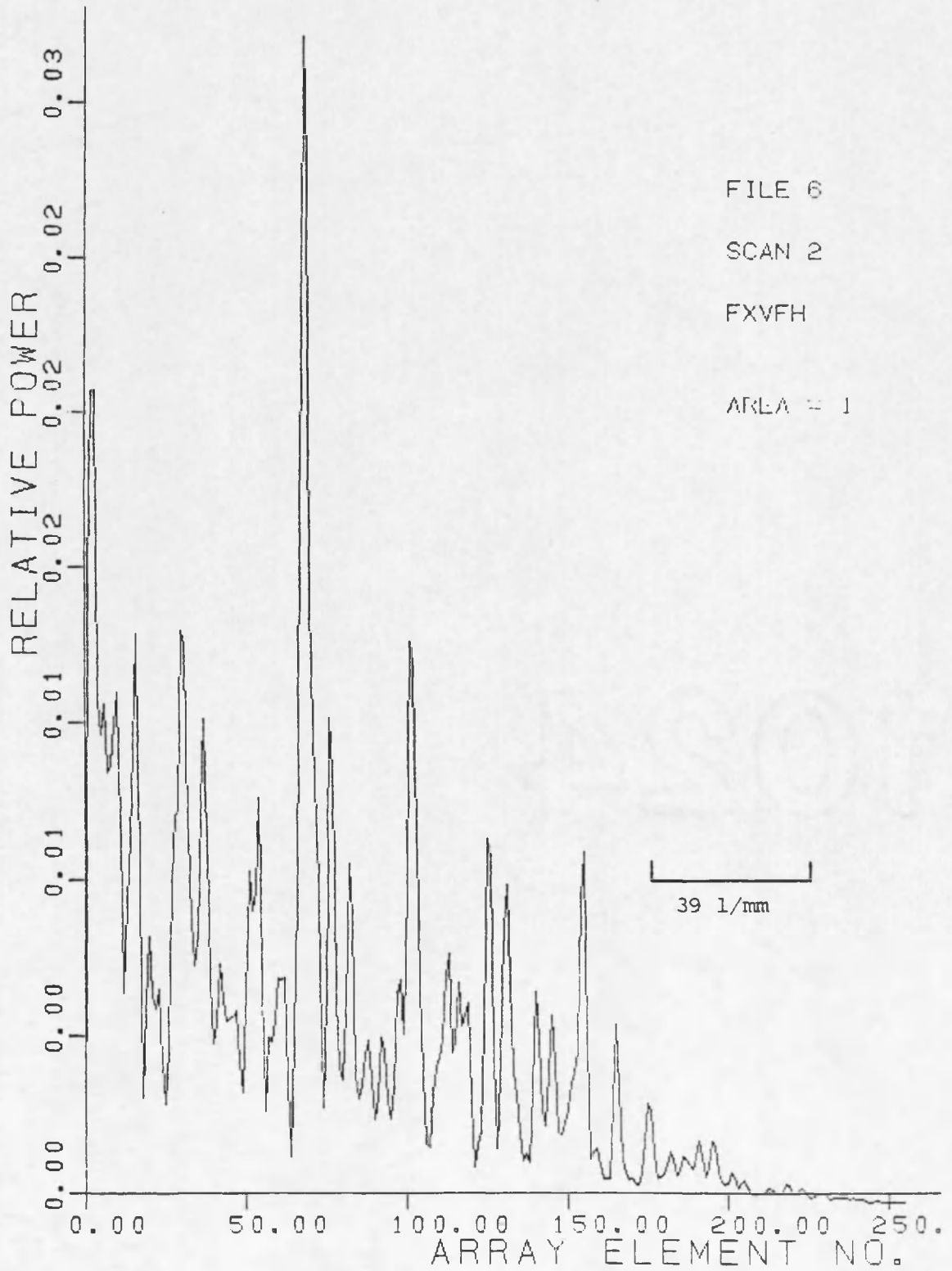


Figure 4.26. Wiener spectrum of the data shown in Figure 4.23.

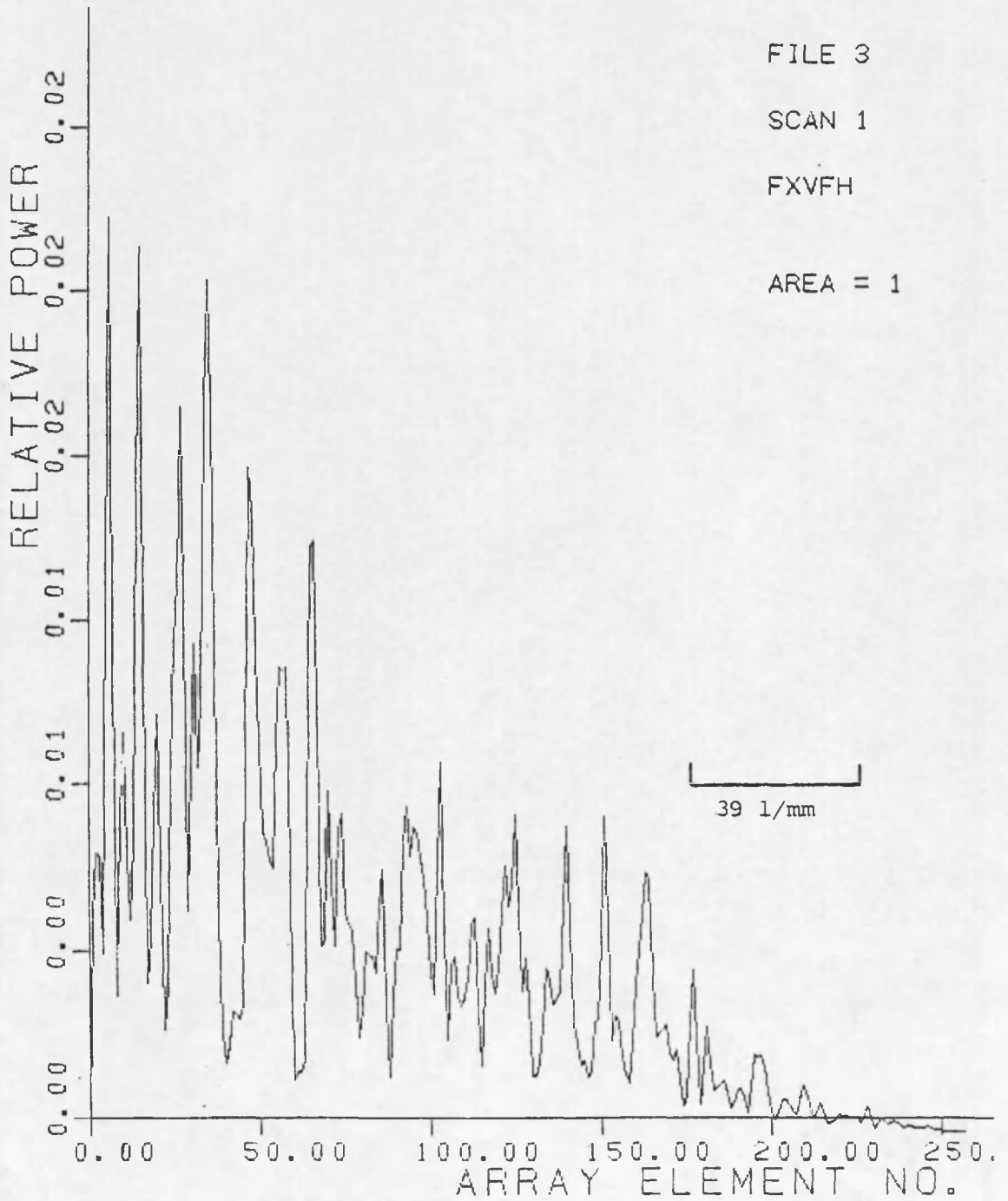


Figure 4.27. Wiener spectrum of data obtained from the same sample of x-ray film as those shown in Figures 4.22 and 4.23 but independent of those data.

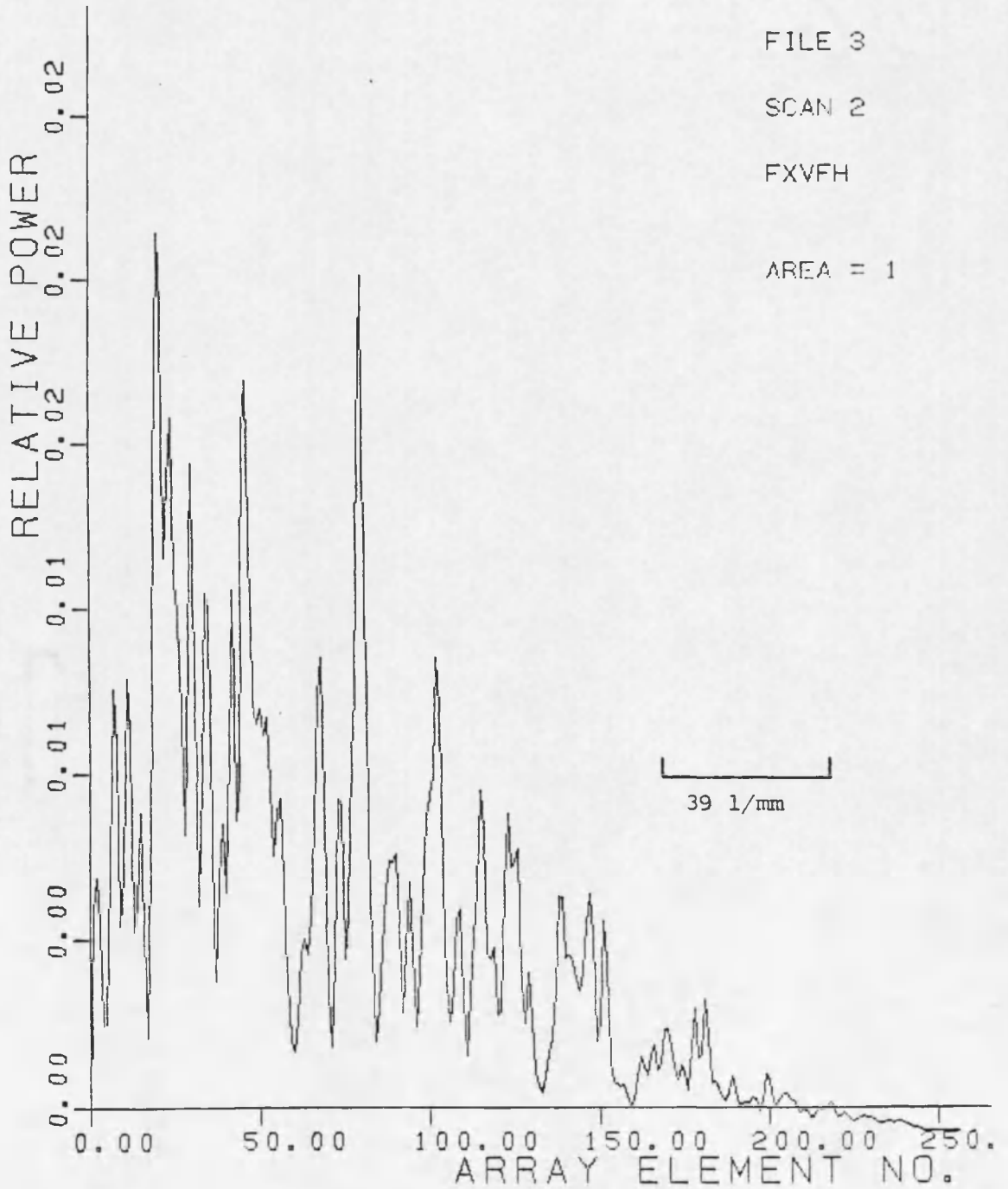


Figure 4.28. Wiener spectrum of another independent set of data obtained from the same sample of x-ray film as those shown in Figures 4.22 and 4.23.

that we are measuring the same qualities in the film sample from one data set to the next. Completely dissimilar plots would suggest that our measurements were not valid in some fundamental sense (that is, the apparatus is not capable of measuring the desired quality), or that the measurements were so imprecise or unrepeatable as to make the results meaningless. Completely identical plots would suggest that we were not seeing results due to the grains on the sample (a random process) but rather seeing some underlying artifact of the measurement process.

We shall assume that the grain noise that we are investigating is isotropic in character. To obtain a better estimate of the true noise spectrum we can average the spectra obtained from each of six sets of independent data. Figure 4.29 shows such an average. As expected, "the standard deviation of the spectral components is large being on the order of their mean throughout the spectrum" and "the estimate is not bad 'on the average'" (Wagner and Sandrick, 1979, p. 525).

In fact, the results obtained from averaging only two independently obtained power spectra yields a quite similar result. Such an average is plotted in Figures 4.30 and 4.31. The pronounced peak occurring at 3 lines/mm in Figures 4.29 and 4.31 is probably quantum mottle of the screen-film system. Wagner (1977) reports mottle in similar screen-film systems falling off by 4 lines/mm.

A density wedge was made on 35 mm Kodak 5063 safety film by contact printing a glass neutral density wedge on the film. The neutral density wedge was made by cutting a wedge shape from a block of neutral density glass. A wedge of similar shape cut from clear glass was

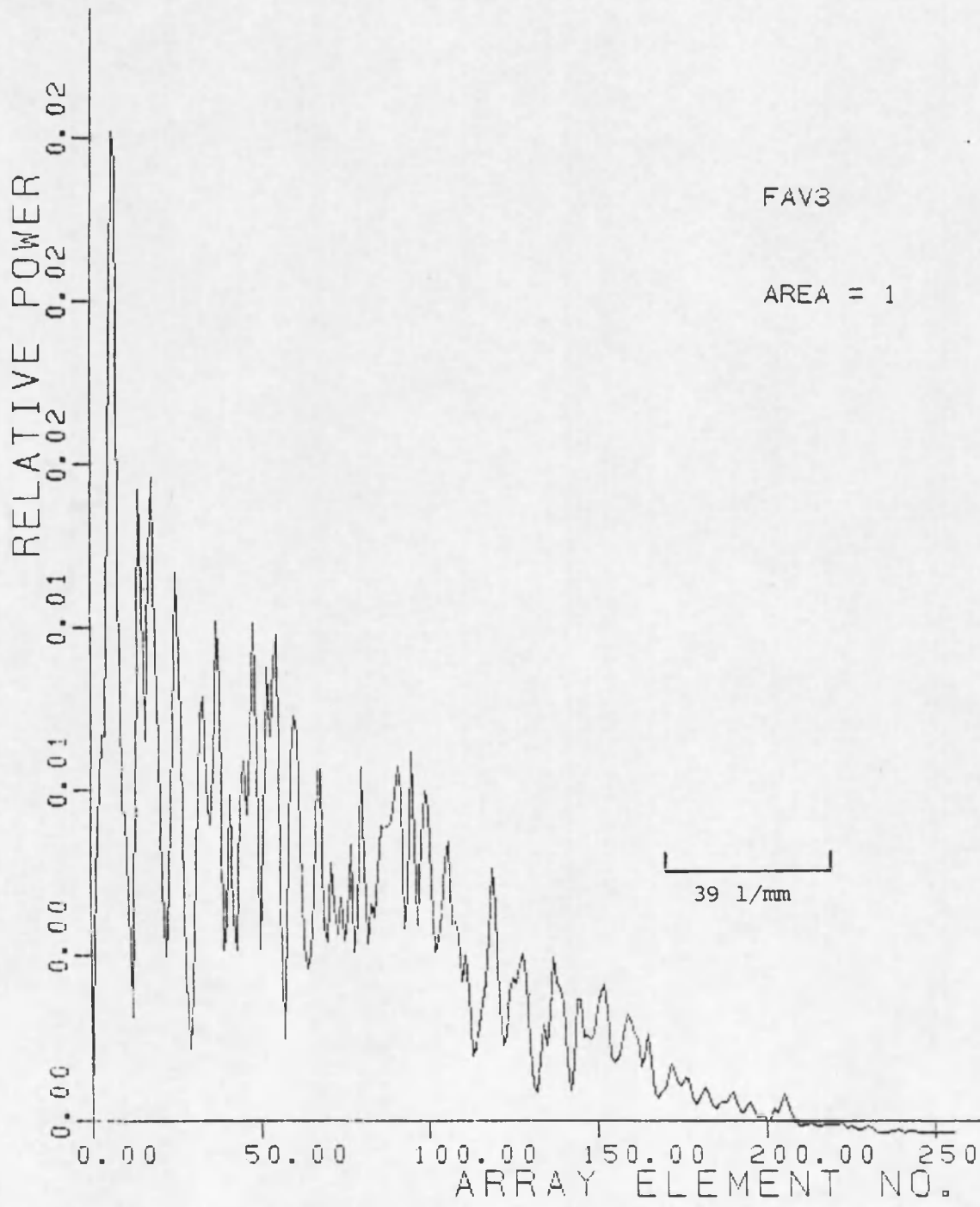


Figure 4.31. Average of a different two of the six independent Wiener spectra that were averaged to give Figure 4.29.

cemented to the neutral density glass wedge to remove any optical phase differences that would otherwise have been introduced by the difference in glass thickness along the wedge. Figure 4.32 shows the physical setup used to make the contact print. The glass neutral density wedge was obtained from Mr. David Thomas, Optical Sciences Center, University of Arizona.



Figure 4.32. Physical setup used to make a film density wedge.

The resulting neutral density wedge on film was scanned taking data points every 100 μm . The resulting plot of transmission versus position on the film is shown in Figure 4.33. The figure shows that

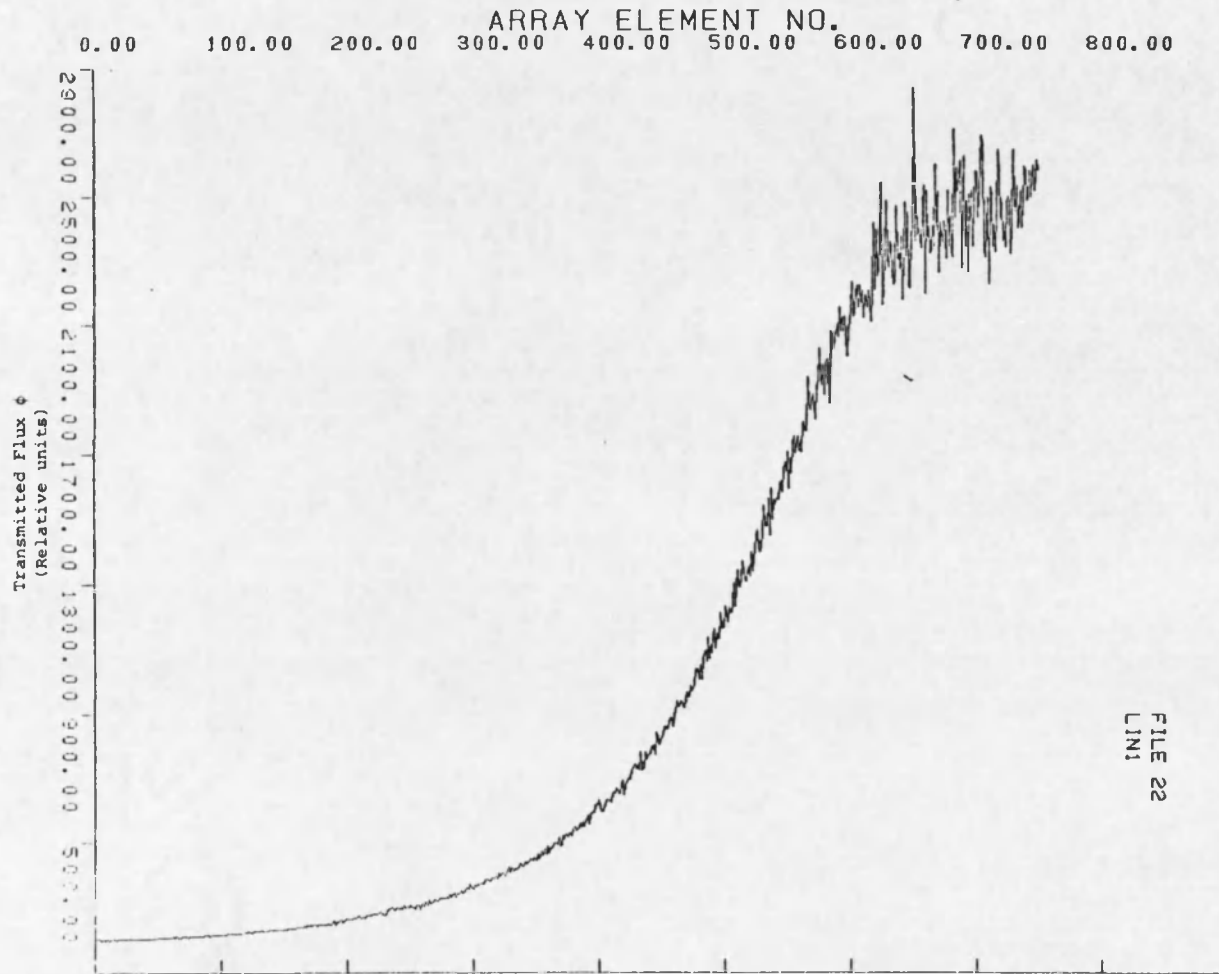


Figure 4.33. Results of scanning the film density wedge on Kodak 5063 film with the spot produced by the 10X microscope objective. The efflux objective was the 20X microscope objective.

the dynamic range of the film was exhausted since the curve smoothly approaches a line of zero slope at the low transmission end of the curve and a line of zero slope on the average at the high transmission end of the curve. The dynamic range of the microdensitometer itself has not been exhausted, as can be seen from fluctuations in the plot throughout the range of measurement and from the absence of any horizontal straight line portions in the plot which would indicate clipping.

The density of each end of the film density wedge was measured using a Macbeth densitometer Model TD402 (S/N 80120). The minimum density on the film density wedge measured 0.40 and the maximum density measured 2.16. Adjusting the maximum transmission value so that the average of the high transmission fluctuations corresponds to a density of 0.40 and scaling the rest of the data by the same factor yields the density curve shown in Figure 4.34. The Macbeth densitometer measures a maximum density of 2.16 while the result of the microdensitometer scan indicates a maximum density of 2.74. The difference is due to some scattered light being lost in the microdensitometer case, resulting in a measured density higher than the actual sample warrants. The scattering of light by the silver grains in a photographic negative was studied by Andre Callier in 1909. He used Q for the ratio of the specular density to the diffuse density of a negative, and it has thus become known as the Callier Q factor.

The density value obtained with the microdensitometer has a specular character that allows both absorption and scattering to contribute to the measured density. In the diffuse measurement the

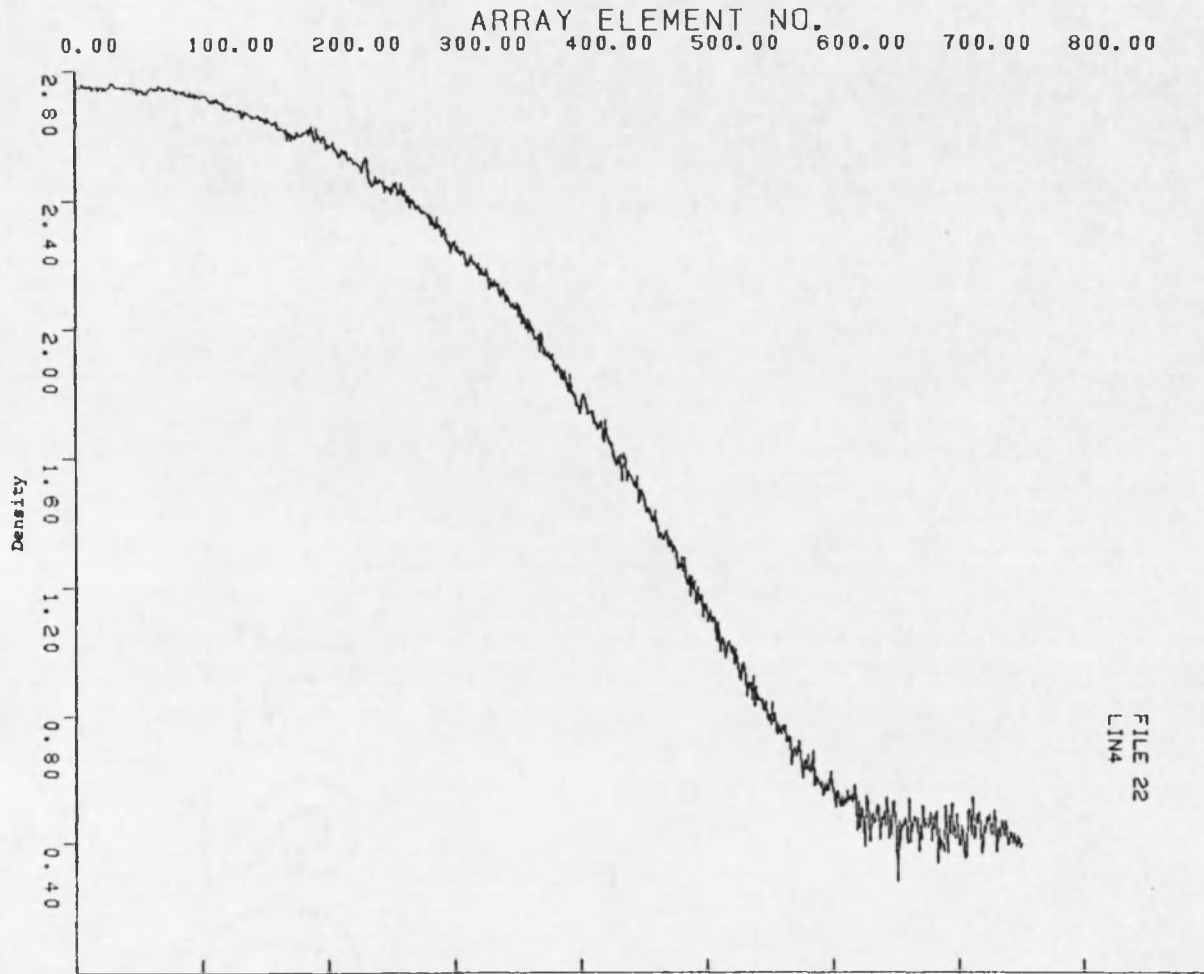


Figure 4.34. A plot of $D = -\ln(k\phi)$ versus position on the film for the data shown in Figure 4.33. The maximum transmission end of the data was scaled to give a $D_{\min} = 0.40$ in agreement with the value measured using the Macbeth densitometer. The remainder of the data was scaled by the same factor.

density is due to absorption only. The ratio of the density value obtained using the microdensitometer (2.74) to the density value measured on the Macbeth densitometer (2.16) is 1.27. That result is reasonable since the typical range of the Callier Q factor is 1.2 to 1.9.

CHAPTER 5

CONCLUSIONS

In the process of conducting the experiments that yielded the results and conclusions of Chapter 4, several conclusions of a general nature were arrived at.

Experimental Overhead

Considerable overhead in time and resources is involved in the experimental process. Digressions into topics not directly related to the principal question are not only unavoidable, they are necessary. As a first example, during the construction of equipment for this project, some time was spent learning machine shop techniques that had no direct connection with the primary optical considerations. Second, the design, construction, and troubleshooting of the electronics connected with the project took at least twice the amount of time initially estimated. The reason for the extensive troubleshooting and redesign of some circuits was the removal of errors of electronic origin, which would have invalidated the experimental results. This type of effort, although necessary, is not nearly as rewarding as efforts that lead to refinements in the precision or accuracy of the measurement. Finally, computer hardware maintenance and software debugging time proved to be an unexpected burden. The author made three hardware repairs, and

others using the computer also made several significant repairs or upgrades to the machine during the lifespan of the project. A plot subroutine provided by the computer manufacturer had several unclear aspects and was poorly documented. Considerable time was lost in gaining an understanding of the program by studying the source code line by line.

Hardware and Software Documentation

Documentation for software or hardware is absolutely essential. The software plot routine that was used required much extra time to understand due to the lack of an adequate explanation of its operation. Similarly, the causes of a problem evident on the Zeiss scanning stage was long undiscovered due to the lack of documentation. The stage seemed to lose several stepping pulses whenever the direction of stepping was reversed. The problem was a lower-than-adequate supply voltage present at the servo motor driving circuits. The voltage was not at its proper level because the dual voltage jumper on the power transformer primary was configured for 220 V (European) operation, but the system was being used on a 117 V circuit. The source of the error was not discovered or even suspected until Zeiss provided German schematics and documentation.

Human Factors

In the initial electronic circuit design a very compact and elegant format was devised for packing information into 8-bit data bytes. Although this format allowed some information to be exchanged at the

maximum data rate from the standpoint of the computer terminal, it added unnecessary complication from the standpoint of the human operator. In retrospect, a different design would have been just as easy to construct and much less obscure to understand. The less compact data format would have added to the data transfer time by as much as 50%, but that additional time would have been offset by ease of operation.

Legacy

Because the amount of experimental overhead is usually high, all aspects of the research project must be conducted with an eye toward being of possible use in the future.

Equipment or circuitry designed for a specific task may not be suitable for some requirement in the future. Furthermore, the task at hand might be unduly compromised by attempting to make a circuit so general that it will have future use. By contrast, the choice of a standard, well known technology is likely to have future payoffs in terms of time and effort required for a new application. For example, this project used TTL digital integrated circuits in the scan control and data recording electronics. Although the state-of-the-art has moved from medium scale integration in TTL integrated circuits to very large scale integration in microprocessors, obsoleting the current circuitry itself, much of the understanding and many of the techniques learned carry over directly.

Documentation is paramount to understanding a system. When a concept has been grasped, it will save significant time if the basics of the idea and of the thought process used to approach the idea are documented succinctly and completely for future reference within the project. Documentation in longhand with freehand sketches is sufficient for this purpose. The need for this type of documentation applies equally to mathematical or physical concepts, mechanical alignment procedures, electronic circuitry operation, or computer software function.

APPENDIX A

MICRODENSITOMETER PHYSICAL CONSTRUCTION

This appendix describes aspects of the physical construction of the microdensitometer. Figure A.1 shows a scale drawing of the component layout in the apparatus.

The various components were mounted on a 1/2-inch-thick aluminum back plate. The back plate is bolted to five cinder blocks that are epoxied to one another. This total mass becomes a vibration-damping mechanism. The back plate was drilled and tapped for 10-32 screws. Mounting blocks were drilled and reamed to allow standard optional bench mounting rods to be secured to the mounting blocks and the mounting blocks to be secured to the back plate in a solid yet easily changeable way.

Translation mounts and an inverted-V optical bench used in a previous vertical mockup were not satisfactory. The many degrees of freedom in that system allowed the whole optical setup to sag and become misaligned.

A suitable description of the current mount would be "solid tinkertoys." The system is easily reconfigured, yet while a configuration is being used it is solid.

A Spectra Physics Model 236 He-Ne laser is used as a source of coherent light at 6328 Å. Light from the laser is polarized. A polaroid sheet is inserted in the light path ahead of the spatial

Figure A.1. Microdensitometer component layout.

- | | |
|-----------------------------|--|
| A. Laser | H. Servo motors, 0.5 $\mu\text{m}/\text{step}$ |
| B. Front surface mirror | I. Efflux objective |
| C. Spatial filter | J. Upper microscope carrier |
| D. Lower microscope carrier | K. Eyepiece tube |
| E. Extension tube | L. Photodiode, S-100A |
| F. Influx objective | M. Sensor focusing mount |
| G. Zeiss scanning stage | N. Amplifier, buffer |

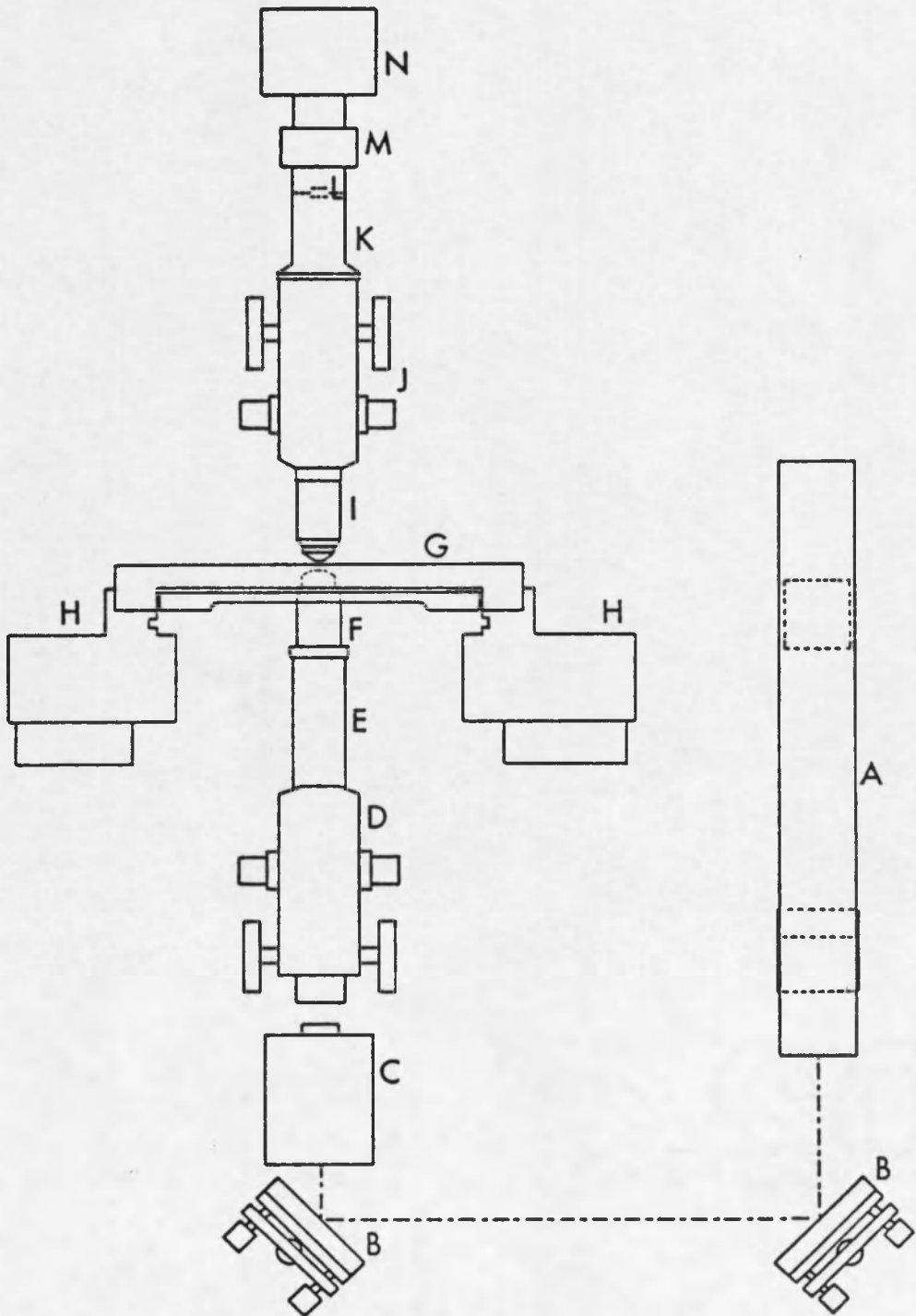


Figure A.1. Microdensitometer component layout.

filter, to attenuate light from the source when a high transmission of the sample would otherwise allow the detector-instrumentation amplifier combination to saturate.

The need to mount the Zeiss scanning stage in a horizontal orientation was the only design constraint of note. The Zeiss stage is capable of moving in 0.5 μm steps in both x and y direction. The horizontal orientation of the stage allows the gravity vector to be normal to both scanning motions. In this case neither scanning servo motor is forced to act against gravity.

The space immediately beneath the Zeiss stage is cluttered with struts, servo motor housings, and various pivots and adjustment screws to allow the scanning stage to be leveled. The microscope carrier is the most convenient and practical mount, and we did not want to replace it with some other specialized, nonstandard, one-of-a-kind mount. However, cantilevering a mount for the carrier out from the back plate and up under the stage was not satisfactory. The long moment arm of the cantilever tended to sag causing the optics to become misaligned. In addition its susceptibility to vibration was a large enough drawback to offset any advantage to be gained from keeping the standard microscope carrier. A simple solution allowed us to avoid the cantilever while keeping the standard microscope carrier.

In the apparatus described here the carrier under the stage was inverted and the eyepiece tube removed. An extension tube was made that has interior threads at one end to match the threads of an objective and exterior threads at the other end to match the threads

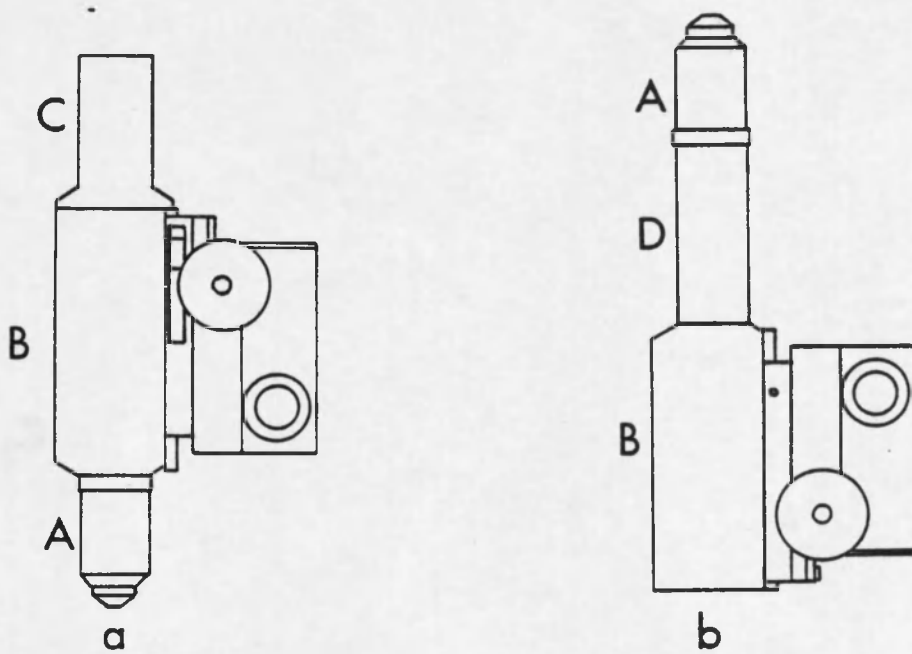
in the carrier (see Figure A.2). The extension tube was screwed into the carrier and the objective was screwed into the other end of the extension tube. The carrier itself could then be mounted firmly to the back plate well below the obstructions under the stage, but the extension tube allowed the influx objective to easily come within its working distance of the sample being scanned.

The spatial filter was mounted as close as practicable under the carrier. Thus the typical working conjugates are approximately maintained.

The interior of the extension tube was spray painted flat black in an attempt to reduce flare light that might be caused by glancing reflection from the aluminum side walls of the tube. We noted that at glancing incidence even "flat" paint is reflective.

Richard Sumner of the Optical Sciences Center suggested the best solution in the form of a sheet of "politex"[™] polishing lap. Even at glancing angle the politex is flat black. The material is spongy, thus easily bent, and the back of the material is pregummed, all desirable characteristics.

A correctly sized rhomboid was cut from a sheet of the material and rolled to fit inside the extension tube. In this way the seam where the two edges of the material met spiraled up the tube, thus reducing any one-sided anomaly that the seam might otherwise have caused (see Fig. A.3).



(a) Typical configuration

(b) Actual configuration, carrier inverted with objective extension tube and no eyepiece tube.

Figure A.2. Influx optics mount.

- A. Microscope objective
- B. Microscope carrier
- C. Eyepiece tube
- D. Extension tube

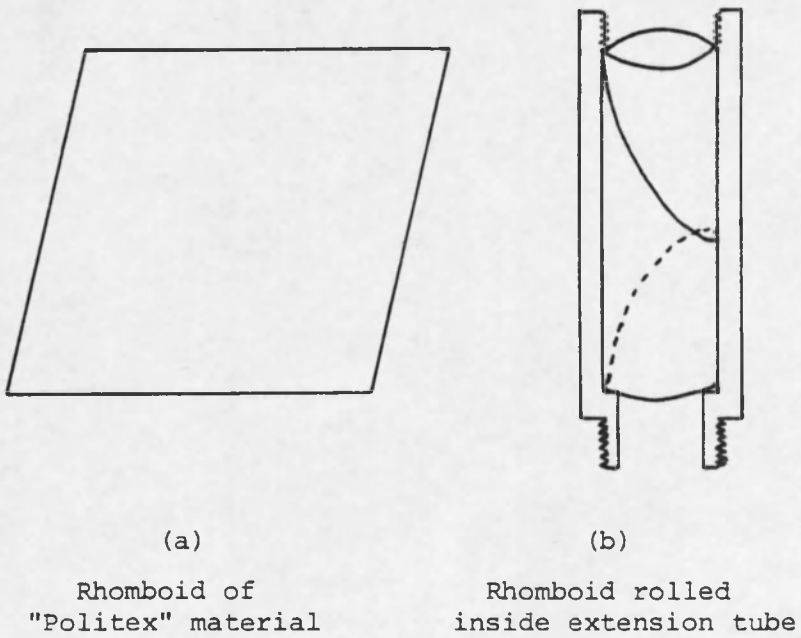


Figure A.3. Extension tube lining to reduce flare.

- (a) Rhomboid of "politex"
- (b) Location of politex in extension tube

APPENDIX B

SYSTEM CIRCUITRY

The electronic circuitry associated with the microdensitometer falls naturally into two categories based on function: the Zeiss scanning stage control circuitry, and the digitizing and data recording circuitry. The author constructed the scan control and digital recording circuitry using LSI and MSI TTL circuits.

Scanning Stage Control Circuitry

Before a photographic sample can be scanned, it must be mounted on the Zeiss scanning stage and the optics must be manually adjusted. The sample is then positioned so that the physical location being probed is the first data point desired. The operator must then input to the stage control circuitry: (1) the desired number of steps between the data points, (2) the scanning direction (x or y), and (3) the location of the final data point in the current scan line. The physical distance between data points must be integer multiples of $0.5 \mu\text{m}$, up to a maximum of 255 half-micrometer steps or $127.5 \mu\text{m}$. The maximum travel per scan line is 65,535 half-micrometer steps or $32,767.5 \mu\text{m}$. The physical limit of the Zeiss travel is 75 mm.

Parameters are input to the stage control circuitry by means of the keyboard of the Texas Instrument Model 733 Data Terminal or through playback of a prerecorded digital cassette tape in the data terminal's "playback" cassette drive.

The format of the parameter input sequence is shown in Figure B.1.

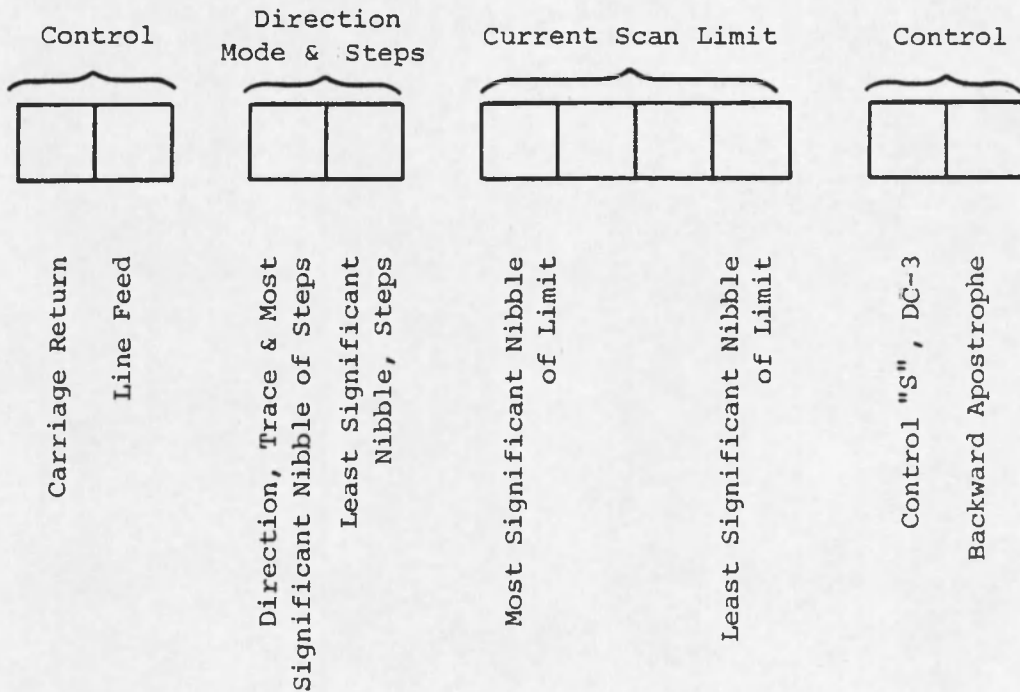


Figure B.1. Parameter Input Format

The function of the first two control characters is to aid in the readability of recorded data. The carriage return and line feed cause the input parameters of a new scan to appear on a new line in the recorded data.

The direction and number of $0.5 \mu\text{m}$ steps between data points are contained in the third and fourth characters. The ASCII characters sent to the stage control circuitry are made up of 7 binary bits each. Figure B.2. shows the characters in detail.

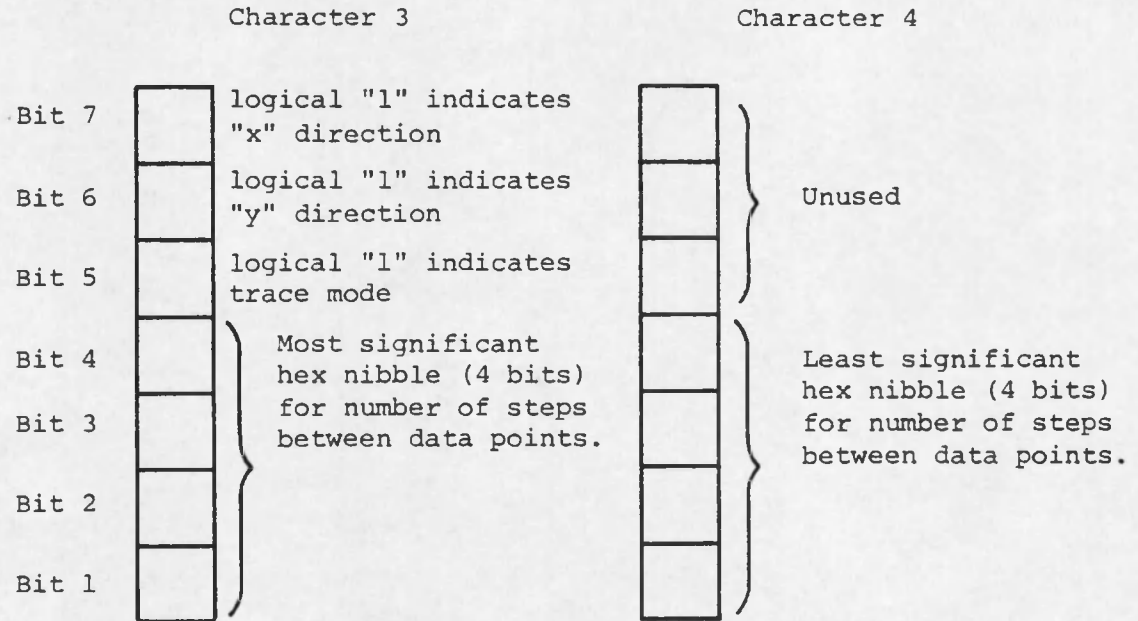


Figure B.2. Bit definitions of character 3 and 4.

Eight binary bits are required to denote the number of steps between data points in the allowable range 0 to 255. Of these eight bits the four of higher order are bits 1 through 4 of the third character. The low order four bits are bits 1 through 4 of character 4.

As shown in Figure B.2., bits 5, 6, and 7 of character 3 also have meaning. When bit 7 is logical "1" the control circuitry interprets this to mean scan in the x direction. When bit 6 is logical "1" the character is interpreted as a command to scan in the y direction. When bit 5 of character 3 is logical "1" the "trace" mode is active. Further description of the trace mode is deferred until the second section of this appendix.

Characters 5, 6, 7 and 8 in the parameter input format load a binary value into registers of the stage control circuitry which set a limit to the number of steps that may be taken in the current scan direction. The maximum allowable number of steps is 65,535, which requires 16 bits of binary storage. The 16 bits are loaded in order of most significant hex digit (4 bits) to least significant hex digit by the low order four bits of characters 5, 6, 7 and 8. Bits 5, 6, and 7 of characters 5, 6, 7 and 8 are ignored.

Character 9 is always control-S (device control 3), which is interpreted by the TI-733 as a command to turn off the cassette, which is in playback mode. The cassette always sends one character following the control-S. In this case it is a backward apostrophe, which is received by the stage control circuitry and ignored although it is seen upon visual inspection. Seeing the backward apostrophe confirms for the operator that control-S has been sent.

Figure B.3 shows the ASCII character set, annotated to highlight the modes and features of programming the control circuitry described in this section.

Figure B.4 shows an example of a scan coding worksheet annotated to highlight the method used in determining the appropriate ASCII characters to be sent in order to cause the desired scanning motion to occur.

b_7	b_6	b_5	b_4	b_3	b_2	b_1	b_0	b_7	b_6	b_5	b_4	b_3	b_2	b_1	b_0
0	0	0	0	0	0	0	0	1	1	1	1	1	1	1	1
0	0	0	0	0	0	0	1	0	0	1	0	1	0	1	1
0	0	0	0	1	0	0	0	1	0	0	1	0	1	1	1
0	0	0	1	0	0	0	0	1	0	0	1	0	1	1	1
0	0	0	1	0	1	0	0	1	0	0	1	0	1	1	1
0	0	1	0	0	0	0	0	1	0	0	1	0	1	1	1
0	0	1	0	1	0	0	0	1	0	0	1	0	1	1	1
0	1	0	0	0	0	0	0	1	0	0	1	0	1	1	1
0	1	0	1	0	0	0	0	1	0	0	1	0	1	1	1
0	1	1	0	0	0	0	0	1	0	0	1	0	1	1	1
0	1	1	1	0	0	0	0	1	0	0	1	0	1	1	1
1	0	0	0	0	0	0	0	1	0	0	1	0	1	1	1
1	0	0	1	0	0	0	0	1	0	0	1	0	1	1	1
1	0	1	0	0	0	0	0	1	0	0	1	0	1	1	1
1	0	1	1	0	0	0	0	1	0	0	1	0	1	1	1
1	1	0	0	0	0	0	0	1	0	0	1	0	1	1	1
1	1	0	1	0	0	0	0	1	0	0	1	0	1	1	1
1	1	1	0	0	0	0	0	1	0	0	1	0	1	1	1
1	1	1	1	0	0	0	0	1	0	0	1	0	1	1	1
1	1	1	1	1	0	0	0	1	0	0	1	0	1	1	1

← scan x direction
 ← scan y direction
 ← enter trace mode

Allowable Data Bytes





-  PRINTABLE CHARACTER
-  PRINTER CONTROL CHARACTER
-  AUXILIARY DEVICE CONTROL CHARACTER
-  CODES GENERATED BY KEYBOARD, BUT NO ACTION TAKEN

Figure B.3. ASCII character set.

The Digitizing and Data
Recording Circuitry

The Zeiss scanning stage steps from one data point to the next in a manner determined by the parameters input to the scanning stage control circuitry described above. At each desired data point the light that passes through the system and sample causes an analog signal when received at an SGD-100A photodiode. The scanning stage is stopped during the measurement. A selectable delay is introduced between the last pulse to the scanning stage and a "start conversion" pulse to the A/D converter. The system clock is inhibited until the A/D converter signals "conversion complete". A 12 bit binary value corresponding to the light through the system is latched into two shift registers.

The following sequence of events occurs in the data collection process:

1. The current scanning stage position is compared with the desired limit in the current scan line (raster).
2. If the limit has not been reached, a pulse train corresponding to the desired number of 0.5 μm steps between data points is sent to the appropriate Zeiss stepping motor driver input. Physically there are four inputs, corresponding to +x, -x, +y, and -y. The Zeiss scanning stage is limited to a stepping rate of 200 pulses per second.
3. After the stage has moved the appropriate number of steps, a selectable delay is initiated. The delay is used to allow

mechanical vibration due to stage motion and analog transients in the photodetector circuitry to be damped.

4. A start conversion pulse is sent to the A/D converter (Varadyne systems Model ADC-M12B2D3). The system clock is inhibited until the A/D conversion is complete.
5. The 12-bit binary result of the A/D conversion is divided into two six-bit bytes and latched into shift registers. The 12-bit binary result is sent to the TI-733 as two ASCII characters, which can be recorded on the "record" cassette drive. The ASCII characters for control codes, upper and lower case alphabet, numerals and punctuation are composed of 7 bits. The lower six bits of each transmitted character are determined by the binary value from the A/D conversion. The seventh bit is generated by inverting bit six. This confines the recorded data to that region in the ASCII chart occupied by numbers, punctuation, and upper case alphabet (see Figure B.3). Bit 6 and 7 are never both zero; thus there is no possibility of sending a control code (having special meaning) to the computer during data transfer. Likewise, bits 6 and 7 are never both logical "1", so there is never the possibility of sending the delete character (decimal 127). A data separator is sent between each two related ASCII characters to preclude data scrambling in the event a character is lost. The data separator is hardware selectable and is currently a tilde (~). The output has the form shown in Figure B.5a.

(a)

Bit 7	A/D 6	A/D 12	1
Bit 6	A/D 6	A/D MSB	1
Bit 5	A/D 5	A/D 11	1
Bit 4	A/D 4	A/D 10	1
Bit 3	A/D 3	A/D 9	1
Bit 2	A/D 2	A/D 8	1
Bit 1	A/D LSB	A/D 7	0

Data Separator "v"
 Analog to Digital
 Most Significant Digit
 Analog to Digital
 Least Significant Digit

(b)

A/D 6	A/D 12	x 6	x 12	y 6	y 12	1	1	0
A/D 6	A/D MSB	x 6	x MSB	y 6	y MSB	1	1	0
A/D 5	A/D 11	x 5	x 11	y 5	y 11	1	0	1
A/D 4	A/D 10	x 4	x 10	y 4	y 10	1	0	0
A/D 3	A/D 9	x 3	x 9	y 3	y 9	0	1	0
A/D 2	A/D 8	x 2	x 8	y 2	y 8	0	0	0
A/D LSB	A/D 7	x LSB	x 7	y LSB	y 7	0	1	1

Device Control 1
 "e"
 "x"
 Y Position MSD
 Y Position LSD
 X Position MSD
 X Position LSD
 Analog to Digital MSD
 Analog to Digital LSD

Figure B.5. Digital data output format

6. When the desired limit of the current scan line (raster) has been reached, the output format is modified. The last data point in a scan line contains additional characters, which correspond to the current x stage position, the current y stage position, two characters for operator verification and a control character to start the playback cassette. Figure B.5b shows the output format. When the last data point in the current line is reached, all 9 characters are sent to the TI-733 terminal. In this case a lower-case "x" is used as the data separator. The lower-case "e" allows the operator to verify that the "device control 1" character is about to be sent. Device control 1 is interpreted by the TI-733 as the "start playback cassette" command.
7. The playback cassette, or the operator using the keyboard, loads a new scan direction: number of steps between data points and binary limit for the next scan line into the scanning stage control circuitry. The first two data points of a new line contain the first seven ASCII characters shown in Figure B.5b. The first two characters are A/D values, the second two are current x position, the third pair are current y position and the data separator is lower-case "x". The operator is able to confirm that the correct number of steps is being taken in the desired direction by investigating the change in the x and y current position characters. When the "trace" bit shown in

Figure B.2 is set, the seven-character output format displaying A/D value as well as current x and y position is used for the output of all data points. The trace bit would normally be used for system checkout or trouble shooting only, since it more than doubles the time necessary to transmit each data point to the computer at some later time.

APPENDIX C

ANALOG TO DIGITAL CONVERTER LINEARITY

An important link in the process of obtaining data in digital form from the microdensitometer is the conversion of an analog signal into a digital format.

Light passing through the system and sample and incident on the photodetector causes a current to flow. A buffer amplifier and a scaling amplifier with adjustable gain isolate the photodiode from the input load of an analog to digital converter module, "ADC-M series" made by Varadyne Systems. The A/D converter generates a twelve bit binary signal which corresponds to the input voltage. It is important to verify that the binary result is an accurate representation of the analog input to insure that no biasing or weighting of the data is anomalously introduced at this point in the data collecting process.

The output from a FLUKE 343A DC voltage calibrator was fed to the input of the A/D converter module. The voltage calibrator was warmed up and then stepped in 1 volt steps from 0 to 14 volts. The data was recorded on the TI-733 printer by the digitizing and recording circuitry described in Appendix B. The results obtained are presented in Table C.1.

The agreement between the expected value and the experimentally obtained value is very good. In addition, the recorded results were

observed to be stable over several collecting cycles of the digitizer which would indicate that the analog to digital converter did not introduce random noise.

Table C.1.

Input (Volts)	Recorded Result	Binary	Decimal	Ideal $\Delta=300$ Volt	Difference $\frac{\text{Ideal-Decimal}}{\text{Ideal}}$ %
0	B @	000000/000000	2	0	
1	,D	000100/101100	300	300	0
2	XI	001001/011000	600	600	0
3	CN	001110/000011	899	900	0.11
4	(R	010010/101000	1192	1200	0.67
5	SW	010111/010011	1491	1500	0.60
6	F\ 3 space	011100/000110	1798	1800	0.11
7		100000/110011	2099	2100	0.05
8	V%	100101/010110	2390	2400	0.42
9	@*	101010/000000	2688	2700	0.44
10	!.	101110/100001	2977	3000	0.76
11	C3	110011/000011	3267	3300	1.00
12	C8	111000/000011	3587	3600	0.36
13	#<	111100/100011	3875	3900	0.64
14	??	111111/111111	4095	off scale	

REFERENCES

- Beran, M. J., and G. B. Parrent, Jr., Theory of Partial Coherence, Prentice Hall, Englewood Cliffs, NJ (1964).
- Hoeschen, D., and W. Mirandé, A Microdensitometer with a He-Ne Laser as Light Source, Optik, 48, 459 (1977).
- Kogelnik, H., and T. Li, Laser Beams and Resonators, Appl. Optics, 5, 1550 (1966).
- Lighthill, M., Introduction to Fourier Analysis and Generalized Functions, Cambridge University Press, Cambridge, England (1958).
- McCamy, C. S., Concepts, Terminology and Notation for Optical Modulation, Phot. Sci. Eng., 10, 34 (1966).
- Optics for Industry, Catalog 77, Rolyn Optics Company, 800 Rolyn Place, Arcadia, CA 91006 (1977).
- Parrent, George B., Jr., and B. J. Thompson, Physical Optics Notebook, Society of Photo-Optical Instrumentation Engineers, Palos Verdes, CA (1969).
- Swing, Richard E., The Optics of Microdensitometry, Opt. Eng., 12, 185 (1973).
- Swing, R. E., Microdensitometer Optical Performance: Scalar Theory and Experiment, Opt. Eng., 15, 559 (1976a).
- Swing, R. E., Supplement to: Microdensitometer Optical Performance: Scalar Theory and Experiment, Unpublished, 4 Horizon Drive, Frederick, MD 21701 (1976b).
- Wagner, Robert F., Fast Fourier Digital Quantum Mottle Analysis with Application to Rare Earth Intensifying Screen Systems, Medical Physics, 4, 157 (1977).
- Wagner, R. F., and J. M. Sandrik, An Introduction to Digital Noise Analysis, in The Physics of Medical Imaging: Recording System Measurements and Techniques, Arthur G. Haus, Ed., From: Summer School, American Institute of Physicists in Medicine, University of North Carolina, Chapel Hill, NC (1979).
- Weingärtner, I., Laser Microdensitometer, Optik, 32, 508 (1971).

